COUPLED QUANTUM – SCATTERING MODELING OF THERMOELECTRIC PERFORMANCE OF NANOSTRUCTURED MATERIALS USING THE NON-EQUILIBRIUM GREEN'S FUNCTION METHOD

By

Anuradha Bulusu

Dissertation

Submitted to the Faculty of the

Graduate School of Vanderbilt University

in partial fulfillment of the requirements

for the degree of

DOCTOR OF PHILOSOPHY

in

Interdisciplinary Materials Science

August, 2007

Nashville, Tennessee

Approved:

Professor D. G. Walker

Professor L. C. Feldman

Professor D. Li

Professor R. D. Schrimpf

Professor N. H. Tolk

Dedicated to my parents, Kameswari and Deekshatulu Bulusu

and my sisters Kanchana and Uma, for teaching me to never give up

ACKNOWLEDGEMENTS

This research would not have been possible without the support of my advisor Prof. Greg Walker, a great teacher and mentor. I am indebted to him for his excellent guidance and support and for the countless hours he dedicated to our brain-storming sessions. He fostered a fun, stress-free working relationship while continuing to encourage my academic progress making it a real pleasure to work for him.

I would like to thank my committee members for their genuine interest and support during the course of this research. Their valuable advice and comments truly helped shape this research. I am grateful to Prof. Supriyo Datta of Purdue University for providing us with a manuscript of his book on which much of this research is based. I would also like to thank the National Science Foundation and a Vanderbilt Discovery Grant for financial support of this research.

Special thanks are due to Sameer Mahajan and Dongyan Xu for their friendship and time spent discussing various research problems. I would also like to thank Saumitra Vajandar and Sriram Dixit for their friendship and support throughout my time in Nashville.

Finally, there is a very special person who deserves my deepest thanks. My husband Nandan has always supported me and encouraged me through all the time spent working on this research. His caring and fun-loving nature provided a welcome respite on many long days.

TABLE OF CONTENTS

LIST OF FIGURES

CHAPTER I

MOTIVATION

Thermoelectric effects in materials allow for direct energy conversion in devices where thermal energy is converted into electricity through the Seebeck effect. Similar energy conversion occurs when a current passed through two dissimilar materials cools the junction through the Peltier effect. Applications of thermoelectricity include chip level electronics cooling, power generators for remote telecommunication, temperature control systems in solid state lasers etc. The emergence of low-cost, high-efficiency thermoelectric power generators will also help reduce our dependence on non-renewable energy resources.

Widespread commercial applications of thermoelectrics have been limited by their low efficiency which is characterized by the dimensionless thermoelectric figure of merit $ZT = S^2\sigma T/\kappa$ where S is the Seebeck coefficient, σ is the electrical conductivity and κ is the thermal conductivity [1]. The Seebeck coefficient and electrical conductivity depend only on the electronic properties of the material while the thermal conductivity can be dominated by contributions from both the electronic component as well as lattice vibrations. The best commercially available thermoelectric materials have $ZT \approx 0.9$. Extensive research has been focused towards developing materials that have a high Seebeck coefficient as well as structures that will either have reduced thermal conductivity or enhanced electrical conductivity resulting in an increase in ZT.

The advent of quantum well nanofilm and nanowire superlattice structures that improve the value of ZT due to a number of advantages shifted the focus from bulk materials towards understanding carrier transport behavior in nanostructures. Quantum confinement in nanostructures increases the local carrier density of states per unit volume near the Fermi energy increasing the Seebeck coefficient [2] while the thermal conductivity can be decreased due to phonon confinement [3, 4] and phonon scattering at the material interfaces in the superlattices [4, 5, 6]. Normally, the electrical conductivity is assumed *not* to be

significantly affected due to the large semiconductor bandgap and the disparity between the electron and phonon mean free paths [7, 8]. The combined benefits of reduced thermal conductivity and improved Seebeck coefficient imply a theoretically higher *ZT* compared to the bulk structures. However, experimental observations especially in the case of Si/Ge superlattices have not been able to achieve the presumed benefits of superlattice thermoelectric devices despite theoretically predicted improvements in *ZT* and experimentally observed reduction in the thermal conductivity of superlattices compared to their bulk counterparts [2, 9]. Hence there is a need to better understand the effect of all the significant factors contributing to the thermoelectric figure of merit of nanoscale devices. In this regard, the two main phenomena that affect electron transport in nanostructures are 1) electron confinement and 2) electron scattering effects such as electron-phonon scattering, electron-impurity scattering etc.

The most common method of predicting thermoelectric parameters is based on a semi-classical, relaxation time approximation model where the system is assumed to be only slightly perturbed from equilibrium. While the semi-classical models work well in predicting the performance of materials in the bulk regime, wave effects that can not be captured naturally in particle-based models begin to dominate in nanostructured materials. Reduced dimensionality results in electron confinement and the formation of discrete subband energy levels in the confined direction. Tunneling of electrons and diffraction, characteristic of wave behavior, begin to dominate at low dimensions. Reduced dimensionality also results in phonon confinement and formation of phonon bandgaps that changes their dispersion relation. Although most of these models use confined dispersion relations, transport and thermoelectric coefficients are still calculated using the semi-classical relaxation time approximation model that cannot adequately capture wave effects. Quantum effects such as subband formation and tunneling are usually introduced in semi-classical models using correction terms [10, 11, 12]. On the other hand, purely quantum transport models [13, 14] that involve the solution to the Schrödinger equation are limited to studying current flow where transport is generally ballistic or includes very limited scattering.

A quantum transport model that can successfully couple wave effects and scattering effects to predict thermoelectric performance is introduced in this research through the non-equilibrium Green's function

(NEGF) method. In addition to successfully coupling quantum and scattering effects, the NEGF method allows us to seamlessly include various parameters that affect thermoelectric performance such as bandgap, doping, and effective mass. We propose to use the NEGF method as a design tool to model thermoelectric structures with optimized values of doping, effective mass and superlattice geometry taking into consideration the effects of electron confinement and scattering to give the best value of ZT. In addition to studying thermoelectric transport at nanoscales, the NEGF method will act as a framework for analysis of other emerging technologies in the field of solid-state energy conversion devices where temperature effects on carrier transport are strong. With the growing impact of nanotechnology in a broad range of fields such as microelectronics, medical imaging, nanocomposite materials etc, the need for quantum modeling has never been greater. The use of NEGF formalism to model electron transport represents a paradigm shift in carrier transport modeling in nanoscale devices. **This effort represents the first reported use of the nonequilibrium Green's function method to predict thermoelectric performance of nanoscale structures**.

Organization of the Thesis

The reminder of chapter 1 consists of a review of semiconductor solid state physics with an emphasis on the change in bandstructure with electron confinement. A description of Fermi's Golden Rule is provided to explain the physics involved in modeling electron-phonon scattering in semiconductors. Chapter 2 provides a review of the progress made in thermoelectric material research since Seebeck first discovered thermoelectricity in 1821. A review of the various analytical models used to identify and characterize thermoelectric performance of materials and structures is also provided starting with Sommerfeld's free electron model. Chapter 3 introduces the NEGF model with a description of the numerical scheme involved in calculating current-voltage characteristics for various materials and structures. Chapter 3 also contains a description of the calculation of Seebeck coefficient and electrical conductivity from current-voltage characteristics obtained using the NEGF model. The thermoelectric coefficients of ballistic silicon nanofilms and nanowires are calculated and compared to experimental measurements in chapter 4. The change in thermoelectric performance as a function of doping and film thickness is studied. The change in

thermoelectric performance when electron-phonon scattering is included in the NEGF model is analyzed for silicon films. Chapter 5 consists of a study of the thermoelectric performance of Si/Ge/Si quantum well superlattices. The change in thermoelectric performance with substrate strain is compared for superlattices with varying thicknesses and doping levels. The change in the over all thermoelectric performance of strained superlattices due to electron-phonon scattering is analyzed. Chapter 6 presents the conclusions drawn from the various studies done towards demonstrating the efficiency of the NEGF method as a viable tool for designing high-efficiency nanoscale structures for energy conversion.

Background

Electrons traveling in a semiconductor experience the periodic potential of the lattice U_C [15]. These electronic wave functions are known as Bloch waves and combine the periodicity of the lattice u_k with the plane wave.

$$\psi_k = u_k e^{ikx} \qquad (1)$$

The dependence of the electronic wave function on the crystal periodicity causes its momentum to vary with position as the crystal momentum alternately speeds up and slows down the electrons. As a result the crystal momentum $\hbar k$ is commonly used to represent the electron momentum where k is the crystal wave vector. The value of the periodic crystal potential is obtained by substituting the wave function in equation 1 in the one-electron Schrödinger wave equation and solving the wave equation by including the crystal potential.

$$\left[\frac{1}{2m}\left(\frac{\hbar}{i}\frac{\partial}{\partial x}+\hbar k\right)^2+U_C(x)\right]u_k = E(k)u_k \qquad (2)$$

Solving equation 2 for any crystal wave vector k will give a set of n eigen values $E_n(k)$ and the corresponding eigen functions u_{nk}. Hence for each n, $E(k)$ forms a band of energies that vary with k. The bandstructure is expanded using Taylor series as

$$E(k) = E(\mathrm{k}) + \left.\frac{\partial E}{\partial k}\right|_{k=\mathrm{k}} k + \left.\frac{\partial^2 E(k)}{\partial k^2}\right|_{k=\mathrm{k}} \frac{k^2}{2} + \ldots.. \qquad (3)$$

At the band extrema for k = **k**, the slope $dE(k)/dk$ goes to zero and hence the bandstructure (approximated to second order) can be rewritten as

$$E(k) = E(\mathrm{k}) + \frac{k^2}{2}\frac{\partial^2 E(k)}{\partial k^2}\bigg|_{k=\mathrm{k}} \qquad (4)$$

Equation 4, known as the dispersion relation, can also be written as

$$E(k) = E(\mathrm{k}) + \frac{\hbar^2 k^2}{2m^*} \text{ where } \frac{1}{m^*} = \frac{1}{\hbar^2}\frac{\partial^2 E(k)}{\partial k^2} \text{ is the equation for effective mass.} \qquad (5)$$

The band extrema lies at the energy minima for conduction bands and energy maxima for valence bands. When the band extrema occurs at k = 0, the dispersion relation may be written as

$$E(k) = E(0) \pm \frac{\hbar^2 k^2}{2m^*} \qquad (6)$$

The second term in equation 6 represents the kinetic energy of the electron or hole in the band. In a three-dimensional semiconductor the Brillouin zone is a volume with wave vectors extending in all three directions and $E(k)$ is a function of the direction of k. Equation 6 represents a three-dimensional isotropic energy band whose constant energy surface in k-space is a sphere if the effective masses are equal in all three directions of that surface.

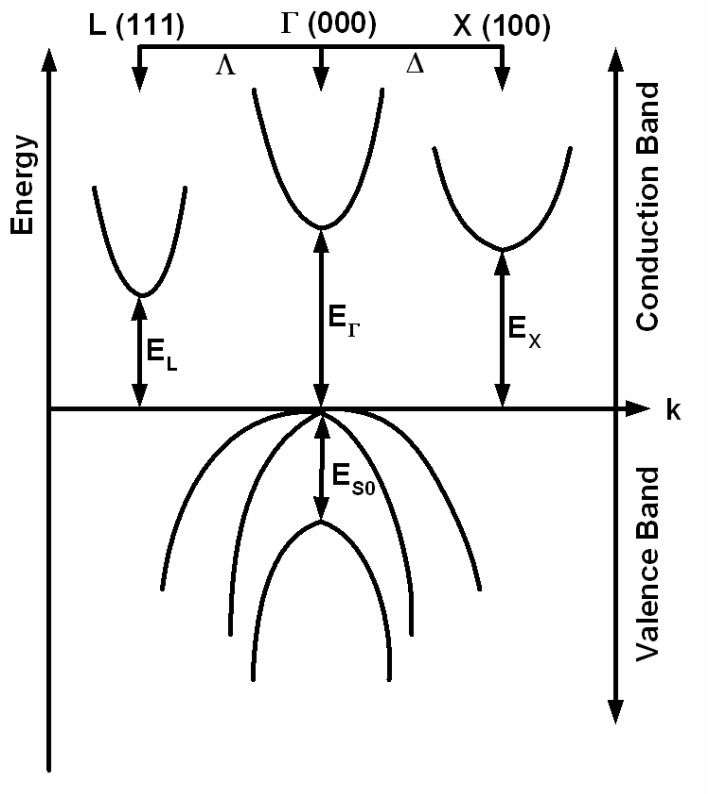

Figure 1. Bandstructure of silicon.

In an FCC diamond crystal such as silicon shown in figure 1, the conduction band has many minima. The lowest conduction band minimum in the case of silicon occurs near the X point along the Δ line that connects the Γ and X points, corresponding to the <100> directions. In common semiconductors such as silicon and germanium, the effective masses are orientation dependent and hence the energy band equation becomes

$$E(k) = E(\mathrm{k}) + \frac{\hbar^2}{2}\left[\frac{k_l^2}{m_l^*} + \frac{k_t^2}{m_t^*}\right] \qquad (7)$$

In anisotropic semiconductors the constant energy surfaces are ellipsoidal in shape as shown in figure 2. Hence there are six constant energy surface ellipsoids for silicon at the conduction band minima along <100>. In the case of germanium, the minimum occurs at the L point corresponding to the <111> directions. Hence there are eight constant energy surface ellipsoids for germanium.

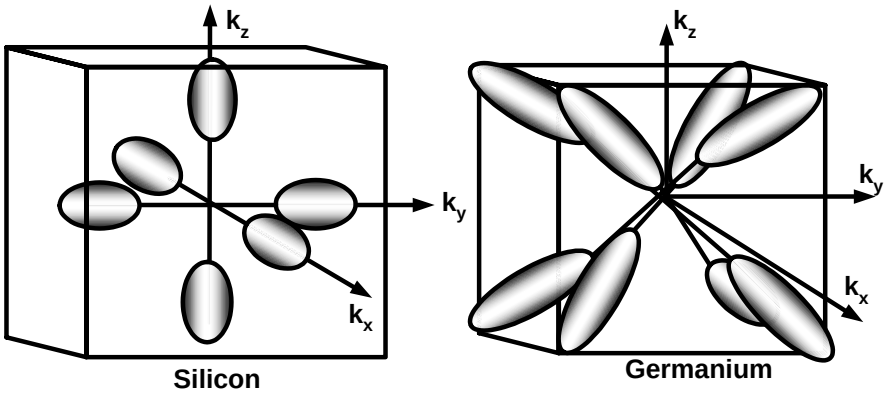

Figure 2. Constant energy surface ellipsoids for silicon and germanium.

The energy relations in the valence band are more complex as the light and heavy hole valence bands are degenerate at k = 0 leading to stronger interactions and complex bands. The parabolic approximation works well in general for low energy electrons near the conduction band minima. In the case of high fields electrons in the conduction band are accelerated and gain high energies. Under such circumstances the higher order terms in the Taylor series cannot be ignored and the bandstructure becomes more complex.

Bandstructure of Confined Electrons

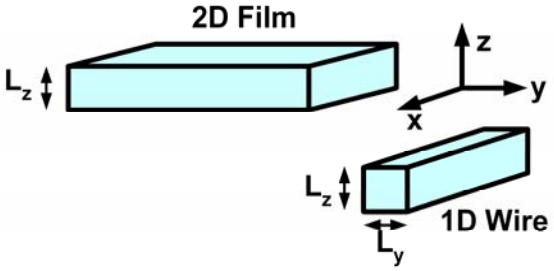

Figure 3. (a) 2D film with confinement along z axis (b) 1D wire with confinement along y and z axes.

Figure 3a and 3b show an example of a nanofilm with very small thickness along the z-axis and a nanowire with very small dimensions along y and z axis. In a bulk homogeneous system electrons are free to travel in the x, y and z directions and the dispersion relation can be described by parabolic bands near the conduction band edge as shown in figure 4a and described in equation 8.

$$E(k_x, k_y, k_z) = E_C + \frac{\hbar^2 k_x^2}{2m^*} + \frac{\hbar^2 k_y^2}{2m^*} + \frac{\hbar^2 k_z^2}{2m^*} \qquad (8)$$

When one dimension of the bulk solid is reduced to a very small scale such as a thin film or transistor with very small thickness along the z-direction, electrons in the thin film are free to travel along the x-y plane but are said to be *confined* along the z-axis. Since the parabolic energy bands describe the kinetic energy of the carriers for wide range of *k* values, confined electrons have flatter bands with discrete energy levels described by only a few wave vectors. Figure (4b) shows the overall energy dispersion relation of electrons in a confined film. The discrete energy levels along the z-axis are given by ε_1, ε_2 etc. while the parabolic *E(k) vs.* $k_{x\text{-}y}$ curves give the energy distribution along the x-y plane.

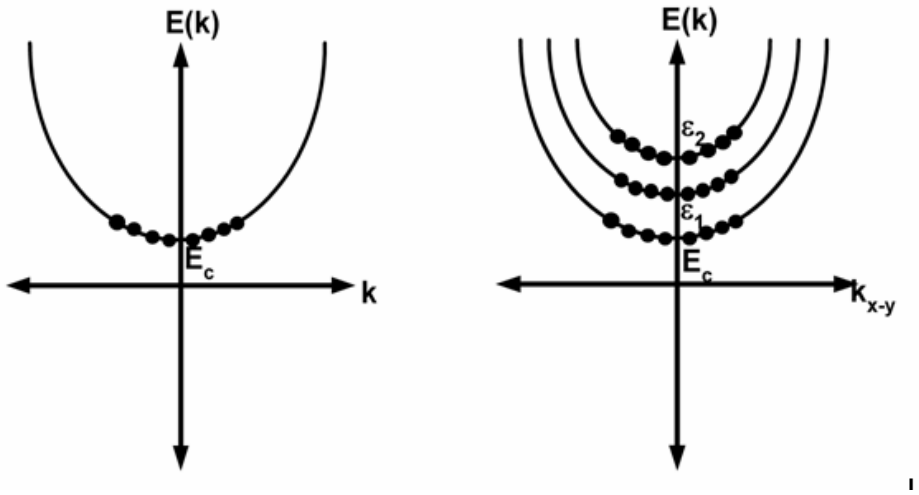

Figure 4. (a) Bandstructure of a bulk solid (b) bandstructure of a confined solid with discrete energies along the z axis.

The discrete z-axis energy levels are known as subbands and can be obtained by solving the wave equation along the z-axis with appropriate boundary potentials. For example, treating the electrons to be confined with periodic potentials in the z-direction such as in a carbon nanotube yields discrete k_Z values given by k_Z

$= 2n\pi/L_Z$ where n is the subband index [16]. In the case of thin films and transistors, the electrons are said to be confined by infinite potential boundaries resulting in $k_Z = n\pi/L_Z$. The energy dispersion relation for a 2D thin film is then given by

$$E(k_x, k_y, k_z) = E_C + \frac{\hbar^2 k_x^2}{2m^*} + \frac{\hbar^2 k_y^2}{2m^*} + \frac{\hbar^2}{2m^*}\left(\frac{n\pi}{L_z}\right)^2 \qquad (9)$$

Similarly, the dispersion relation for a one-dimensional wire is given by

$$E(k_x, k_y, k_z) = E_C + \frac{\hbar^2 k_x^2}{2m^*} + \frac{\hbar^2}{2m^*}\left(\frac{m\pi}{L_y}\right)^2 + \frac{\hbar^2}{2m^*}\left(\frac{n\pi}{L_z}\right)^2 \qquad (10)$$

When a thin film or wire is connected to contacts in order to apply a bias, the incoming electrons have to take into account the confined energy levels in the film or wire. Hence, for a two dimensional film the Fermi function is given by considering the electrons to have parabolic energy levels in the infinite x and y directions and experience confinement along the z direction [16].

$$f_{2D}(E) = N_0 \log\left(1 + \exp\left(-\frac{E-\mu}{k_B T}\right)\right) \text{ where } N_0 = \frac{m^* k_B T}{2\pi\hbar^2} \qquad (11)$$

The Fermi function for a 1D film is calculated in a similar manner by considering the electron to have infinite potential boundary conditions in the y-z axes and free flow only in the x direction. f_{1D} is given by

$$f_{1D} = \frac{N}{4\pi} f_{-1/2}(E/k_B T) \quad \text{where } N = \sqrt{\frac{2m_c k_B T}{\hbar^2}} \qquad (12)$$

$$f_{-1/2}\left(E/k_B T\right) = \frac{1}{\sqrt{\pi}} \int_0^\infty \frac{dy}{1 + \exp\left(\varsigma - E/k_B T\right)} \frac{1}{\sqrt{E/k_B T}} \text{ and } \varsigma = \frac{\hbar^2 k_x^2}{2m^* k_B T}. \qquad (13)$$

Electron-Phonon Scattering

The motion of electrons traveling in a device is frequently interrupted by collisions with phonons, impurity atoms, defects in the crystal etc. The scattering of electrons with each type of scatterer is usually characterized by a scattering rate which gives the probability per unit time that an electron with crystal momentum *k* scatters to a state with crystal momentum *k'*. Consider the inflow and outflow of electrons

into a specific energy level ε due to energy transitions from levels above ε_2 and below this level ε_1. The energy levels are separated by an energy value of $\hbar\omega$ such that $\varepsilon_2 - \varepsilon = \varepsilon - \varepsilon_1 = \hbar\omega$. In the early 20th century Einstein proposed that if there are N photons present in a box each with energy $\hbar\omega$, then the rate of downward transitions is proportional to N+1 while the rate of upward transitions is proportional to N [17]. Einstein argued that this difference in the transition rates ensured that at equilibrium, the lower energy states are more likely to be occupied than the higher energy states as predicted by the Fermi function. Since photons and phonons are described by the Bose-Einstein distribution we can extend this argument to the case of electron transitions due to phonon absorption and emission. The electrons and phonons are treated as one big many-particle system whose dynamics are described by an equation similar to the Schrödinger equation as

$$[H]\{\psi\} = i\hbar \frac{d}{dt}\{\psi\} \qquad (14)$$

The vector $\{\psi\}$ represents a state vector in a multi-particle Hilbert space that includes both electrons and phonon systems [16]. In the many-particle system similar to a device connected to a source and drain contacts, the N phonon subspace is coupled to the N+1 phonon subspace through phonon emission and to the N-1 phonon subspace through phonon absorption. The emission and absorptions are peaked for phonon energies of $\hbar\omega$ where $\varepsilon_n - \varepsilon_m = \hbar\omega$. The transition of the electrons from ε_n to ε_m and vice versa is dependent on the transition rate *S(k, k')* which is obtained using Fermi's Golden Rule [15]. This coupling can be expressed through a broadening term Γ which is related to the transition rate S as

$$\frac{\Gamma}{\hbar} = S(k,k') \quad \text{where}$$

$$\Gamma_{nn} = 2\pi \left|K_{mn}^{em}\right|^2 (N+1)\delta(\varepsilon_n - \varepsilon_m - \hbar\omega) + 2\pi \left|K_{mn}^{ab}\right|^2 (N)\delta(\varepsilon_n - \varepsilon_m + \hbar\omega) \qquad (15)$$

The coupling constants *K* are expressed in the form of an interaction potential invoking the one-electron viewpoint where a single electron feels the potential due to one phonon occupying a particular mode.

$$K_{mn}^{em} = \int dr \phi_m^*(r) U^{em} \phi_n(r) \text{ and } K_{mn}^{ab} = \int dr \phi_m^*(r) U^{ab} \phi_n(r) \qquad (16)$$

Representing the phonon waves as plane waves with wave vector β, the interaction potential is written as

$$U_S(\vec{r},t) = K_\beta^{ab} A_\beta^{ab}(\vec{r}) \exp\left(i\vec{\beta}.\vec{r}\right) + K_\beta^{em} A_\beta^{em}(\vec{r}) \exp\left(-i\vec{\beta}.\vec{r}\right) \quad (17)$$

Substituting equation 17 into 16 and then into 15 yields the broadening matrix as

$$\Gamma_{nm} = \left|K^{em}{}_\beta\right|^2 \left|A^{em}{}_\beta\right|^2 (N+1)\delta(\varepsilon_n - \varepsilon_m - \hbar\omega) + 2\pi \left|K^{ab}{}_\beta\right|^2 \left|A^{ab}{}_\beta\right|^2 (N)\delta(\varepsilon_n - \varepsilon_m + \hbar\omega) \quad (18)$$

K_β is a function of the change in electronic potential energy per unit strain of the lattice. For acoustic phonons that displace neighboring atoms in the same direction, lattice spacing is produced by the strain and not the displacement. Optical phonons displace neighboring atoms in opposite directions and this displacement produces a change in lattice spacing directly. Hence the scattering interaction potential for acoustic phonons and optical phonons is written as

$$\left|K_\beta\right|^2 = \beta^2 D_A^2 \quad \text{and} \quad \left|K_\beta\right|^2 = D_o^2 \quad (19)$$

where D_A is the acoustic deformation potential and is experimentally known for most bulk materials of interest while D_o is the optical phonons deformation potential.

$|A_\beta|^2$ is the square of the amplitude of lattice vibration. While classically the energy of vibration is proportional to the square of its amplitude of oscillation, quantum mechanically this energy is quantized and is given as

$$E = \left(N + \tfrac{1}{2}\right)\hbar\omega \quad \text{where N = 0, 1, 2, …..} \quad (20)$$

By equating the maximum kinetic energy of the oscillating wave to the quantum mechanical energy, the value of $|A_\beta|^2$ is obtained as

$$\left|A_\beta\right|^2 \approx \frac{\hbar}{2\rho\Omega\omega_\beta} \quad (21)$$

ρ is the mass density, ω_β the phonon frequency and Ω is the normalization volume. Depending on the type of phonon that the electron interacts, the value of K_β and A_β can be used to calculate the broadening matrix Γ_{nm}.

CHAPTER II

REVIEW OF THERMOELECTRIC MATERIALS AND MODELS

In general thermoelectric research is two-pronged with 1) experiments focused towards finding new materials and structures with enhanced thermoelectric performance and 2) analytical models that predict thermoelectric behavior to enable better design and optimization of materials and structures. In this paper we present a review of the theoretical models that were developed since thermoelectricity was first observed in 1821 by Seebeck and how these models have guided experimental materials search for improved thermoelectric devices. A new quantum model is also presented, which provides opportunities for optimization of nanostructured materials to enhance thermoelectric performance.

Thermoelectric Properties

When two wires of different metals are joined at both ends and the two junctions are kept at different temperatures, a voltage develops across the two junctions. This effect is known as the Seebeck effect which was discovered by Seebeck in 1821 and published in 1822 [18]. The voltage across the two junctions is proportional to the temperature gradient across the junctions provided the temperature gradient is small. The proportionality constant is defined as the Seebeck coefficient or thermoelectric power and is obtained from the ratio of the voltage generated and the applied temperature gradient.

$$S = \frac{dV}{dT} \qquad (22)$$

In 1834, the Peltier effect was discovered [19]. When two metals are joined together and kept at constant temperature while a current passes across the junction, heat is generated or absorbed at that junction in addition to Joule heating. The Peltier coefficient Π_{12} is defined as the heat emitted per second when unit current flows from conductor 1 to 2. This heat is directly proportional to the current passing through the junction as described by equation 23.

$$dQ = \prod dI \qquad (23)$$

The Thomson effect was predicted in 1854 and found experimentally in 1856 [20]. The Thomson effect occurs when a current flows across two points of a homogeneous wire having a temperature gradient along its length and heat is emitted or absorbed in addition to the Joule heat. The Thomson coefficient μ_T is positive if heat is generated when positive current flows from a higher temperature to lower temperature.

$$dQ = \mu_T \frac{\partial T}{\partial x} dx dI \qquad (24)$$

These three thermal-electrical properties provide the basis for modern direct energy conversion devices and their exploitation is the subject of considerable research.

Development of Semiconductor Thermoelectric Materials

Initial thermoelectric materials studied were metals which displayed Seebeck coefficients of a few tens of μV/K. However, in the middle of the 20th century, interest turned towards semiconductors as thermoelectric materials due to their high Seebeck coefficients and dominance of lattice heat conduction despite small ratios of electrical to thermal conductivity. In 1952 Ioffe et al. [21] studied the change in semiconductor thermal conductivity of a material relative to its position in the periodic table. He found that for larger mean atomic weight, the thermal conductivity was lower. This behavior was attributed to the increase in density that caused the velocity of sound in the crystal to decrease leading to a subsequent decrease in thermal conductivity. Since mobility of electrons serves as a direct relation between the crystal structure and electrical conductivity, Goldsmid [22] studied the ratio of mobility μ and thermal conductivity κ as a function of the mean atomic weight. Using the relationship proposed by Shockley and Bardeen [23] for mobility in semiconductors and Pierls relationship for thermal conductivity, he calculated the ratio as a function of the electron mean free path ι_e and phonon mean free ι_p paths in crystals.

$$\frac{\mu}{\kappa} = \frac{4e\rho}{c\upsilon_s (2\pi m_e k_B T)^{1/2}} \frac{l_e}{l_p} \qquad (25)$$

Here ρ is the density; υ_s the velocity of sound and c is the specific heat of the crystal while m_e and e are the electron mass and charge respectively. Using material properties measured for some common

semiconductors they plotted the above ratio against the mean atomic weight of the semiconductors seen in figure 5. Applying the above mentioned selection rules of choosing materials with high Seebeck coefficients and high atomic weights led to the discovery of Bi_2Te_3 in 1954 by Goldsmid and Douglas [24] that provided cooling of 26^0C. Bismuth telluride has a hexagonal structure with mixed ionic-covalent bonding along the lattice planes and the weak van der Waals bonding perpendicular to the planes. The hexagonal structure ensures high anisotropy in the lattice conductivity with a factor of 2 decrease in the thermal conductivity in the direction perpendicular to the planes. Bismuth telluride also has a multivalley bandstructure with multiple anisotropic constant energy surfaces that have a small effective mass in one direction and large effective masses in the other two directions. Since smaller effective mass lead to high electron mobility, choosing the appropriate growth direction of bismuth telluride will ensure good thermoelectric performance.

In 1956, Ioffe et al. [25] suggested that alloying a semiconducting thermoelectric material with an isomorphous substance i.e. having the same crystalline structure, would enhance the figure of merit by reducing lattice thermal conductivity without affecting carrier mobility. They suggested that phonons would scatter due to the disturbances in the short-range order but the preservation of long-range order would prevent scattering of electrons and holes. This led to an extensive study of the thermoelectric performance of various semiconductor alloy systems over a wide range of temperatures.

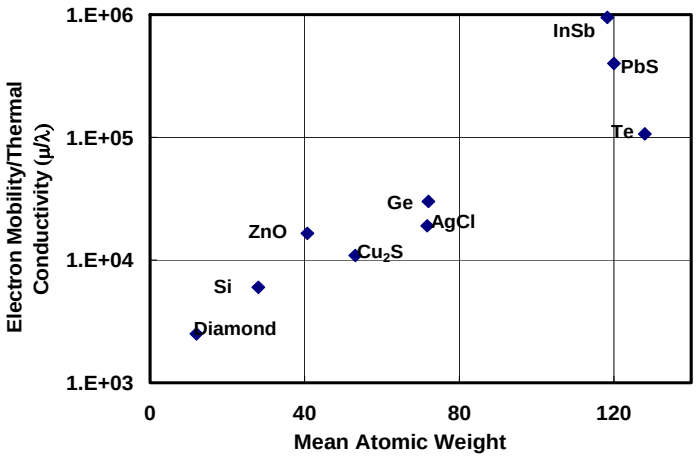

Figure 5. Ratio of electron mobility to thermal conductivity of thermoelectric materials. Reproduced from data in [22].

Birkholz in 1958 [26] and Rosi et al. in 1959 [27] showed that alloying Bi_2Te_3 with Sb_2Te_3 or Bi_2Se_3 greatly reduced the thermal conductivity. They also showed that adding even 5% of Sb_2Se_3 greatly improved the figure of merit by raising the bandgap that reduced ambipolar conduction i.e. contribution due to both electrons and holes to electrical conductivity and thermal conductivity. These studies led to the formation of a pseudo-ternary Bi_2Te_3 - Sb_2Te_3 - Sb_2Se_3 system. The studies showed that the best n-type material was the Bi_2Te_3 rich alloys while the best p-type performance was obtained from the Sb_2Te_3 pseudo-ternary alloys with an average figure of merit of $3.3x10^{-3}K^{-1}$ from both types at room temperature [28]. In general however, bismuth and bismuth telluride alloys are good thermoelectric materials only below room temperature. At room temperature and above, the relatively small bandgap causes mixed conduction due to both electrons and holes leading to reduced Seebeck coefficient.

At temperatures above those that bismuth telluride can be used, materials like lead telluride are found to have very good thermoelectric properties in the range of 300K to 700K. Lead telluride belongs to the lead chalcogenides system similar to materials such as PbS and PbSe. Lead chalcogenides have a cubic (NaCl) rock-salt structure with a FCC unit cell. They are polar semiconductors with a mixed ionic-covalent bond with the electrons traveling mainly in the cation (Pb) sublattice and the holes in the anion chalcogenide sublattice. Similar to bismuth telluride PbTe has high mean atomic weight and a multivalley bandstructure. Having slightly higher bandgap of 0.32eV at 300K it produces higher Seebeck coefficients. While it has

higher lattice thermal conductivity than bismuth telluride at room temperature, it eventually produces higher *ZT* values as the temperature is raised. Lead telluride also forms isomorphous solid solutions with lead selenide and tin telluride leading to lower thermal conductivities and improved *ZT* values. Rosi et al. [28] in 1961 studied the bandgap of the PbTe-SnTe system and determined that band reversal effect actually causes the bandgap to go to zero at the composition $Pb_{0.4}Sn_{0.6}Te$ and hence recommended that lower compositions of tin telluride would ensure sufficient bandgaps leading to ZT values near 1 for n-type PbTe-SnTe alloys at 700K [29]. Another type of alloy system that gives ZT values around 1 for temperature range around 700K are alloys between $AgSbTe_2$ and GeTe called TAGS [30]. These alloys posses the same rock-salt structure of PbTe over part of the compositional range. When the composition of GeTe is greater than 70% it leads to a transition to rhombohedral structure. The lattice strain associated with this phase transition is also believed to contribute to reduced lattice thermal conductivity values around 1.5W/m-K. At higher temperature ranges of 600K to 1300K, silicon and germanium which are bad thermoelectrics due to their high thermal conductivity at room temperature can be alloyed to obtain SiGe alloy, a far superior material for thermoelectric generation [31]. The large bandgap of silicon makes silicon rich alloys such as $Si_{0.7}Ge_{0.3}$ suitable for high temperature applications since problems with minority carrier dominance do not arise. The large phonon scattering ensures low thermal conductivity without affecting the electron mobility making it possible to obtain *ZT* values of 0.5 and higher [32].

Materials in general exhibit the best possible thermal conductivity in the crystalline state and the lowest conductivity in the amorphous state. Based on this concept Slack in 1979 [33] proposed that the smallest possible lattice conductivity can be predicted by setting the mean free path of the phonons equal to that in the amorphous state. This observation prompted extensive research leading into materials that are termed as phonon glass and electron crystal (PGEC). These materials have very complex structures such as compounds of Borides (YB_{68}) [34] and compounds of silver-thallium ($TlAsSe_3$) [35]. These materials contain groups of atoms or molecules that do not have precisely defined positions or orientations. The lack of long-range order causes the atoms or molecules to *rattle* and act as phonon scattering sites reducing the thermal conductivity to around 0.5W/m-K

Another class of materials is called Skutterudites, which are complex materials with a chemical formula of $ReTm_4M_{12}$ where Re is a rare earth element such as lanthanum or cerium, Tm is a transition metal such as cobalt, iron etc and M is metalloid such as phosphor, arsenic, or antimony. Binary skutterudites have the chemical formula of TmM_3, and its crystal structure has the unique feature of containing two large empty spaces within each unit cell. While the binary structures have reasonably large Seebeck coefficients of around 200μV/K, they still exhibit very high thermal conductivities [29]. When a rare earth element is mixed with the binary skutterudite, the heavy atom of the rare earth element occupies the empty space of the crystal [36]. In addition to causing large impurity scattering of phonons in these materials, the loosely bound heavy atoms rattle in their *cages* enhancing scattering of phonons and reducing thermal conductivity by an order of magnitude at room temperature. Skutterudites have been found to have a figure of merit greater than one at temperatures around 700K.

Additional examples of PGEC materials are inorganic clathrates with the chemical formula A_8B_{46} where B represents for example either gallium or germanium or a combination of the two elements [29]. These materials are found to be very promising for power generation at temperatures above 600ºC. Clathrates consist of an open framework of gallium and germanium atoms that act as an electron crystal. Guest atoms are selectively incorporated in nanocavities in the crystal. The guest atoms vibrate independent of the crystal structure scattering phonons in the process. Clathrates can be made of tin, silicon, antimony etc. Examples of some good thermoelectric clathrates are $Sr_8Ga_{16}Ge_{30}$, Cs_8Sn_{44} as well as well as Zn_4Sb_3 that has been observed to give ZT values of 1.3 at 400K. More recently an alloy of Pb-Sb-Ag-Te abbreviated as LAST was developed as n-type thermoelectric material having ZT values around 1.7 [37, 38]. These alloys have nano-sized inclusions during synthesis that act as phonon scattering sites. A similar p-type alloy dubbed as SALT was observed to have ZT values around 1.6, the highest known for p-type thermoelectric materials.

In addition to the development of bulk materials with enhanced thermoelectric properties, the development of superlattices to improve ZT has led to research in superlattices made from alloys that are good thermoelectric materials to start with such as Bi_2Te_3/Sb_2Te_3, Bi_2Te_3/Bi_2Se_3 as well as PbSeTe/PbTe

quantum dot superlattices, $Si/Si_{1-x}Ge_x$ and Si/Ge superlattices [8]. While fabrication of superlattice films and wires can take advantage of the advances made in semiconductor manufacturing technology such as molecular beam epitaxy, metallorganic chemical vapor deposition etc, significant challenges exist in translating the high ZT performance of bulk materials into similar performance in nanoscale applications. In this regard the biggest bottleneck is the electrical conductivity which is dominated by contact resistance. The anisotropic nature of most nanoscale materials also makes their thermal conductivity performance unpredictable and hard to measure. Measurement of thermoelectric properties at the nanoscale is especially hard as the substrate and buffer layers can overwhelm the Seebeck coefficient and electrical conductivity measurements. The challenges and high costs associated with nanoscale measurements places special emphasis on the need to have a detailed understanding of electron-hole-phonon transport at the nanoscale so as to better predict thermoelectric performance. Quantum confinement effects while increasing the density of states per unit volume at the Fermi level can also lead to reduced electrical conductivity due to the limited energy states available for electron transport. Similarly while phonon scattering and confinement at the superlattice interfaces can lead to reduced thermal conductivity, its impact on electron and hole transport through confined carrier-phonon scattering also has to be better understood. There has never been a greater need for a strong model that can couple both quantum and scattering effects to predict transport behavior in nanoscale devices.

Development of Modeling of Thermoelectric Coefficients

In 1928, A. Sommerfeld [39] put forth a comprehensive model on free electron theory in metals using Fermi-Dirac statistics instead of Maxwellian statistics for the free electron theory in metals developed by Lorentz. Sommerfeld assumed that only the valence electrons in a metal formed a free electron gas that obeyed the Fermi-Dirac distribution. In 1931, Sommerfeld and Frank [40] studied thermoelectric phenomena in metals studied where various combinations of the electric current and temperature gradient $\partial T/\partial x$ were applied on a wire. From their calculations they obtained equations for the electrical conductivity σ, thermal conductivity κ and Thomson coefficient μ_T. In all the calculations Sommerfeld and

Frank assumed conditions of local equilibrium and the number of electrons to be independent of temperature and the mean free path of the electrons to be independent of their velocity.

$$\sigma = \frac{4\pi e^2}{3m}\left(\frac{m}{h}\right)^3 \int_0^\infty f_0 \frac{\partial}{\partial v}\left(\ell v^2\right) dv \quad (26)$$

$$\kappa = \frac{4\pi m}{6}\left(\frac{m}{h}\right)^3 \left[\int_0^\infty \ell v^5 \frac{\partial f_0}{\partial x} - \frac{\int_0^\infty f_0 \frac{\partial}{\partial v}\left(\ell v^4\right) dv}{\int_0^\infty f_0 \frac{\partial}{\partial v}\left(\ell v^2\right) dv} \int_0^\infty \ell v^3 \frac{\partial f_0}{\partial x} dv \right] \quad (27)$$

$$\mu = \frac{2\pi^2 m k_B{}^2 T \lambda^2}{3eh^2} \quad (28)$$

where λ is the de Broglie wavelength of electrons.

Bloch [41] solved the wave equation for periodic metallic lattice and showed that if the lattice is perfect, the electron would travel infinitely through it and only by taking into consideration the thermal motion of the lattice and the effect of impurities would finite conductivity be obtained. In addition, Bloch showed that the application of Pauli's exclusion principle eliminated the direct proportionality between the number of free electrons and the electrical conductivity. Conduction under an applied field would then take place only if the final energy levels are unoccupied such that the electrons near the Fermi level can make transitions and take part in conduction. Bloch called these electrons conduction electrons. Based on these ideas Bloch introduced temperature dependence of electronic conduction in metals where the electric resistance varied directly with the absolute temperature for high temperatures and varies as T^5 for low temperatures. Bloch's theory of electrical conduction could not be easily extended to semiconductors as it seemed to suggest that a lattice should have nearly infinite conductance at low temperatures while in reality the conductivity of semiconductors is very low at low temperatures due to limited number of free electrons. It also could not explain the non-conductivity of insulators. In 1931, A. H. Wilson [42] extended Bloch's theory to semiconductors and developed a formal theory of electron transport in semiconductors and insulators with emphasis on the temperature dependence of electrical conductivity. Wilson's work was further extended to study Hall coefficients and thermoelectric power of semiconductors by M. Bronstein [43] in 1932 and R. H.

Fowler [44] in 1933 but neither of the results by these authors were in a form suitable for comparison with direct experimental data or predictions of thermoelectric power from measured Hall and resistivity data.

In his book *The Theory of Metals* in 1953 Wilson [45] gave a comprehensive analysis of the conduction mechanism and thermoelectric performance of metals and semiconductors under the relaxation time approximation taking into account the effect of electron scattering with acoustic and optical phonons and electron-impurity scattering. Based on his calculations, the relaxation time in metals for electron-phonon scattering was calculated to be proportional to $E^{3/2}T^{-1}$ which is the same result shown by Bloch for metals. In the case of semiconductors the distribution of electrons is taken to be $f_0=\exp^{-\left(\varepsilon-\varepsilon_f/k_BT\right)}$ and restricting the phonon energy range to values around the Fermi energy ε_f, Wilson calculated the electrical conductivity to be proportional to $nm^{*-5/2}T^{-3/2}$. By arriving at a direct proportionality between the conductivity and number of free electrons n, Wilson was able to show that semiconductors have very low conductivity at low temperatures due to the very small number of free electrons available for conduction.

In 1953 Johnson and Horovitz [46] used Sommerfeld's model of electric current and thermal current to calculate thermoelectric coefficients for three different cases. 1) Impurity temperature range where all the carriers are either *n*-type or *p*-type such that the concentration of carriers remains constant with temperature until intrinsic carrier effects become important. 2) Transition temperature range where in addition to *n* and *p* type carriers, intrinsic carriers also exist and hence $n_e \neq n_h$. 3) Intrinsic temperature range where intrinsic carrier dominate the electrons and holes from donors and acceptors such that $n_e = n_h$. The authors used Maxwell statistics to describe the carrier distribution in the semiconductors. The mean free path was said to be affected by lattice vibrations where similar to Sommerfeld, it was expressed to be independent of carrier energy. In the impurity and transition range an additional mean free path due to impurities was included where the mean free path was expressed as a function of carrier energy as $l_{imp} = a\varepsilon^2$. The thermoelectric power for polycrystalline germanium having carrier concentrations ranging from 10^{15}cm^3 to $7x10^{18}$cm^3 was calculated using these equations and compared to experiments conducted by Lark-Horovitz, Middleton, Miller Scanlon and Walerstein [47] over a temperature range of 78K to 925K. For impurity temperature range of approximately 78K to 300K there was lot of scatter in the experimental data and the theoretical

predictions were not in good agreement with the experiments. In the transition and intrinsic range of temperatures greater than 300K there was good agreement between experiments and theory.

When Lord Kelvin (Thomson) [48] formulated his theory of thermoelectric phenomena in 1854 he suggested that similar to the reciprocal relations between force and displacement in a mechanical system in equilibrium, there exist reciprocal relations between two or more irreversible transport processes that interfere with each other when they take place simultaneously in a thermodynamic system. Accordingly if J is the electric current due to an applied field and Q the thermal current due to the application of a temperature gradient, then for independent processes the electro-motive force that drives the electric current is given by

$$X_1 = R_1 J \qquad (29)$$

where R_1 is the resistance to current flow and the force that drives the thermal current is given by

$$X_2 = R_2 Q \qquad (30)$$

where R_2 is the resistance to the flow of thermal current. However since these two processes mutually interfere with each other two forces X_1 and X_2 must be expressed as a combination of the two resistances R_1 and R_2 as

$$X_1 = R_{11} J + R_{12} Q \qquad (31)$$

$$X_2 = R_{21} J + R_{22} Q \qquad (32)$$

Thomson suggested that *as long as there is no heat conduction from one part of the circuit to another,* $R_{12} = R_{21}$. Thomson's reciprocal relations were examined by Onsager in 1931 [49] who calculated the thermoelectric properties as the entropy flow per particle due to 1) heat flow from high temperature to low temperature and 2) degradation of electrochemical potential energy into heat. From the macroscopic laws governing the thermoelectric process, the electric current J and the thermal current Q were expressed as

$$-J = L_{11} \frac{1}{T} \nabla \mu + L_{12} \nabla \frac{1}{T} \qquad (33)$$

$$Q = L_{21} \frac{1}{T} \nabla \mu + L_{22} \nabla \frac{1}{T} \qquad (34)$$

L_{11}, L_{12} and L_{22} are called kinetic coefficients and are properties of the medium such as electrical conductivity, thermal conductivity etc and in the absence of a magnetic field, Onsager stated that

$$L_{12} = L_{21} \qquad (35)$$

Callen in 1948 [50] showed that while Onsager's relations strictly referred to specific transient irreversible processes, they could be extended to steady state processes by considering the system to be the limiting case of many small sections, each in local equilibrium. This assumption is incorporated by treating the temperature T and Fermi energy ε_f as functions of position. Callen pointed out that this assumption was similar to the assumptions made while using the Boltzmann transport equation where the system is assumed to be in local equilibrium by incorporating the deviation from equilibrium term in the calculations.

In 1953 Frederikse [51] noticed large anomalies in the predicted vs. measured thermoelectric power in germanium below temperatures of 200K. They attributed these anomalies to the assumption of lattice thermal equilibrium commonly made when calculating thermoelectric coefficients. The deviation from equilibrium of the lattice at low temperatures results in a phonon current that interacts with the electron current. Frederikse modified Horovitz's model to include an additional term inversely proportional to temperature that would account for the deviation from equilibrium of the lattice at lower temperatures. Onsager's reciprocal relations were used by P. J. Price [52] in 1956 where he used a modification of the Johnson-Horovitz model [53] to calculate the thermoelectric coefficients in isotropic semiconductors. The thermoelectric parameters were calculated phenomenologically as a function of the electron and hole conductivities using average values of the electric and thermal current.

$$\sigma = \langle J.J \rangle \qquad (36a)$$

$$S = \frac{1}{\sigma T} \langle J.Q \rangle \qquad (36b)$$

$$\kappa_e = \frac{1}{T} \langle Q.Q \rangle \qquad (36c)$$

The carrier energy was said to be affected by contributions from 1) electrostatic field 2) band edge energies 3) bandgap and at low temperatures 4) entrainment of the lattice energy due to carrier-lattice collisions

known as phonon-drag effect. The resulting expression for thermoelectric power was expressed in terms of the electron and hole electrical conductivities as

$$S = \frac{k_B}{2e\sigma}\left[\alpha\left(\sigma_e - \sigma_h\right) - \sigma \ln\left(\frac{\sigma_e}{\sigma_h}\right) - \sigma\xi\right] \text{ where } \sigma = \sigma_e + \sigma_h \text{ and } \xi = \log\left(\frac{\mu_e}{\mu_h}\left(\frac{m_e}{m_h}\right)^{3/2}\right)$$

(37)

Price assumed that the electron and hole mobilities were independent of doping and used the *S vs.* σ plot to graphically obtain the value of α, a function of the material bandgap, as shown in equation 38. Price showed that the graph, seen in figure 6, formed a loop where n-type materials are at the bottom of the loop and p-type materials at the top. The value where $\sigma_e = \sigma_h$ corresponded to the minimum value of σ where minimum thermoelectric power is obtained due to bipolar transport. In addition to the thermoelectric loop, another notable contribution made by Price was the study of the change in thermoelectric power of semiconductors under shear strain. He showed that shear strain would change the activation energy of the impurity donor atom binding a carrier in a many-valley band by decoupling the orbitals associated with the different valleys leading to a shift in the band edge energies. Price recognized that this shift in the band edge energies of the donor atoms would appreciably change the thermoelectric power of semiconductors especially at very low temperatures.

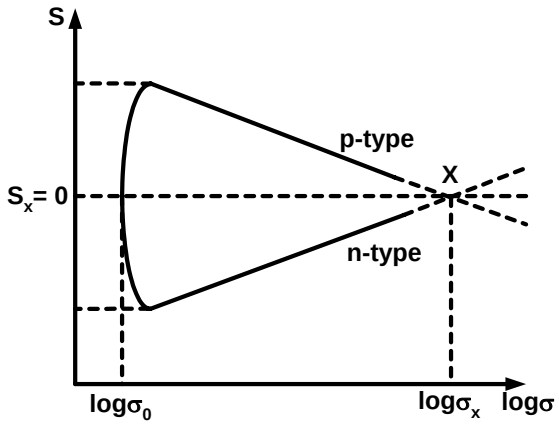

Figure 6. Price's doping curve for thermoelectric power. Reproduced from [52]

$$\alpha = 2\log\left(\frac{2\sigma_X}{\sigma_0}\right)\ldots\alpha \gg 1. \quad (38)$$

In 1912, Altenkirch [54, 55] introduced the concept of a figure of merit when he showed that good thermoelectric materials should possess large Seebeck coefficients, high electrical conductivity to minimize Joule heating and low thermal conductivity to retain heat at the junctions that will help maintain a large temperature gradient. Ioffe in 1957 [56] presented the figure-of-merit in its present form $Z= S^2\sigma/\kappa$ which he used to qualify the efficiency of thermoelectric materials. Ioffe gave a simple explanation to calculate the Seebeck coefficient based on thermodynamic considerations. Consider a junction of two conductors through which one coulomb of charge passes at an infinitesimally slow rate such that the current is very small. The entire circuit is assumed to be at constant temperature T such that there is no heat conduction or joule heat loss allowing the system to be treated to be in equilibrium. Since the two conductors are in equilibrium their chemical potentials are equal such that $\varepsilon_{f_1} = \varepsilon_{f_2} = \varepsilon_f$. For a reversible, open system, the conservation of energy equation can be written as

$$U = Ts + \varepsilon_f \quad (39)$$

The average energy U as well as the entropy *s* of the electrons in the two conductors is different. Since the chemical potential of the two conductors us equal, we can write

$$U_1 - Ts_1 = U_2 - Ts_2 \quad (40)$$

When an electron passes through a junction of two conductors its average energy changes by U_1-U_2. This difference in electron energy is generated in the form of Peltier heat $\Pi_{1\text{-}2}$ at the junction.

$$U_1 - U_2 = \prod_{1-2} \quad (41)$$

The relation between Peltier heat and Seebeck coefficient is given by $ST = \Pi_{1\text{-}2}$. From equations 40 and 41 the Seebeck coefficient is obtained as

$$S = \frac{\prod_{1-2}}{T} = \frac{U_1 - U_2}{T} = S_1 - S_2 \quad (42)$$

Equation 42 describes the Seebeck coefficient as the flow of entropy per unit charge across a junction. From this definition and equation 39, the Seebeck coefficient across the junction can be written as

$$S = \frac{1}{e}\left(\frac{\bar{\varepsilon} - \varepsilon_f}{T}\right) \qquad (43)$$

where $\bar{\varepsilon}$ is the average electron energy passing across the junction. If ε is the energy of each electron passing through the junction and *f(ε)* is the distribution function of the electrons, the average electron energy across the junction is calculated as

$$\bar{\varepsilon} = \frac{\int_0^\infty \varepsilon f(\varepsilon) d\varepsilon}{\int_0^\infty f(\varepsilon) d\varepsilon}. \qquad (44)$$

Using Fermi-Dirac statistics to describe electron distribution in near degenerate semiconductors and a constant relaxation time, power-law approximation to describe carrier energy dependent mean free path of the electrons,

$$\bar{\ell} \propto \varepsilon^r \qquad (45)$$

Ioffe calculated the Seebeck coefficient in a semiconductor as

$$S = \frac{k}{e}\left[\left(\frac{r+2}{r+1}\right)\frac{f_{r+1}\left(\varepsilon_f / k_B T\right)}{f_r\left(\varepsilon_f / k_B T\right)} - \frac{\varepsilon_f}{k_B T}\right] \qquad (46)$$

The Fermi integrals in equation 46 are calculated from

$$f_r\left(\varepsilon_f / k_B T\right) = \int_0^\infty \frac{x^r}{e^{\left(x - \varepsilon_f / k_B T\right)} + 1} \qquad (47)$$

where $x = \varepsilon/k_B T$ is the reduced energy for electrons. Ioffe calculated the electrical conductivity through the relation $\sigma = ne\mu$ where *n* is the electron density given by Fermi-Dirac statistics as

$$n = \frac{4\pi\left(2m^* k_B T\right)^{3/2}}{h^3} f_{1/2}\left(\frac{\varepsilon_f}{k_B T}\right) \qquad (48)$$

and μ is the temperature dependent mobility of the electrons. Temperature dependency of mobility was included through the relation $\mu = \mu_0 k_B T^{r+1}$ where μ_0 is the mobility at absolute 0K. Thermal

conductivity was calculated as a sum of the contributions from the electrons as well as lattice vibrations i.e. phonons. The lattice conductivity was obtained from

$$\kappa_{ph} = \frac{1}{3} c v l_p \qquad (49)$$

c is the specific heat obtained from the Debye model, ν is the sound velocity and ι_p is the phonon mean free path. The electron contribution to thermal conductivity was calculated from the general case of the Weidmann-Franz law is given by

$$\frac{\kappa_{el}}{\sigma} = A\left(\frac{k}{e}\right)^2 T \qquad (50)$$

The coefficient A accounts for the various scattering mechanisms and is equal to

$$A = \left[\frac{r+3}{r+1}\frac{f_{r+2}\left(\varepsilon_f / k_B T\right)}{f_r\left(\varepsilon_f / k_B T\right)} - \frac{(r+2)^2}{(r+1)^2}\frac{f_{r+1}^2\left(\varepsilon_f / k_B T\right)}{f_r^2\left(\varepsilon_f / k_B T\right)}\right] \qquad (51)$$

where the scattering parameter r changes depending on the type of scattering. For example, the value of r is -1 for scattering with optical phonons while for ionized impurity scattering, which is predominant in metals, the value of r is determined to be equal to be 2.

In 1959 Chasmar and Stratton [57] used Ioffe's model to calculate the optimum value of the Fermi level that would give the maximum value of ZT for various values of the scattering parameter r. They introduced a material parameter β which was a function of the effective mass and temperature of the system and the classical statistics based low carrier concentration mobility μ_c.

$$\beta = \frac{\frac{2e\left(2\pi m^* k_B T\right)^{3/2}}{h^3}\left(\frac{k_B}{e}\right)^2 T\mu_c}{\kappa_l} \qquad (52)$$

For a given temperature and material parameter, β the optimum value of Fermi energy to maximize ZT was calculated for various scattering parameters r. Their calculations indicated that the value of β and hence the figure of merit ZT must increase as the temperature rises. More importantly their work was the first to identify the impact of bandgap on the figure of merit. While materials with large bandgaps were found to

have low carrier mobility and high thermal conductivity, small bandgap materials would result in low ZT values at high temperatures due to increased minority carrier contribution to thermal conductivity. In addition ionic compounds were considered to be bad thermoelectric materials due to very high polar scattering of electrons decreasing the mobility. Chasmar and Stratton combined their analysis with the results of Goldsmid [22] whose studies on the ratio of mobility to thermal conductivity as a function of the atomic weight led to the discovery of bismuth telluride. From their analysis semiconductors with best values of β between 0.1 and 0.2 and high atomic weight comprised of sulphides, selenides and tellurides of heavy metals such as lead or bismuth. Though these compounds have low bandgap at 0K ($\leq$ 0.22eV), the bandgap increases as the temperature increases. Cadmium telluride on the other hand has a large bandgap, 1.45eV at 300K but the material parameter β is only 0.03-0.06. Based on the above studies Chasmar and Stratton proposed that a combination of cadmium telluride or selenide (large bandgap, small β) with a telluride or selenide of small bandgap and large β would result in a good thermoelectric material.

Attempts to find an upper bound to the figure of merit were made by various researchers. Littman and Davidson [58] used irreversible thermodynamics to show that no upper limit was imposed on ZT by the second law. However, Rittner and Neumark [59] showed that it was important to employ a combination of statistical or kinetic methods with a proper physical model of semiconductors to study the figure of merit. Simon [60] studied the optimum ZT value in two band semiconductors as a function the minimum bandgap η_g, material parameter β for electrons and holes and the scattering parameter *r* for electrons and holes. He defined a parameter $\gamma = (m_e/m_h)^{3/4}(\mu_{ce}/\mu_{ch})^{1/2}$ that he varied by varying the material parameters β_e and β_h. While he could not arrive at a definite upper limit to the value of ZT his theoretical studies of optimum ZT vs. γ for $\eta_g = 0$ showed that very high values of ZT could be achieved in very small bandgap semiconductors by doping.

Significant progress was made in the fifties and the sixties towards analytically calculating the scattering parameters used in the Boltzmann transport equation. The most common modes of scattering included in the BTE were acoustic phonon scattering through the deformation potential put forth by Bardeen and Shockley [6] and the polar-optical mode scattering put forth by Callen in 1949 [61] and Frohlich in 1954

[62]. In the case of elastic scattering such as acoustic phonon scattering and ionized-impurity scattering, the relaxation time approach that characterizes the rate at which momentum decays can be used to solve the BTE. However in the case of inelastic scattering no relaxation time exists and hence other methods to solve the BTE were developed such as the variational calculations approach put forth by Kohler in 1948 [63], the iteration method by Rode in 1970 [64] and the matrix method by Kranzer in 1971 [65]. Meanwhile Kane in 1957 [66] determined accurately the structure of the lowest (000) conduction band minima at the center of the Brillouin zone as well as the wave functions in that valley. Using Kane's model of the band structure and electron wave functions, Rode calculated the electron mobility in intrinsic, direct gap, polar, non-degenerate semiconductors using Maxwellian statistics. He included the three scattering mechanisms i.e. acoustic deformation potential scattering, polar optical phonon scattering and piezoelectric scattering which he identified as the most important mode of scattering for lower lattice temperatures such as for e.g. below 60K in GaAs. The electron distribution function under the influence of a small electric field is described as a linear finite-difference equation, which was solved using a numerical iteration method. The mobilities resulting from using parabolic vs. non-parabolic bands described by Kane were compared. Non-parabolicity affected the calculated mobility by only 10% in wide bandgap material such as GaAs while small bandgap material such as InSb showed a 50% decrease in the calculated mobility when non-parabolicity was included. Good match between the predicted and measured mobility data was seen for GaAs between the temperature ranges of 150K to 400K. While the poor match with measured data at high temperatures could not be explained, the results below 150K were attributed to the non-inclusion of impurity scattering in the model which becomes prominent at low temperatures. In 1971 Rode [67] extended the previous study to calculate mobility and thermoelectric power in degenerate direct-gap, polar semiconductors using Fermi-Dirac statistics. In addition to piezoelectric scattering, longitudinal acoustic phonon scattering and polar-optical phonon scattering, ionized-impurity scattering and heavy hole scattering were also included in the calculations. Thermoelectric power was calculated from the short-current calculated from the perturbation distribution where the field is set equal to zero.

$$Q = -\frac{\left(\frac{1}{e}\nabla\varepsilon_f + \frac{J}{\sigma}\right)}{\nabla T} \qquad (53)$$

Mobility and thermoelectric power were compared with experimental data for intrinsic InSb, InAs and InP. There was good agreement with measured mobility data for all three semiconductors above room temperature while below room temperature the mobility showed two orders of magnitude decrease compared to experiments. Electron-hole scattering was prominent above room temperature, polar mode inelastic scattering dominated at room temperature while impurity scattering was dominant below room temperature. Below 60K in InSb and 80K in InAs, deformation potential acoustic mode scattering and piezoelectric scattering dominate electron mobility. Good agreement with experimental data was also seen in the case of thermoelectric power for various electron concentration levels at room temperature. However, for higher temperatures, the thermoelectric power showed slight deviation from experiments where multi-valley conduction was suspected to dominate electron transport.

Sofo and Mahan in 1994 [68] extended Rode's work to study the optimum bandgap in direct bandgap semiconductors. Non-parabolicity was included using the two-band Kane model and the solution to the BTE was obtained using Rode's iteration method in the Gauss-Siedel formulation because inelastic scattering was included. Comparisons were made between ZT values for parabolic bands and non-parabolic bands with either elastic ionized impurity scattering or inelastic polar optical phonon scattering. They found that the dependence of ZT on the bandgap Eg fell into two regimes. For $Eg < 6k_BT$ the value of ZT decreased with decreasing bandgap due to the increasing presence of minority carriers. For $Eg > 10k_BT$ the value of ZT either increased or decreased depending upon the type of scattering involved. Additionally they found that the most important effect of non-parabolicity was to modify the effective mass values that in turn changed the value of the material parameter B_0 present in the expression for ZT similar to the parameter B in Chasmar and Stratton's model. Mahan determined that in order to obtain higher ZT values the value of B_0 need to increase implying that materials with higher effective masses or reduced thermal conductivity κ needed to be researched.

Development of Low-Dimensional Models for Thermoelectric Applications

The concept of monocrystalline semiconductor structures having a periodic potential in one-dimension was proposed by Esaki and Tsu in 1970 [69] who called these structures *superlattices*. They suggested that the periodic potential could be obtained by periodic variation of alloy composition or variation of impurity density during epitaxial growth out of materials such as Si, Ge and their alloys, III-V, II-VI, compounds and their alloys etc. The dispersion relation in the direction parallel to the superlattice planes was assumed to be parabolic while in the cross-plane direction they used a sinusoidal approximation in the form of Mathieu's equation [70].

$$E\left(k_{\parallel},k_{\perp}\right)=\frac{\hbar^2 k_{\parallel}^2}{2m^*}+t\left(1-\cos\left(k_{\perp}d\right)\right) \quad (54)$$

where d is the superlattice period and t is the amplitude of the superlattice periodic potential. The authors found that under moderate electric fields in the cross-plane direction the confined energy bands and wave vector zones would result in a negative conductance that could lead to new ultra-high frequency oscillators. The negative conductivity will arise from the fact that electrons traveling perpendicular to the superlattice would experience negative effective mass beyond the inflection point in the sinusoidal dispersion relation. In 1984 Friedman [71] proposed that the low temperature ($k_BT<\mu$) thermoelectric power S of a superlattice as a function of dopant concentration can be used to provide information about the one-electron density of states and the location and width of the mini-bands. Following Wilson's model for calculating thermoelectric power using Fermi-Dirac statistics in the BTE and assuming energy-independent momentum scattering rates, they showed mathematically that the thermoelectric power tends to diverge at the mini-band extrema. The divergence in S is smoothed out for energies greater than k_BT but they were still discernible for low temperatures. In addition, anisotropy in the thermoelectric power was predicted for in-plane vs. cross-plane temperature gradient. For the next couple of years the low-temperature thermoelectric power of superlattices was predominantly used as a tool to understand the electronic structure and transport properties of superlattices [72, 73] as well as the scattering dynamics of electrons and phonons in solids [74, 75].

In 1992, Mensah and Kangah [76] used the relaxation time approximation (RTA) model of the BTE with the sinusoidal dispersion relation for the confined direction of superlattices to obtain analytical expressions for the Seebeck coefficient and thermal conductivity of superlattices along the superlattice cross-plane direction. Defining 2Δ as the width of the lowest energy mini-band in the *E vs. k* regime, the thermopower and thermal conductivity are calculated for two ranges of Δ. For $\Delta << k_BT$, the electrons in the superlattice are said to behave as a 2D electron gas while for $\Delta >> k_BT$ the electrons behave as a 3D gas. They suggested that by an optimal selection of Δ and *d*, the superlattice period it is possible to obtain good-quality and efficient thermoelements. In 1993, Dresselhaus and Hicks [77] proposed that by layering highly anisotropic thermoelectric materials such as Bi_2Te_3 alloys in the form of superlattices would make it possible to increase the figure of merit provided that the superlattice multilayers are made in a particular orientation. The model of the superlattice proposed by the authors involved layers of thin films with no barrier layers such that confinement effects originated only due to electron confinement in the thin films. They theorized that in addition to confinement effects that cause electrons to behave as a 2D gas, the layering would reduce thermal conductivity through phonon scattering and thus increase ZT. The layers were assumed to be parallel to the x-y plane where they have a parabolic dispersion and a confined dispersion in the z direction as shown in equation 55 which unlike the sinusoidal dispersion used in the previous papers, treats the lowest subband in the well to be flat similar to electrons confined in an infinite potential well.

$$\varepsilon\left(k_x,k_y\right)=\frac{\hbar^2k_x^2}{2m_x^*}+\frac{\hbar^2k_y^2}{2m_y^*}+\frac{\hbar^2\pi^2}{2m_z^*a^2}\ \text{where } a \text{ is the layer thickness.} \qquad (55)$$

Using the dispersion relation and the equations for S, σ and κ_{el} and κ_{ph} specified by Rittner [43] they calculated the figure of merit ZT for transport along the x-axis in terms of the reduced Fermi energy ε_f^* and a material parameter B described in equation 56.

$$\varepsilon_f^{\,*}=\frac{\left(\varepsilon_f-\frac{\hbar^2\pi^2}{2m_z^*a^2}\right)}{k_BT}\ \text{and}\ B=\frac{1}{2\pi a}\left(\frac{2k_BT}{\hbar^2}\right)\left(m_xm_y\right)^{1/2}\frac{k_B^2T\mu_x}{e\kappa_{ph}} \qquad (56)$$

The authors analyzed that the value of $Z_{2D}T$ can be increased by using narrower layers that will ensure increased phonon scattering and by choosing optimum current direction and layer orientation to maximize

mobility. The $Z_{2D}T$ values for Bi_2Te_3 were predicted for two orientations of the multilayers, the x-y planes and the x-z planes. The results predicted an increase in ZT by a factor of 13 over the bulk value in the x-z plane for current flow along the x-axis for layers that are 3.8Å thick. In the case of the x-y plane results predicted an increase in ZT by a factor of 3 over the bulk value for layers that are 10Å thick. The dispersion model used in the above paper treats the quantum wells as decoupled such that there is no tunneling between the wells.

Sofo and Mahan [78] analyzed the ZT predictions of a superlattice put forth by Hicks and Dresselhaus by incorporating alternating barrier layers having finite thermal conductivity in the superlattice and introduced a tunneling probability between the quantum wells in their calculations. They argued that quantum mixing between the wells due to tunneling leads to a broadening of the density of states from 2D to 3D. In addition, the finite thermal conductivity of the barrier region produces a parasitic effect of backflow of heat that would hinder the pumping of heat in the well. The authors used the RTA model to include electron density dependence on the electrical conductivity through the expression given by Wilson [45].

$$\sigma = n\left(e^2\tau / m_x \right) \quad (57)$$

The dependence of the electrical conductivity on electron density ensures that if the well width a and chemical potential ε_f are kept constant, just by increasing the barrier width b, the electron density will decrease due to reduced tunneling probability causing the electrical conductivity to decrease and decrease ZT. Alternately, for a fixed barrier width, as the well width is reduced, the two-dimensional density of states increases and proportionately increases the electrical conductivity as well as ZT. The thermal conductivity equation was also modified to include heat backflow at the barriers in the thermal conductivity. In addition they changed the value of B to be inversely proportional to the superlattice period d and not the well thickness a. Sofo and Mahan used their model to predict the ZT vs. well width values for Bi_2Te_3 layers in the x-y plane with transport along the x-axis. Using average values in the literature for the mobility μ_x and thermal conductivity κ, they found that there was improvement in ZT due to the enhancement of density of states at the bottom of the lowest subband with decreasing well width but the amount of increase was not as high as originally predicted by Dresselhaus and Hicks. The change in ZT

with decreasing well width was studied as a function of the barrier width. In all cases except for a 20Å wide barrier the ZT values increase with decreasing well thickness. The decrease in ZT for the 20Å barrier was attributed to tunneling through the barrier that causes quantum coupling between the wells leading to broadening of density of states making the 2D density of states to become 3D density of states and reduce ZT. The authors also point out that the flat subband assumption works well when the Fermi level lies above the subband at a distance greater than the value of k_BT as electrons above and below the Fermi level have opposite contribution to the thermopower. Similar studies on the effect of tunneling and finite thermal conductivity contribution of the barrier material were done by Broido and Reinecke [79] in 1995 who studied the effects of confinement on the figure of merit of Bi_2Te_3 superlattices using Kronig-Penny type subband energy dispersion in the RTA model. They too found that the value of ZT_{2D} increased as the well width decreased until tunneling between wells caused the value of ZT_{2D} to reduce for further decrease in well width.

In 2001 Broido and Reinecke [80] extended the BTE model with Kronig-Penny subbands to calculate thermoelectric coefficients in quantum well and quantum wire superlattices. The thermoelectric coefficients were calculated for the occupied subbands in each conduction band valley neglecting inter valley scattering. The results for each valley were summed over all the multiple ellipsoidal conduction band valleys to obtain the overall thermoelectric coefficients. Elastic acoustic phonon scattering through the deformation potential scattering and inelastic optical phonon scattering using the solution to the inelastic 3D Boltzmann transport equation were included in the calculations. Optical phonons were assumed to be dispersionless with the dominant phonon energy to be the value of its zone center $\hbar\omega_0$. The BTE solution for inelastic scattering was obtained by using an extension of Ritz's iterative method [81]. The thermoelectric coefficients were compared to the results of the constant relaxation time approximation (CRTA) and bulk values as a function of decreasing well width. In general, solutions based on the CRTA were found to predict much higher values for mobility compared to the inelastic solution. Power factor predictions made by both CRTA and inelastic scattering methods predicted lower values than the bulk which were attributed to electron confinement in the wells leading to reduced conductivity. The power factor values increased with decreasing well width due to increase in the 2D density of states and

eventually matched the bulk power factor. However, further decrease led to electron tunneling that changed the 2D density of states to 3D lowering the power factor. These effects as seen previously were not captured by the CRTA model. The effect of scattering and bandstructure on the thermoelectric performance was demonstrated through the power factor studies done on two materials, PbTe and GaAs. PbTe has an anisotropic multivalley bandstructure while GaAs has a single isotropic conduction band valley. At room temperature both acoustic-phonon and optical-phonon scattering dominate in PbTe while only optical-phonon scattering dominates in GaAs. Accordingly the full solution of the BTE including elastic acoustic phonon and inelastic optical-phonon scattering showed an increase of only a factor of two in the power factor of PbTe compared to its bulk value while GaAs showed a factor of 9.5 increase in its power factor.

The ability to incorporate the full bandstructure information to calculate the thermoelectric coefficients was demonstrated by Sofo et al. in 2003 [82] when they presented a method of calculating the electronic structure from first principle calculations, which they included in the relaxation time approximation to calculate the transport coefficients. They defined a kernel of all transport coefficients known as the *transport distribution* that contains all the electronic information needed to obtain the thermoelectric coefficients directly for any given material.

$$\Xi = \sum_{\vec{k}} \vec{v}_{\vec{k}} \vec{v}_{\vec{k}} \vec{\tau}_{\vec{k}} \ . \quad (58)$$

The group velocity values are obtained using the linear augmented plane wave (LAPW) method while the relaxation times are calculated for various scattering mechanisms using parameters found in literature. Doping was included by changing the relative position of the Fermi level under the assumption that the bandstructure remains unchanged as the Fermi level changes. The above method was used to calculate the thermoelectric coefficients for Bi_2Te_3 using experimentally determined thermal conductivity values for the various planes. The Seebeck coefficient for all doping levels was calculated using a constant relaxation time that gave the best fit with experimental data in the intrinsic region. For all doping levels, the Seebeck coefficient of the n-type material showed a better fit with experiments compared to the p-type. The model also captured effectively the anisotropy in the electrical conductivity of Bi_2Te_3 where the conductivity along the basal plane can be four times greater than the conductivity along the trigonal axis. The

predictions for the figure of merit however did not show very good match with experiments with results for the n-type matching better than those for the p-type. Similar match with experimental data was obtained by Lee and Allmen in 2006 [83] who calculated the thermoelectric coefficients using a tight-binding model with $sp^3d^5s^*$ orbitals, nearest neighbor interactions and spin orbit coupling for Bi_2Te_3 in the constant relaxation time approximation model.

Nanostructured Thermoelectric Materials

The interest in nanoscale structures for thermoelectric applications was motivated by the increase in density of states per unit volume with shrinking device dimensions, seen here in figure 7, while the thermal conductivity can be decreased due to phonon confinement [3, 4] and phonon scattering at the material interfaces in the superlattices[4,5,6]. Semi-classical models used to predict the electrical conductivity showed no significant decrease in the electrical conductivity of nanofilms and nanowires [2, 5, 7, 8, 77, 79]. However, experiments have not been able to match the predicted improvements in the figure of merit [2, 9]. Hence it is very evident that shrinking device dimensions present an increasing need for a quantum transport model that can also effectively couple quantum effects and scattering effects. The need to incorporate scattering stems from the fact that while electron-phonon scattering usually helps restore thermodynamic equilibrium, shrinking device dimensions may not ensure enough scattering to restore equilibrium. The simultaneous consideration of scattering effects, which is usually described as particle behavior, and quantum effects, which are wave in nature, is confounding and computationally intensive. In this regard the non-equilibrium Green's function formalism provides a framework for coupling quantum effects and thermal effects to model electron transport in thermoelectric devices. Open boundary conditions allow the source and drain contacts to be coupled to the device through simple self-energy terms. In addition, the NEGF formalism *does not* require a statistical distribution of carriers within the device thus allowing for the rigorous incorporation of both elastic and inelastic scattering effects using the concept of Buttiker probes [84]. A brief synopsis of the formalism is presented in the next chapter while a more thorough and detailed development can be found in [16] and [84].

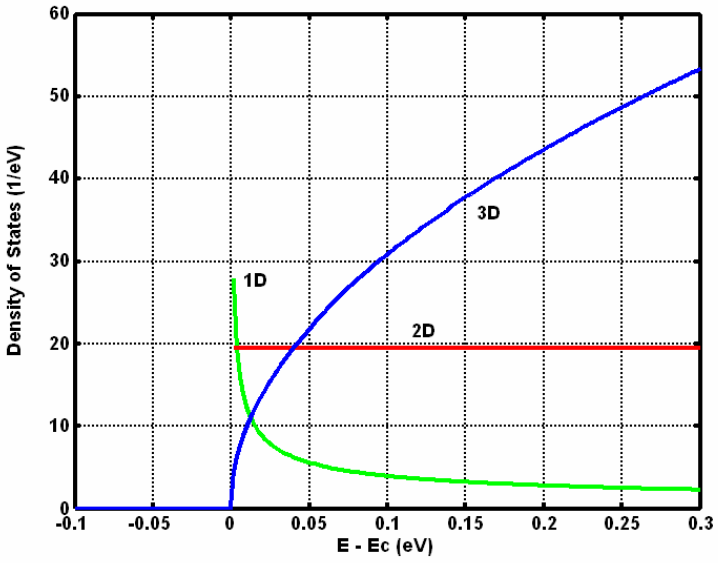

Figure 7. Distribution of density of states per unit volume with respect to energy of 3D , 2D and 1D structures

CHAPTER III

THE NEGF FORMALISM

In general an isolated device and its energy levels are described using a Hamiltonian H, a Hartree potential U and energy eigen-states of the electron, ε_α.

$$\left(H+U\right)\psi_\alpha\left(\vec{r}\right)=\varepsilon_\alpha\psi_\alpha\left(\vec{r}\right) \quad (59)$$

The potential U is obtained using Poisson's equation and accounts for the effect of any change in the electron density matrix on the channel capacitance. The channel capacitance consists of an electrostatic capacitance that depends on the dielectric constant ε_r and a quantum capacitance which depends on the density of eigen states in the channel [16]. In general, the electron density matrix in real space is given by

$$\left[\rho(\vec{r},\vec{r'};E)\right]=\int_{-\infty}^{+\infty} f\left(E-E_f\right)\delta\left(\left[EI-H\right]\right)dE\,. \quad (60)$$

Here $\delta(EI-H)$ is the local density of states. We write the standard expansion for the delta function as

$$\delta\left(EI-H\right)=\frac{i}{2\pi}\left(\left[\left(E+i0^+\right)I-H\right]^{-1}-\left[\left(E-i0^+\right)I-H\right]^{-1}\right) \quad (61)$$

Equation 61 can also be written in the form

$$\delta\left(EI-H\right)=\frac{i}{2\pi}\left[G\left(E\right)-G^+\left(E\right)\right] \quad \text{where } G\left(E\right)=\left[\left(E-i0^+\right)I-H\right]^{-1} \quad (62)$$

$G(E)$ is the retarded Green's function while $G^+(E)$, its conjugate complex transpose, is called the advanced Green's function. In the time domain, the Green's function can be interpreted as the impulse response of the Schrödinger equation where in the present scenario the impulse is essentially an incoming electron at a particular energy. In the energy domain the Green's function gives the energy eigen-values for the eigen-states that are occupied in response to the applied impulse. The diagonal elements of the spectral function, which is the difference between the retarded and advanced Green's function, represent the available local electron density of states.

$$A\left(\vec{r},\vec{r}';E\right)=2\pi\delta\left(EI-H\right)=\left[G\left(E\right)-G^{+}\left(E\right)\right] \qquad (63)$$

The electron density in the channel is the product of the Fermi function and the available density of states and for an isolated device is written as

$$\rho\left(\vec{r},\vec{r}';E\right)=\int_{-\infty}^{+\infty} f\left(E-E_f\right)\left[A\left(E\right)\right]\frac{dE}{2\pi} \qquad (64)$$

The real portion of the diagonal elements of the density matrix, represent the electron density distribution in the channel. This electron density represented as *n* is used in the Poisson's equation to self-consistently solve for the potential in the channel where N_d is the donor density and ε_r is the permittivity of the channel.

$$\nabla^2 U=-\frac{q}{\varepsilon_r}\left(N_d-n\right) \qquad (65)$$

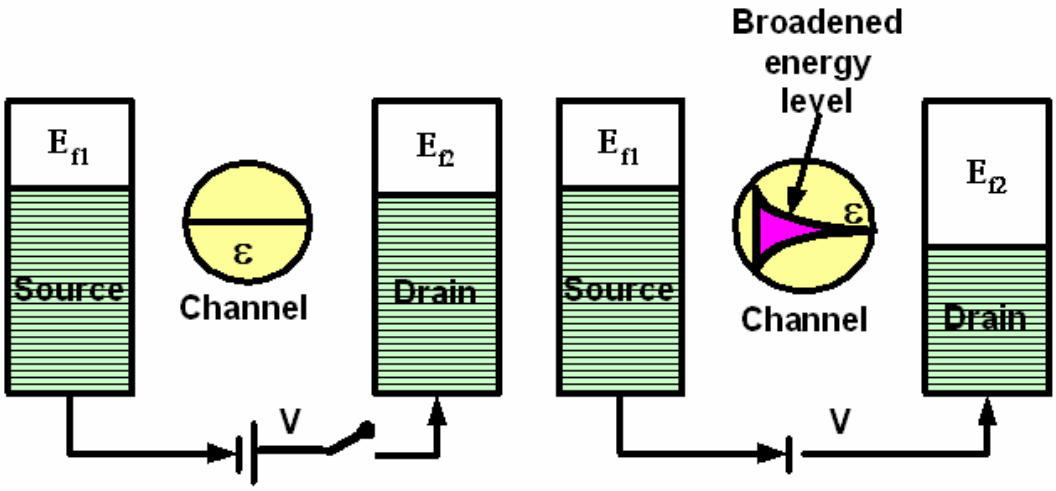

Figure 8. (a) Single energy level of an isolated channel (b) Broadening of electron energy levels in the channel when connected to contacts

To understand the process of current flow, consider an isolated device having a single energy level ε as seen in figure 8a. The source and drain contacts have an infinite distribution of electronic energy states. When the isolated device with single energy level ε is connected to the source and drain contacts, some of the density of states around this energy level ε will spill over from the contacts into the channel. This process is known as energy level *broadening* and is shown in figure 8b. Since the Fermi levels in the source and drain are equal, the amount of broadening will be equal on both sides and hence the net current flow in

the channel will be zero. When a positive bias is applied on the drain side, the Fermi level on the drain side is lowered according to equation 66, opening up states below the channel energy level ε in the drain.

$$E_{f2} = E_{f1} - qV_D \qquad (66)$$

The electrons entering the channel with energy ε now have states with lower energies available in the drain to escape to. This causes the channel current to become non-zero. As the applied bias is increased linearly, more and more states between ε and ε_{f2} become available to remove electrons from the channel causing the source to increase its supply of electrons into the channel. This phenomenon results in a linear increase of current in the channel. Eventually, the difference in the channel energy level ε and the drain Fermi level ε_{f2} is so great that there are no additional states around the energy ε in the drain for the channel electrons to escape. The current reaches saturation such that the number of electrons leaving the drain will equal the number of electrons entering from the source. This process also explains why experimental measurements [85] have shown that the maximum measured conductance of a *one-energy* level channel approaches a limiting value $G_0 = 2q^2/\hbar = 51.6(K\Omega)\text{-}1$.The above analogy of a one-energy level system is applicable to nanoscale thin films and wires where available energy levels along the confined dimension are very limited in addition to being spaced far apart from adjacent energy levels.

In the NEGF formalism the coupling of the device to the source and drain contacts is described using self-energy matrices Σ_1 and Σ_2. The self-energy term can be viewed as a modification to the Hamiltonian to incorporate the boundary conditions. Accordingly, equation 59 and 62 can be rewritten as

$$\left(H + U + \sum_1 + \sum_2\right)\psi_\alpha\left(\vec{r}\right) = \varepsilon_\alpha \psi_\alpha\left(\vec{r}\right) \quad (67)$$

$$G\left(E\right) = \left[\left(E - i0^+\right)I - H - \sum_1 - \sum_2\right]^{-1} \qquad (68)$$

The self-energy terms Σ_1 and Σ_2 originate from the solution of the contact Hamiltonian. In this semi-infinite system, which is connected to the channel, there will be an incident wave from the channel as well as a reflected wave from the contact. The wave function at the interface is matched to conserve energy resulting in the boundary condition,

$$\Sigma_j = -t\exp\left(ik_j a\right) \qquad (69)$$

where t, the inter-unit coupling energy resulting from the discretization is given by

$$t = \frac{\hbar^2}{2m^* a^2}. \qquad (70)$$

Here k_j corresponds to the wave vector of the electron entering from the channel while a corresponds to the grid spacing that will be discussed later in this chapter. The broadening of the energy levels introduced by connecting the device to the source and drain contacts is incorporated through the Gamma functions Γ_1 and Γ_2 given by

$$\Gamma_1 = i\left(\Sigma_1 - \Sigma_1^+\right) \text{ and } \Gamma_2 = i\left(\Sigma_2 - \Sigma_2^+\right) \quad (71)$$

The self-energy terms affect the Hamiltonian in two ways. The real part of the self-energy term shifts the device eigenstates or energy level while the imaginary part of Σ causes the density of states to broaden while giving the eigenstates a finite lifetime. The electron density for the open system is now given by

$$[\rho] = \int_{-\infty}^{+\infty} \left[G^n(E)\right]\left(\frac{dE}{2\pi}\right) \qquad (72)$$

$G^n(E)$ represents the electron density per unit energy and is given by

$$G^n(E) = G(E)\Sigma^{in}(E)G^+(E) \text{ where } \left[\Sigma^{in}(E)\right] = \left[\Gamma_1(E)\right]f_1 + \left[\Gamma_2(E)\right]f_2 \quad (73)$$

For plane wave basis functions, the current through the channel is calculated as the difference between the inflow and the outflow at any given contact.

$$I_j = -\frac{q}{\hbar}\int_{-\infty}^{\infty} trace\left[\Gamma_j A\right]f_j - trace\left[\Gamma_j G^n\right] \quad (74)$$

where the subscript j indexes the contacts. For a two-terminal device $I_1 = -I_2$.

Two kinds of devices are examined in the present work as shown in figure 9. The first is a 2D film with infinite dimensions along the x and y axes (perpendicular to the current flow) while the thickness along the z axis (in the direction of current flow) has nanoscale dimensions (few nanometers). The second device is a nanowire with infinite length in the x direction, while the y and z directions have reduced dimensions. Electrical bias is applied along the confined z direction in the cases of both film and wire. Doping in the

materials is varied by changing the position of the conduction band edge E_c relative to a fixed Fermi level E_f using the relation [86]

$$n = N_c \exp\left(-\frac{\left(E_c - E_f\right)}{k_B T}\right) \qquad (75)$$

N_c is the effective density of states at the conduction band edge. The electrical properties modeled in this thesis are the electrical conductivity and Seebeck coefficient. Both these properties are studied as a function of the doping in the film and wire. Electrical conductivity is calculated as the slope of the current-voltage curves using the relation

$$\sigma_{Film} = \frac{dJ}{dV} L_z \text{ and } \sigma_{Wire} = \frac{dI}{dV} \frac{L_z}{L_y} \qquad (76)$$

The current for the wire is calculated as the current per unit length along the x-axis.

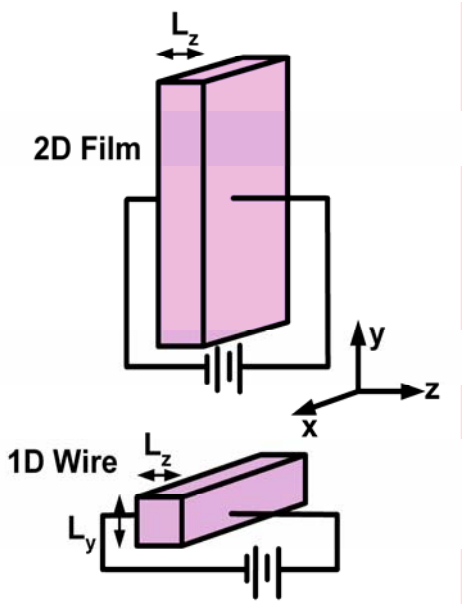

Figure 9. Schematic diagram of 2D thin film and 1D wire with 1D and 2D confinement.

Numerical Scheme

The NEGF model is discretized on a uniform one-dimensional grid with a lattice spacing of a. Transport occurs parallel to the grid, which is also the confined direction. The Hamiltonian used in this thesis is an effective mass Hamiltonian, which averages the effects of the underlying periodic potential of the lattice. The finite difference method is used in place of the Laplacian operator ∇^2 and the resulting Hamiltonian is a discretized N x N tridiagonal matrix given as

$$\nabla^2 = [H] = \begin{bmatrix} E_c + 2t & -t & \\ -t & E_c + 2t & -t \\ & -t & E_c + 2t \end{bmatrix} \quad (77)$$

where t is the coupling energy between adjacent nodes as mentioned in equation 70 and is given in terms of the discretized spacing a and the effective mass m^*. The grid spacing a and grid size N is chosen such that the channel thickness $L=a(N-1)$. The grid spacing a must be chosen such that the coupling energy t is larger than the energy range of integration above the conduction band edge. In order to ensure current conservation, the energy eigenvalues of the Hamiltonian must be real. In order to meet this criterion, the Hamiltonian must be Hermitian. In the case where we are modeling a superlattice, such as Si/Ge/Si, there will be a spatially varying effective mass as well as conduction band edges. The spatial variation of the conduction band edges in the Hamiltonian allows for the automatic inclusion of boundary effects across interfaces. We employ the standard nonlinear control-volume approach [87] and require that the material interface lies at a node to ensure that the Hamiltonian remains Hermitian.

$$[H] = \begin{bmatrix} Ec_A + 2t_A & -t_A & \\ -t_A & Ec_J + t_A + t_B & -t_B \\ & -t_B & Ec_B + 2t_B \end{bmatrix} \quad (78)$$

The Hamiltonian matrix calculated in this way is combined with the self-energy terms in the Green's function to obtain the channel electron density. For the doping levels considered in this paper, the contacts are generally ohmic in nature eliminating the need to model any barrier effects at the source and drain electrodes. The grid size used in the present model consisted of 101 nodes. The resulting size of the Hamiltonian was a 101 x 101 matrix. For an energy range of -1eV to 1 eV, we used 1200 uniform integration steps. In the case of degenerate doping, however, the maximum contribution to current comes

from energy values concentrated near the conduction band edge. In this case, care must be taken to choose an energy range close to the conduction band edge to ensure that the contribution from those energy steps is properly included. The matrix inversion in the Green's function was performed for each integration step, and the integration was performed self-consistently with the potential. This process was repeated for each voltage in the calculated I-V characteristics. To ensure numerical accuracy, first the number of integration steps was selected to ensure a suitable error. Next convergence of the potential calculation was set to an acceptable error. A relaxation of 0.2–0.5 on the density usually allowed convergence in about 10 iterations. The self-consistent approach can be used as long as the value of U_o ($U_o = q^2/\varepsilon_o\varepsilon_r$) as well as the value of the broadening Γ is comparable to k_BT. If U_o exceeds k_BT, the channel goes into the Coulomb blockade regime where the self-consistent method cannot be used anymore to solve for potential. The coupling energy t also has a similar effect as broadening and ensuring that $t \geq U_o$ will keep the channel in the self-consistent field regime. A large t implies that the grid spacing a is small, leading to more delocalization of the electron wave function, which, in turn, improves the accuracy of the self-consistent field calculation.

Calculation of Subband Currents

As mentioned in chapter 1, the electrons in a 2D film can be treated as having infinite range of energies along the x and y axis while being confined along the z-axis which is also the direction of transport.

$$E(k) = E_c + \frac{\hbar^2 k_x^{\,2}}{2m_x^*} + \frac{\hbar^2 k_y^{\,2}}{2m_y^*} + \frac{\hbar^2}{2m_z^*}\left(\frac{n\pi}{L_z}\right)^2 \text{ where n = 1, 2, 3…….} \quad (79)$$

The term $k_z = n\pi / L_z$ is the wave vector corresponding to the confined electrons that form discrete standing waves when confined in an infinite potential well and n is the subband index. For the film we use the 2D Fermi function given in equation 11 that accounts for the infinite states along the x-y plane. Hence, along the transport direction, the electron energy is written as

$$E(k) = E_c + \frac{\hbar^2}{2m_z^*}\left(\frac{n\pi}{L_z}\right)^2 \quad (80)$$

In the NEGF formalism, the energy of each subband is obtained directly by solving for the Eigen values of the Hamiltonian [H]. The conduction band and subsequent subbands are treated as individual, single-energy channels. In the case of ballistic transport where there is no scattering between energy levels, this approach allows us to model electron transport in the device separately for each energy level. Accordingly, current-voltage characteristics are obtained for the conduction band and each additional subband separately. The current thus obtained is summed over all the bands to obtain the net channel current. We start by writing the Schrödinger wave equation along the z-axis as

$$[H]\psi_{nz} = \varepsilon_{nz}\psi_{nz} \qquad (81)$$

The electron energies along the z-axis can be obtained by substituting a plane wave basis for the electron wave function in the Hamiltonian and solving the Schrödinger wave equation along the z-axis using the finite-difference method.

$$\varepsilon_n(k_z) = E_c + 2t\left(1-\cos\left(k_{nz}a\right)\right) \qquad (82)$$

When solved in this way, the value of k_z for an isolated channel will be equal to $n\pi/L_z$ corresponding to standing waves in the channel. When the channel is connected to the contacts, some of the energy density states from the infinite contacts spill over into the channel broadening the energy levels around each energy band in the channel. The wave vectors associated with the broadened energy levels around each band can be obtained by solving the energy conservation equation. For example, the wave vectors corresponding to the broadened energy states around the conduction band E_c are

$$k_z a = \cos^{-1}\left[1-\frac{E-E_c}{2t}\right] \qquad (83)$$

Similarly, wave vectors for broadened states around the first subband are obtained as

$$k_z a = \cos^{-1}\left[1-\frac{E-E_{sub1}}{2t}\right] \text{ and so on.} \qquad (84)$$

For each energy band, the channel current-voltage characteristics are obtained independently until the contribution by any additional subbands is negligible. The final channel current at a particular voltage is obtained as the sum of the currents of the conduction band and the contributing subbands.

Incorporating Electron-Phonon Scattering in the NEGF

In addition to the source and drain contacts electrons can scatter into and out of the channel by either phonon absorption or phonon emission such that $\varepsilon_n - \varepsilon_m = \hbar\omega$. The transition of the electrons from ε_n to ε_m and vice versa is dependent on the transition rate *S(k, k')* which is obtained using Fermi's Golden Rule as explained in chapter 1. This coupling can be expressed through a broadening term Γ which is related to the transition rate S (refer equation 15) as

$$\frac{\Gamma}{\hbar} = S(k,k') \quad \text{where} \quad \begin{aligned} \Gamma_{nn} &= 2\pi \left|K_{mn}^{em}\right|^2 (N+1)\delta(\varepsilon_n - \varepsilon_m - \hbar\omega) \\ &+2\pi \left|K_{mn}^{ab}\right|^2 (N)\delta(\varepsilon_n - \varepsilon_m + \hbar\omega) \end{aligned} \tag{85}$$

The broadening term obtained through Fermi's Golden Rule is similar to the broadening term in the NEGF which is expressed as

$$\Gamma_s = \int \frac{d(\hbar\omega)}{2\pi} \begin{bmatrix} S_o^{em}(N_\omega + 1)\left[G^p(E-\hbar\omega) + G^n(E+\hbar\omega)\right] + \\ S_o^{ab}(N_\omega)\left[G^n(E-\hbar\omega) + G^p(E+\hbar\omega)\right] \end{bmatrix} \tag{86}$$

$G^n(E)$ is the electronic density of states and $G^p(E)$ is the hole density of states and correspond to the $\delta(\varepsilon_n - \varepsilon_m \pm \hbar\omega)$ terms while S_o corresponds to the value $|K_{mn}|^2$ terms for emission and absorption of phonons in equation 85. For the case where electrons in the channel scatter with a phonon of single frequency, the broadening term can be simplified to

$$\Gamma_s = S_o \begin{bmatrix} (N_\omega + 1)\left[G^p(E-\hbar\omega) + G^n(E+\hbar\omega)\right] + \\ N_\omega\left[G^n(E-\hbar\omega) + G^p(E+\hbar\omega)\right] \end{bmatrix} \tag{87}$$

Since the imaginary part of the self energy term is responsible for broadening, the scattering self-energy $\sum_s$ can be expressed using equation 87 as

$$\sum_s = -i\frac{\Gamma_s}{2} \tag{88}$$

The value of S_o for a single phonon of energy $\hbar\omega_o$ is obtained as a sum over all phonon wave vectors β in the Brillouin zone as

$$S_o = \sum_{\beta} \frac{D_o^2 \hbar^2}{2\rho\Omega(\hbar\omega_o)} = \frac{D_o^2 \hbar^2}{12\pi^2 \rho(\hbar\omega_o)} \left(\frac{\pi}{a}\right)^3 \qquad (89)$$

ρ is the mass density, ω_o the phonon frequency and D_o is the optical deformation potential and a, the lattice constant. An example of single-phonon scattering is g-type intervalley longitudinal optical-phonon scattering of electrons from the [001] valley into the [00$\bar{1}$] valley in silicon [15]. The scattering self energy is included in the Green's function seen in equation 68 as an additional contact that scatters electrons into and out of the channel such that the net current through the scattering contact is zero.

$$G(E) = \left[\left(E - i0^+\right) I - H - \Sigma_1 - \Sigma_2 - \Sigma_s\right]^{-1} \qquad (90)$$

CHAPTER IV

RESULTS FOR SILICON NANO-FILMS AND NANO-WIRES

The NEGF method is used to calculate the current density of silicon films for varying thickness under a constant applied field of 10^6 V/m. The current density is for each film is calculated for two cases 1) ballistic electron transport through the film and 2) electrons scattering with longitudinal optical phonons. The results are shown in figure 10 and demonstrate the three fundamental aspects of electron transport in nanoscale devices. The calculated current is very small for small film thicknesses and increases as the film thickness increases. This is the effect of electron confinement where very small film thickness leads to the formation of discrete subband energies that are spaced far apart in the energy space of the Brillouin zone. The electrons in thin films have very limited number of subbands available for transport leading to low current density.

The second important effect is the impact of electron-phonon scattering on the current density. Scattering in the NEGF model is included such that electrons scatter within the broadened energy levels at each energy band. Intersubband scattering is not modeled in this research. Since very small films have limited subbands that contribute to current flow, the effect of scattering is also limited to very few subbands. As a result, the effect of scattering is less than 10% for film thicknesses up to 5nm. As the film thickness increases, the subband energies are spaced closer to each other leading to increased contribution to current flow. In addition the subbands are also lower in energy as they come closer to the conduction band edge As a result, there is a higher probability for the electrons to scatter that begins to gain significance for film thicknesses greater than 5nm where the decrease in current is now 12% of the ballistic current.

The limited impact of scattering on the current demonstrates the third important effect i.e. the nonequilibrium nature of electron transport in silicon films with thicknesses equal to or less than 5nm to 7nm. Scattering with phonons is a way of restoring equilibrium in a system. If the electrons experience very

limited scattering with phonons, they are in a state of non-equilibrium and Fermi-Dirac statistics may no longer be applicable to describe electron distribution.

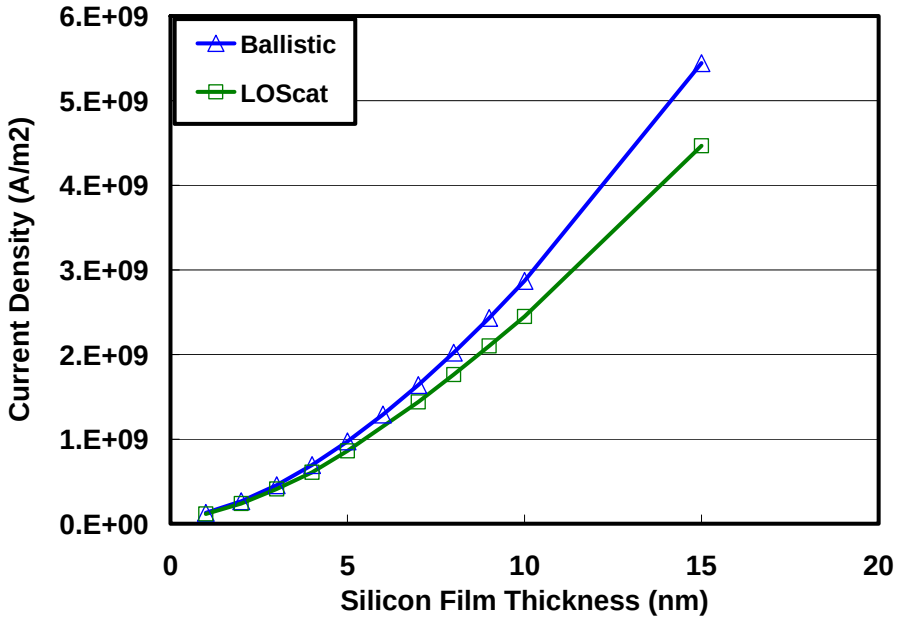

Figure 10. Current density vs. thickness of silicon films doped to $10^{18}cm^{-3}$ for (a) ballistic electron transport and (b) electron transport with longitudinal optical-phonon scattering.

Effect of Electron Confinement on Seebeck Coefficient of Silicon Films and Wires

The NEGF is used to calculate the Seebeck coefficient, electrical conductivity and power factor of ballistic silicon 6nm and 12nm films and 6nm x 6nm wire. The Seebeck coefficient for the silicon film and wire was calculated by applying a temperature gradient along the z-axis. This was achieved by keeping the source temperature constant at 300K while changing the drain temperature in increments of 10K from 300K to 330K. The applied bias ranged from 0 to 0.1V. Figure 11 shows the current-voltage characteristics for a ballistic silicon 6nm film doped to a concentration of $5x10^{18}cm^{-3}$. At low bias conditions, the higher temperature at the drain results in diffusion of electrons from the drain towards the source, opposing the direction of the bias leading to negative current values. As the applied bias is increased, more electrons from the source drift towards the drain and at a particular voltage, which we call the Seebeck voltage; the diffusion of electrons from the drain to the source is balanced by the drift current from the source to the

drain leading to zero current. The Seebeck voltage obtained for each temperature gradient is divided by that value of the gradient to obtain the Seebeck coefficient. The current-voltage characteristics were calculated for the conduction band and 2 contributing subbands in the case of the 6nm film and 6 subbands in the case of the 12nm film. The very high electron confinement in the wire led to current contribution only from states around the conduction band edge.

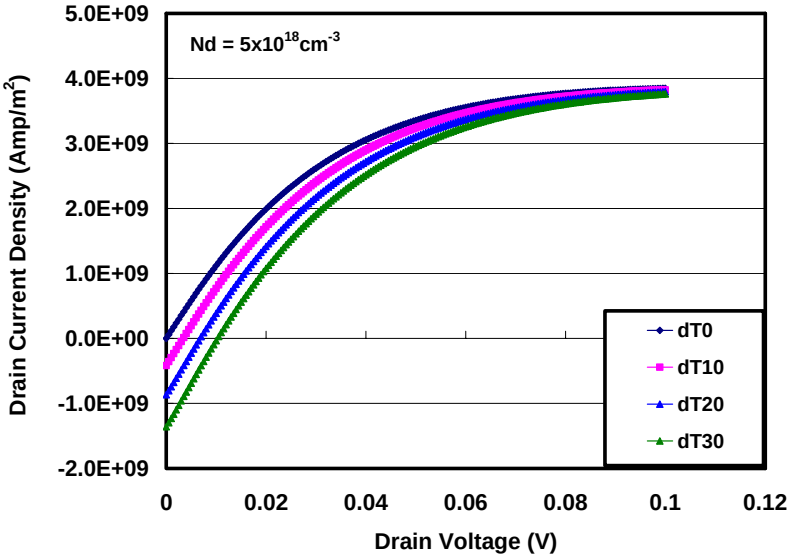

Figure 11. Current-voltage characteristics of a ballistic silicon 6 nm film with doping of $5x10^{18}cm^{-3}$. Applied temperature gradient ranges from 0K to 30K.

Figure 12 shows the predicted and measured Seebeck coefficient values for silicon 2D film and 1D wire for various doping levels. The states around the Fermi level contribute towards the electrical properties of a material. In the case of low doping, the conduction band edges and the subsequent subband energy levels are located at a few eV above the Fermi level as seen in figure 13. For example, for a doping of $10^{16}cm^{-3}$, the value of the conduction band edge Ec is 0.306eV. For current to flow through a channel with this doping, the applied bias must be high enough to reach states around Ec for the drift current to equal the diffusion current. Accordingly, the value of the Seebeck voltage will be high leading to high Seebeck coefficients. For high doping, the conduction band edge is closer to the Fermi level causing the Seebeck coefficient to be lower with increased doping.

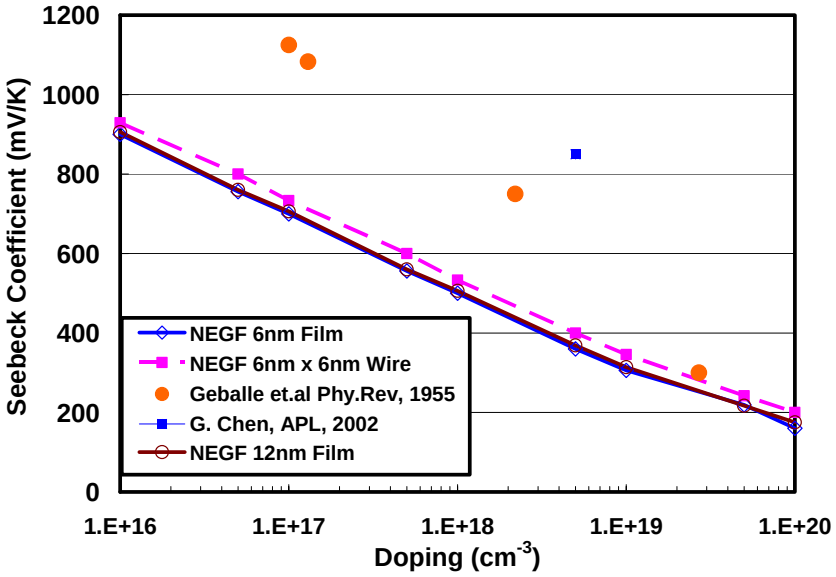

Figure 12. Seebeck coefficient of ballistic silicon films and wires calculated using NEGF and compared to experiments [88, 89].

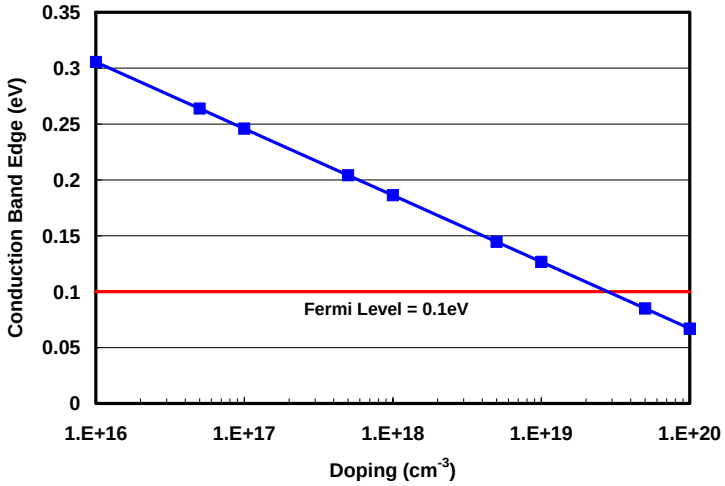

Figure 13. Change in conduction band edge with doping for silicon

The limited states available around the Fermi level is also the reason the Seebeck coefficient remains constant with size. For high doping, the conduction band edge is close to the Fermi level where confinement effects are more dominant due to increase in density of states per unit volume around the Fermi energy. Even here, while confinement causes the increase in density of states per unit volume to be

higher for thinner films, the electron energy levels are few and far between to lead to any significant impact on the Seebeck coefficient. As the film thickness increases, the number of energy levels around the Fermi energy increases and are also spaced closer to each other causing the Seebeck coefficient to increase with film thickness. This effect is evident from figure 14, where the Seebeck coefficient is no longer constant with film thickness for doping of $1x10^{19}$ cm^{-3} to $1x10^{20}$ cm^{-3} and for a given doping, increases as the film thickness increases.

The effect of confinement is more evident from the 2D film to the 1D wire as seen from the increase in the Seebeck coefficient of the wire by approximately 30μV/K compared to the film for the same doping level. The effect of increase in the local density of states per unit volume near the Fermi energy is greater in the wire compared to the film. As a result, for a particular doping, more carriers occupy higher energy states in the wire compared to the film causing an increase in the value of the voltage for which the thermally induced current is balanced by the field current. The experimental values for the Seebeck coefficient were measured for bulk silicon over a wide range of temperatures while the values used here are an average for the temperature range of 300K to 330K. Since silicon is not a good thermoelectric material there is limited experimental data for the Seebeck coefficient of silicon nanofilms and nanowires. However, the predicted values of S for the film match the experimental trends [88].

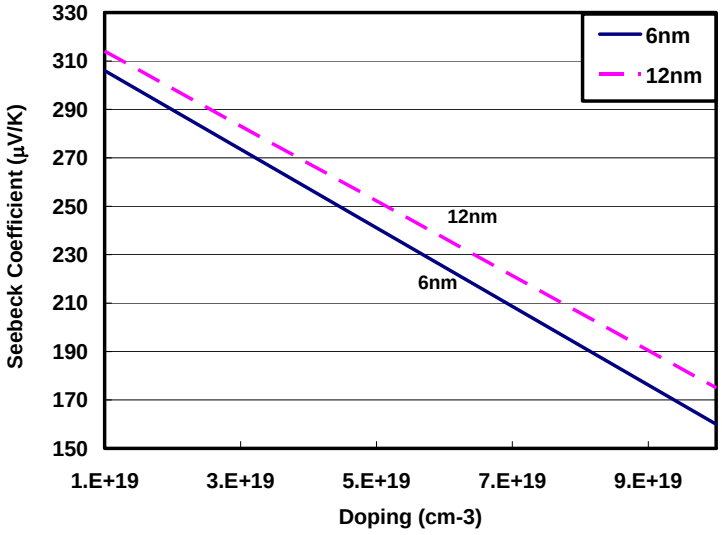

Figure 14. Seebeck coefficients for 6nm and 12nm ballistic silicon films for high doping values

Effect of Electron Confinement on Electrical Conductivity of Silicon Films and Wires

Figure 15 shows the electrical conductivity values as a function of doping for 6nm and 12nm silicon films as well as a 6nm x 6nm silicon wire obtained using the NEGF formalism. When the number of bulk dimensions is reduced from 2D to 1D electron confinement is increased from 1D to 2D as in the case of the 6nm x 6nm wire causing a 33% decrease in conductivity. Confinement of electrons increases the spacing between adjacent subband energy levels leading to a quadratic increase in the electrical conductivity with size. Figure 16 shows the subband energies of 6nm and 12nm silicon films doped to a concentration of $10^{18}cm^{-3}$ corresponding to Ec of 0.1863eV. The subband energies considered here ranged from Ec to 2 eV in the Brillouin zone. It can be seen from figure 16 that the value of the subband energies of the 6nm channel are higher than that of the 12nm channel and are also spaced farther apart from each other. For the energy range considered, the 12nm channel has double the number of electron subbands compared to the 6nm channel leading to a factor of 3.5 decrease in the conductivity of the 6nm film compared to the 12nm film. Also, as seen in figure 13, high doping brings the conduction band edge closer to the Fermi level. As the film thickness increases, the number of energy levels around the Fermi energy increases and are also spaced closer to each other causing the electrical conductivity of the 12nm film to increase with film thickness. In reality and as seen from figure 10, as the size of the film increases, transport is no longer ballistic and the conductivity is expected to reach a maximum before starting to reduce with increase in size due to the dominance of scattering.

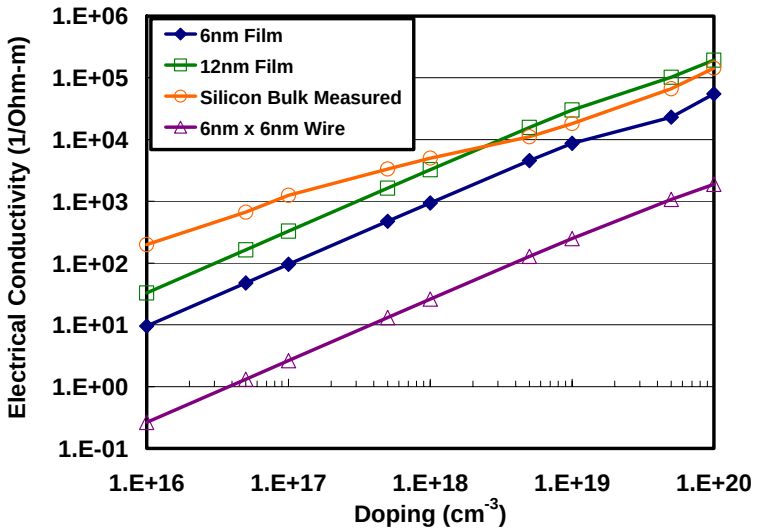

Figure 15. Predicted and measured [90] electrical conductivity values for a ballistic Silicon 6nm and 12nm film and 6 nmx6 nm wire.

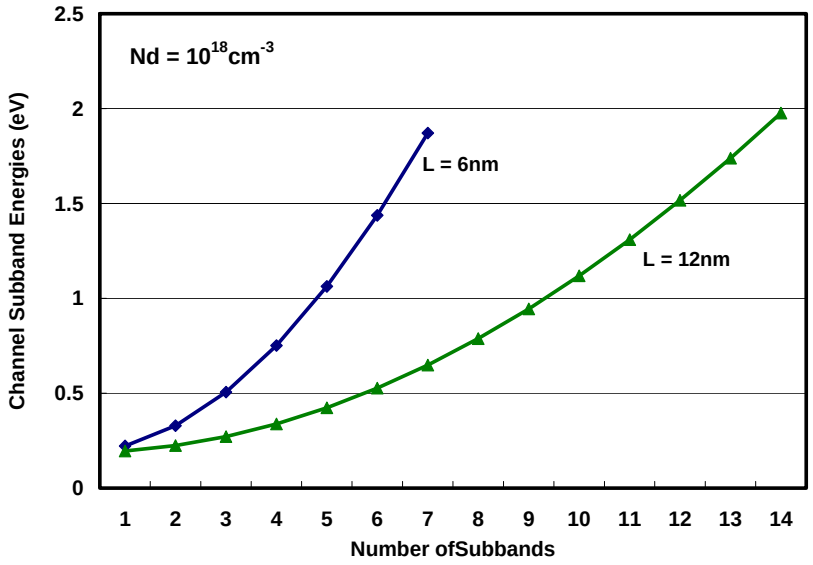

Figure 16. Comparison of subband energies for 6nm and 12nm silicon films

Effect of Electron-Phonon Scattering on the Power Factor of Silicon Films

Scattering of electrons with longitudinal optical phonons is modeled in the NEGF by treating scattering as an additional contact into which electrons can either scatter into or out of while ensuring that the net current

at that contact is zero. The procedure involved in calculating the current-voltage characteristics as well as the Seebeck coefficient and electrical conductivity is exactly the same as the ballistic case. Electrons interacting with optical phonons undergo both coherent and incoherent scattering. Coherent scattering results in a momentum redistribution while incoherent scattering results in energy loss or gain with the lattice. For the device dimensions considered in this thesis, the electrons undergo only elastic scattering as seen from figure 17 where the energy current per unit energy of the electron entering from the source and leaving through the drain is equal. The energy of the optical phonons with which the electrons scatter is 63meV. The material parameters and the value of the deformation potential used to obtain the transition rate S_o in equation 89 were obtained from [15]. The momentum redistribution however results in significant resistance to electron transport as seen

from figure 18 where there is a 45% decrease in the current of a 12nm film compared to its ballistic conductivity.

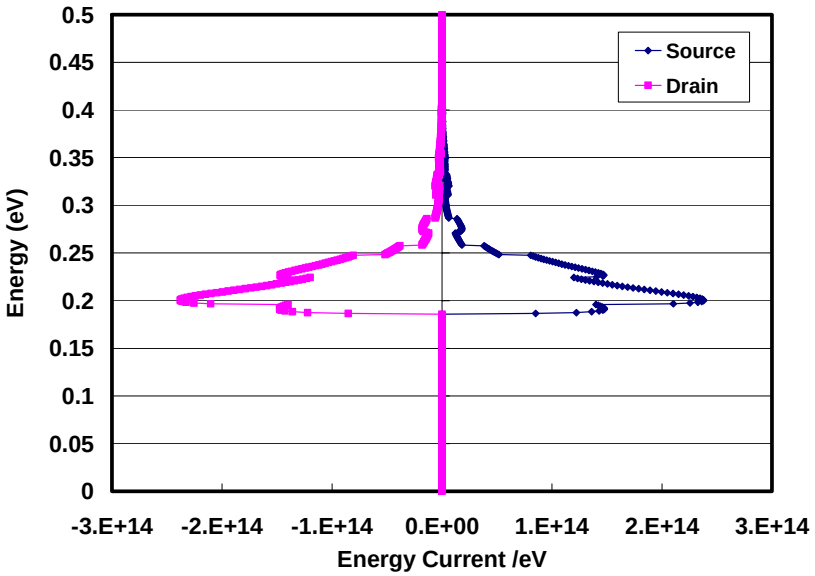

Figure 17. Comparison of the energy current with optical-phonon scattering, entering from the source and leaving through the drain for a 6nm film doped to $10^{18}cm^{-3}$.

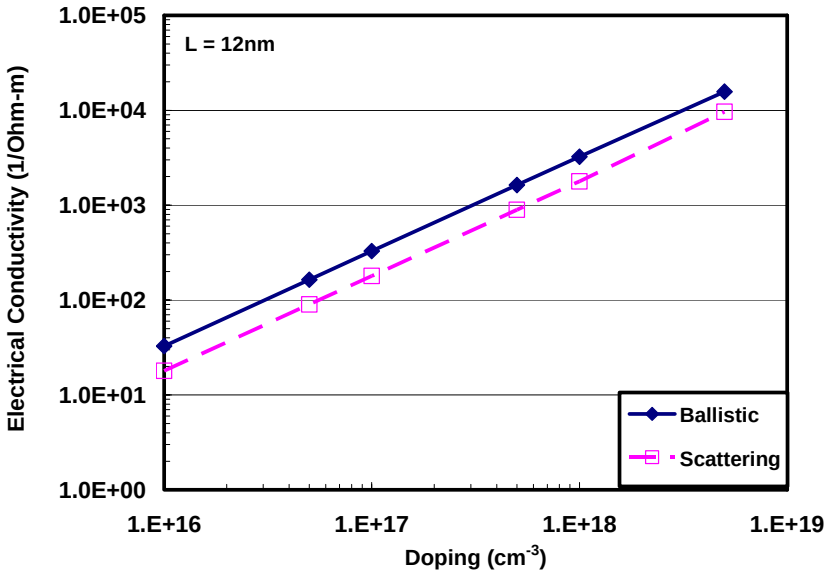

Figure 18. Decrease in the electrical conductivity of a 12nm silicon film due to scattering with optical phonons.

The decrease in conductivity dominates the power factor in the thermoelectric performance of silicon thin films as the Seebeck coefficient showed only a 20μV/K decrease with scattering. The power factor defined as $S^2\sigma$ is calculated and compared for a 6nm silicon film for both ballistic and scattering cases in figure 19. Despite the 6nm film exhibiting very low scattering of approximately 10% as seen in figure 10, for large doping the number of carriers available to scatter is higher leading to 20% decrease in the power factor for a doping of $10^{19}cm^{-3}$ and a further decrease of 45% for $5x10^{19}cm^{-3}$ doping demonstrating the importance of scattering even at such small length scales.

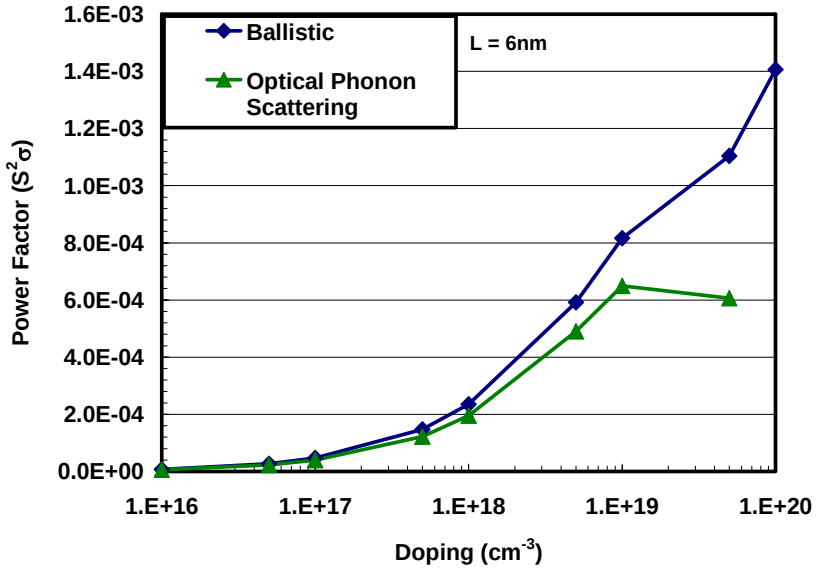

Figure 19. Power factor of a 6nm film with and without optical-phonon scattering predicted using the NEGF formalism.

In figure 20, the conductivity predictions from the NEGF model for 6 nm and 12nm silicon films were compared to the electrical conductivity predicted using the constant relaxation-time approximation (CRTA) model [2, 77] using the confined dispersion shown in equations 79 and 80, similar to the NEGF model. For electrical conductivity calculations, the CRTA model requires the value of mobility in the direction of transport. Because of the conflict in the electron mobility behavior with decreasing film thickness seen in the literature [91, 92, 93, 94], we use the bulk mobility value of silicon as a benchmark for calculating the electrical conductivity using the CRTA model. The conductivity predicted by the CRTA model for a single subband and the conductivity summed over two subband energies were found to be the same for a 6nm film while the NEGF model predicted a 95% difference between the two cases. The number of subbands chosen was based on the proximity of the subband energy levels to the conduction band from data in figure 16. Similarly, in the case of the 12 nm film, the conductivity predicted by the CRTA model for a single band differed from the conductivity summed over 6 subbands by 16% to 32% for a doping range of $10^{16}cm^{-3}$ to $10^{20}cm^{-3}$. Since the conductivity predictions of the CRTA model are directly proportional to the mobility, a value of $300cm^2/V\text{-}s$, corresponding to the mobility of a 20nm silicon film [91] instead of bulk mobility resulted in a 77% decrease in the conductivity predicted by the CRTA model. The results indicate that for a given mobility, the effect of confinement is captured in part by the CRTA model when confined dispersion

is used. The effect of electron confinement in the CRTA model predominantly comes from the value of mobility used which has to be determined experimentally or through additional quantum correction terms [10, 11 and12]. Figure 20 reiterates the fact that quantum effects are not inherent in Boltzmann models. While approximations to the Boltzmann model may work to a certain degree, they may not be able to cope with the advances being made in nanostructural devices. The NEGF method with its ability to couple scattering effects in a quantum model provides the key to this problem.

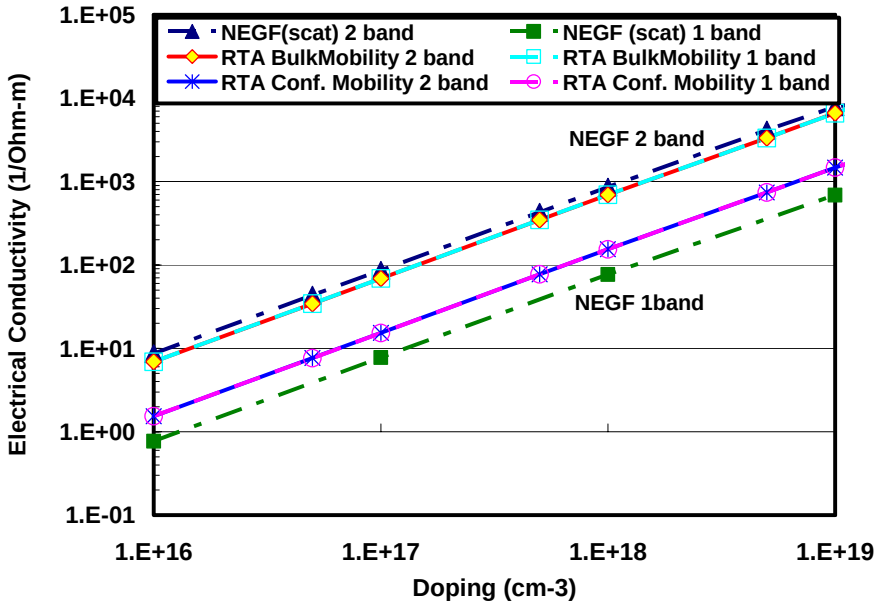

Figure 20. Comparison of the electrical conductivity predictions between the NEGF model and the CRTA model [2, 77] for a 6 nm silicon film

CHAPTER V

TRANSPORT IN SI/GE/SI QUANTUM WELL SUPERLATTICES

The quantum well superlattice studied in this research consists of a single quantum well formed by alternating layers of silicon, germanium and silicon thin films as shown in Figure 21. Electron confinement in the device occurs due to two reasons. 1) The very small thickness of the films gives rise to discretely spaced energy subbands in the cross-plane z-direction. 2) The difference in the conduction band edges of the different materials forming the layers of the superlattice set up potential barriers to electron flow thus causing additional confinement of the electrons in the well region. Electron transport in the device under an applied bias is modeled along the confined z direction and the current is calculated over the conduction band and 10 subbands. The Seebeck coefficient and electrical conductivity are calculated in a similar manner as the silicon films by varying the temperature of the drain relative to the source and averaging the results over the applied temperature gradient. The applied bias ranged from 0 to 0.05V.

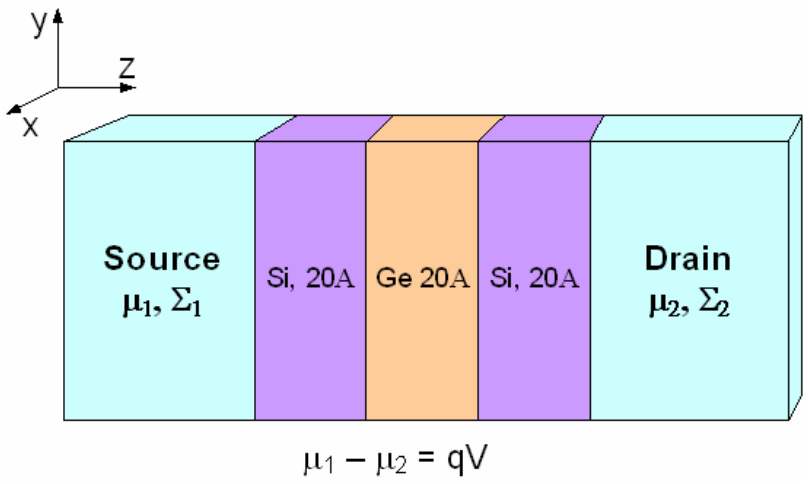

Figure 21. Schematic representation of a Si/Ge/Si quantum well superlattice modeled in the simulation

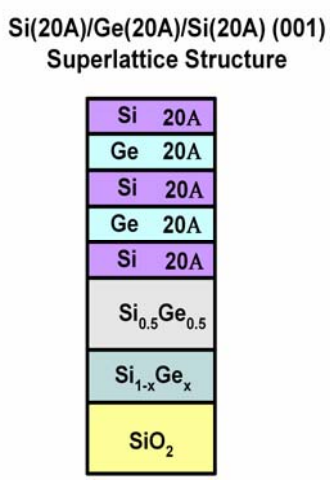

Figure 22. Schematic of a commercially grown Si/Ge/Si superlattice structure.

Effect of Substrate Strain

Superlattices are commonly grown on buffer layers consisting of either a fixed concentration of Si_xGe_{1-x} alloy or a graded Si_xGe_{1-x} layer on which alternate layers of silicon and germanium are epitaxially grown as shown in figure 22. When an interface is created between any two materials with mismatched lattice constants, strain develops at the interface as the two layers are stretched and compressed till the system reaches equilibrium where the strain energy is at its minimum [95]. For materials such as silicon that has a diamond structure, strain splits the 6 fold degenerate conduction bands in silicon into two fold and four fold degenerate bands with the energy of the two fold degenerate bands being lower than that of the four fold degenerate bands. This effect is due to the fact that the wave function of the conduction-band minima near the *X* point contains a significant contribution from excited *d*-orbitals [96]. This portion of the wave function is bonding in nature so its energy is reduced as atomic cores are brought closer together. Therefore, the conduction-band minimum in silicon is lowered in the presence of compressive strain. Conversely, tensile strain in silicon causes an increase in the energy of the conduction-band valleys that are oriented in the direction of the applied strain.

The effect of strain is demonstrated in the case where there is an interface between silicon and germanium. Silicon and germanium have lattice constants of 5.43 Å and 5.67 Å respectively. The interface between

(001) silicon and (001) germanium surfaces produces biaxial tensile strain in the plane of the silicon lattice due its smaller lattice constant. Accordingly, the silicon (001) layers will experience tensile biaxial strain in the plane of the interface raising the energies of the (100) and (010) valleys in k-space. The compressive stress generated in silicon along the [001] direction perpendicular to the plane of strain lowers the conduction band valley in the Δ direction in k-space. Similarly the germanium (001) atoms will experience compressive biaxial strain leading to a decrease in the energy of the (100) and (010) valleys while the energy of the (001) valley along the z-axis is increased due to tensile stress. Therefore, biaxial strain breaks the symmetry that originally exists due to splitting of the conduction band minima.

In general, the effective mass for motion along an axis is higher than the effective mass in the plane perpendicular to the axis. For example, in silicon, the effective mass for motion along the z axis or [001] direction is $0.91m_e$ while the effective mass along the [100] and [010] axis is $0.19m_e$ leading to higher mobility in the x-y plane. At room temperature, electrons lie predominantly in the valleys corresponding to the x and y axes. Under biaxial strain, the energy minima of the z-axis is lowered and electrons fall into the valley corresponding to the (001) valley which has lower effective mass in the x-y plane. This feature is exploited in MOSFETS where the mobility along the x-y plane is higher for biaxial strain in the (001) layers perpendicular to the z-axis. Since we are studying transport in the cross-plane direction of superlattices, electron transport along the [001] direction is modeled using an effective mass of $0.91m_e$.

During the fabrication of superlattice structures, the epitaxial growth of the various layers ensures that the final lattice constant is equal to that of the corresponding substrate. For example, if the substrate used is $Si_{0.5}Ge_{0.5}$ then the silicon and germanium layers are strained accordingly to match the lattice constant of $Si_{0.5}Ge_{0.5}$. In this case the lattice constant of $Si_{0.5}Ge_{0.5}$ is 5.54 Å which is greater than the lattice constant of silicon and lower than that of germanium. Accordingly, the conduction band minima in the silicon layers will be lowered while the energy in germanium will increase. Van de Walle [97] in 1989 developed a *model-solid* theory to calculate the change in the bandstructure of materials under biaxial strain. According to his research, the shift in the conduction band with respect to the average value is given by

$$\Delta E_c^{001} = \frac{2}{3}\Xi_u^{\Delta}\left(\varepsilon_{zz} - \varepsilon_{xx}\right) \quad (91)$$

The strain tensors ε_{zz} and ε_{xx} are obtained from the difference in the in-plane and cross-plane lattice constants. Ξ_u is the hydrostatic deformation potential for the conduction band. Using Van de Walle's model, the change in the conduction band edges for silicon and germanium due to substrate strain were calculated for Si_xGe_{1-x} substrates with varying concentrations of silicon and germanium. The resulting band diagrams depicting the splitting of the conduction band edge along the Δ valley in silicon and germanium due to Si(001) and $Si_{0.5}Ge_{0.5}$ respectively are shown in figure 23. The shift in the conduction band edges were incorporated into the NEGF model through the value of Ec in the Hamiltonian to obtain the current-voltage characteristics and the thermoelectric coefficients of strained Si/Ge/Si quantum well superlattice structures.

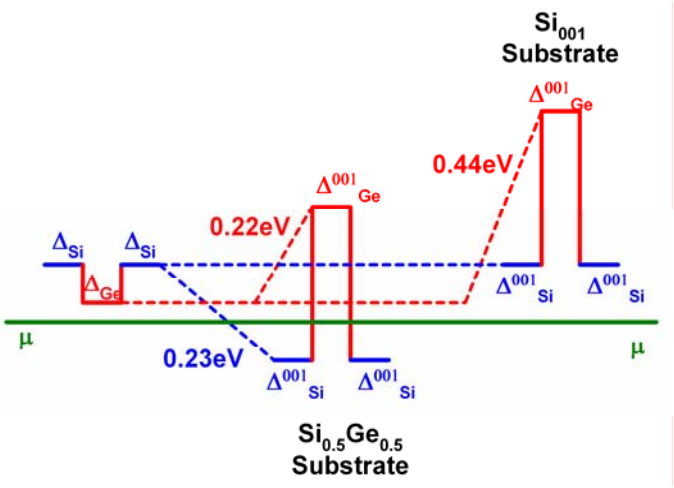

Figure 23. Change in bandstructure of silicon and germanium with strain for Si(001) and $Si_{0.5}Ge_{0.5}$ substrates

Thermoelectric Properties of Strained Si/Ge/Si Quantum Well Superlattices

Figure 24 shows the Seebeck coefficient of Si(2nm)/Ge(2nm)/Si(2nm) superlattice structure The Seebeck coefficient values of Si(001) substrate is significantly larger than the other substrates at low doping. The reason for this increase can be explained by looking at the band diagram of a Si(001) substrate vs. $Si_{0.5}Ge_{0.5}$

substrate for a particular doping. Figure 25 shows the band diagrams of the Si(2nm)/Ge(2nm)/Si(2nm) superlattice for a doping of $1x10^{18}cm^{-3}$ with respect to a reference Fermi level of 0.1eV.

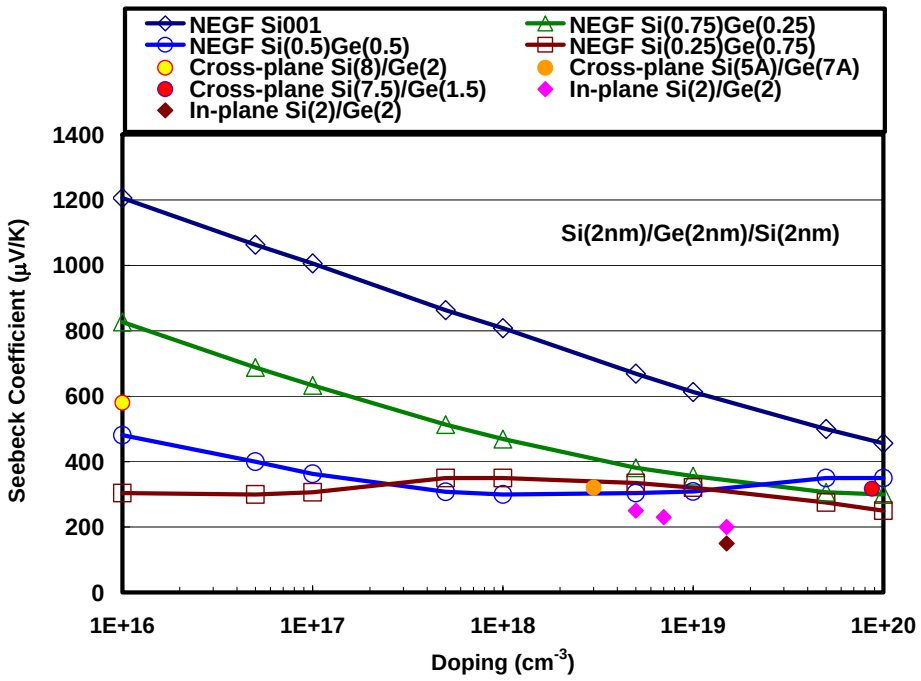

Figure 24. Seebeck coefficient vs. doping for Si/Ge/Si superlattice for various substrates compared with experimental measurements taken from [9, 98, 99, 100 and 101].

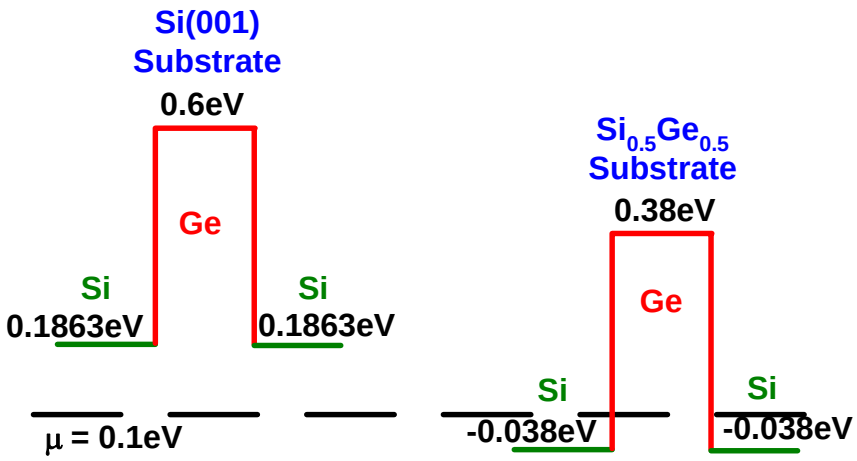

Figure 25. Band diagram of quantum well for a doping of $1x10^{18}cm^{-3}$ for Si(001) and $Si_{0.5}Ge_{0.5}$ substrates.

As seen in figure 23, the conduction band edge in silicon does not change for a Si(001) substrate. From figure 25 we can see that the 10^{18} doping ensures that the conduction band edge in silicon remains at 0.0863eV above the Fermi energy which is approximately equal to $3k_BT$. The germanium layer however experiences tensile strain along the [001] direction due to Poisson's stresses. As a result, the band splitting in germanium causes the germanium layer to form a significant barrier to the flow of electrons. When the temperature at the drain is increased, the electrons at the conduction band edge in silicon cannot easily diffuse nor drift through the superlattice due to the germanium barrier resulting in a large Seebeck voltage.

The conduction band in silicon for the $Si_{0.5}Ge_{0.5}$ substrate is below the Fermi level as silicon layer experiences compressive stresses along the z-axis causing the band edge along the [001] direction to be lower than the average value of Ec in silicon (refer figure 23). For thermoelectric purposes when the temperature at the superlattice drain is increased, the electrons at the conduction band edge in silicon cannot easily diffuse nor drift through the superlattice due to the large germanium barrier resulting in a large Seebeck voltage. In the case of a $Si_{0.5}Ge_{0.5}$ substrate, band splitting due to compressive stresses along the z-axis in the silicon layer shift its conduction band minima below the Fermi level. When the drain temperature is increased, electrons below the Fermi level gain energy and occupy the states immediately above the Fermi level on the drain side. The empty states below the Fermi level on the drain side attract electrons from the source that can tunnel through the germanium layer easily. The ability of electrons to tunnel through germanium means the electron diffusion due to temperature is easily balanced by electron drift at low voltages. Hence the Seebeck voltage developed is lower than that of the Si(001) substrate leading to lower Seebeck coefficients.

The oscillations in the Seebeck coefficient with doping for the $Si_{0.5}Ge_{0.5}$ and $Si_{0.25}Ge_{0.75}$ substrates can be explained by looking at the available density of states/eV distribution in the superlattice for the $Si_{0.5}Ge_{0.5}$ substrate shown in figure 26. It can be seen from figure 26a that for a few k_BT below the Fermi level, the density of states for the $10^{18}cm^{-3}$ doping case is approximately 12states/eV and is higher than that of the $5x10^{19}cm^{-3}$ doping case in figure 26b, which contains about 5 states/eV. When the drain temperature is raised, electrons from states below the Fermi level rise to states above it. However with the limited

availability of states below the Fermi level in the case of the $5x10^{19}cm^{-3}$ doping case, the probability of electrons tunneling from the source side of the silicon layer is lower in the case of the $5x10^{19}cm^{-3}$. As a result, more electrons can tunnel in the $10^{18}cm^{-3}$ doping case resulting in a Seebeck coefficient that is smaller by 17% compared to the $5x10^{19}cm^{-3}$ doping case. It is evident from the results in figures 24 and 25 that lower concentrations of silicon in the substrate alloy layer will result in greater strain in the silicon layer lowering its conduction band edge further below the Fermi level. The lower conduction band shifts the subbands closer to the Fermi level leading to Seebeck oscillations as seen from figure 24 where the $Si_{0.25}Ge_{0.75}$ substrate also displays oscillations in the Seebeck coefficient with doping. This effect is only possible where confinement creates discrete density of states.

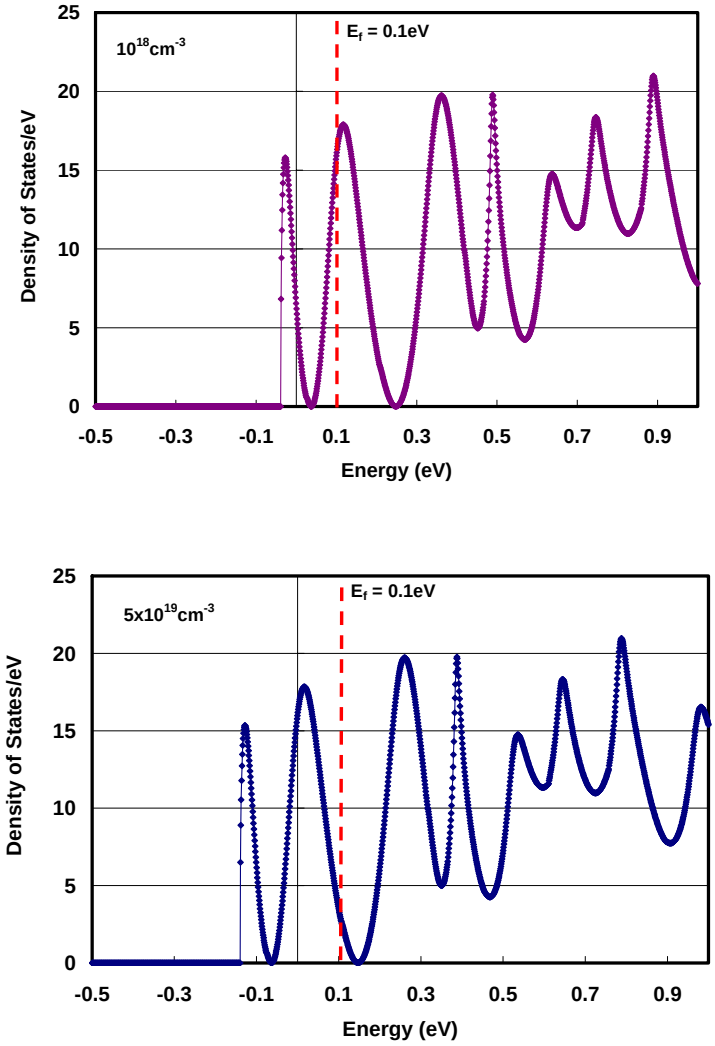

Figure 26. (a) Available Density of states vs. energy for $1x10^{18}cm^{-3}$ doping of the superlattice (b) Density of states vs. energy for $5x10^{18}cm^{-3}$ doping of superlattice. The red line in each case is the Fermi level

Experimental evidence of increase in Seebeck coefficient with doping was reported by Vashaee et.al. [102]. In this case the superlattice structure was made of 25 periods of InGaAs (5nm)/InAlAs(3nm) layers. The measured Seebeck coefficient was found to decrease with doping from $2x10^{18}cm^{-3}$ to $8x10^{18}cm^{-3}$ after which it almost doubles for a doping of $3x10^{19}cm^{-3}$. No sign change in the Seebeck coefficient was observed experimentally indicating that transport was due to electrons and not holes.

Figure 27 shows the electrical conductivity of the quantum well superlattice for various substrates as a function of doping. The conductivity for a given doping increases as the concentration of silicon in the substrate is reduced. The reason for this behavior is due to the fact that when the percentage of silicon in the substrate is reduced, the silicon layer is increasingly under tensile stress. As a result, the conduction band edge in silicon is lowered relative to the Fermi level. Even though the value of $\Delta Ec_{Si\text{-}Ge}$ does not change, the lowering of the silicon band edge with increase in the concentration of germanium in the substrate means the germanium layer will also get closer to the Fermi level opening more states for electron transport and hence better conductivity.

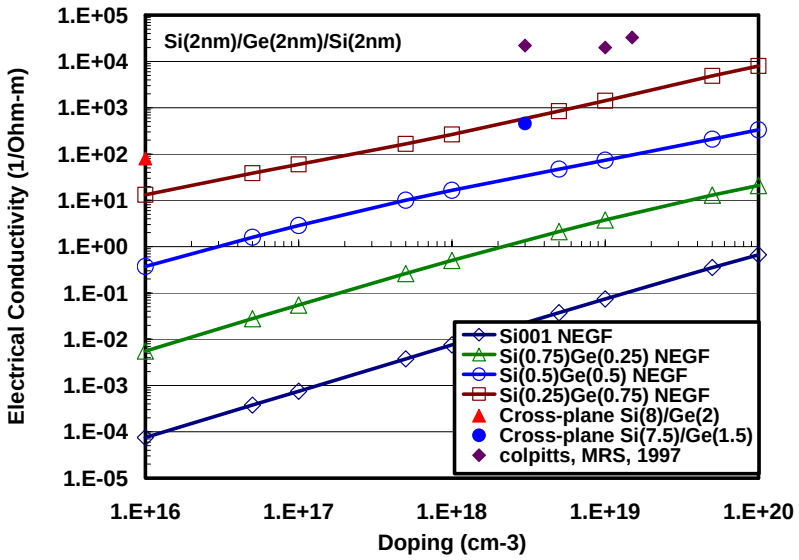

Figure 27. Electrical conductivity vs. doping for Si/Ge/Si superlattice for various substrates compared with measured values taken from [98, 99].

The dominance of the electrical conductivity on the power factor is evident from figure 28 where despite the very high Seebeck coefficients of the superlattice grown on Si(001) substrate, the superlattice grown on $Si_{0.25}Ge_{0.75}$ substrate has the best power factor values due to its higher electrical conductivity compared to other substrates.

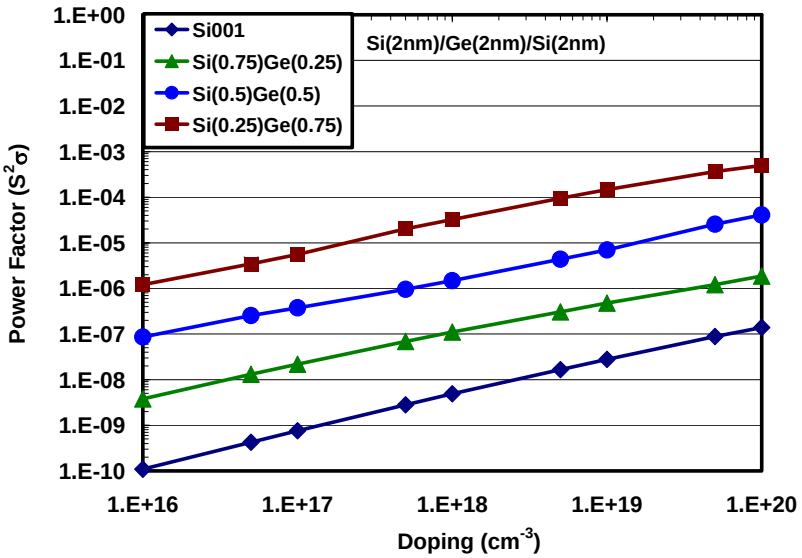

Figure 28. Power factor vs. doping of Si/Ge/Si superlattice for various substrates

The usefulness of the NEGF method as a tool for designing and optimization of quantum well structures for enhanced thermoelectric performance is demonstrated through figures 29 and 30 where the power factor of Si/Ge/Si superlattices grown on Si(010) substrate and $Si_{0.5}Ge_{0.5}$ substrate is compared for three different germanium barrier layer thicknesses. The first is a Si(2nm)/Ge(1nm)/Si(2nm) superlattice where electrons can easily tunnel through the germanium layer. The second is the Si(2nm)/Ge(2nm)/Si(2nm) where tunneling is more likely for the superlattice on $Si_{0.5}Ge_{0.5}$ substrate compared to the Si (001) substrate for low doping. The third is a Si(2nm)/Ge(4nm)/Si(2nm) superlattice where absolutely no tunneling is possible due to the very large germanium barrier layer.

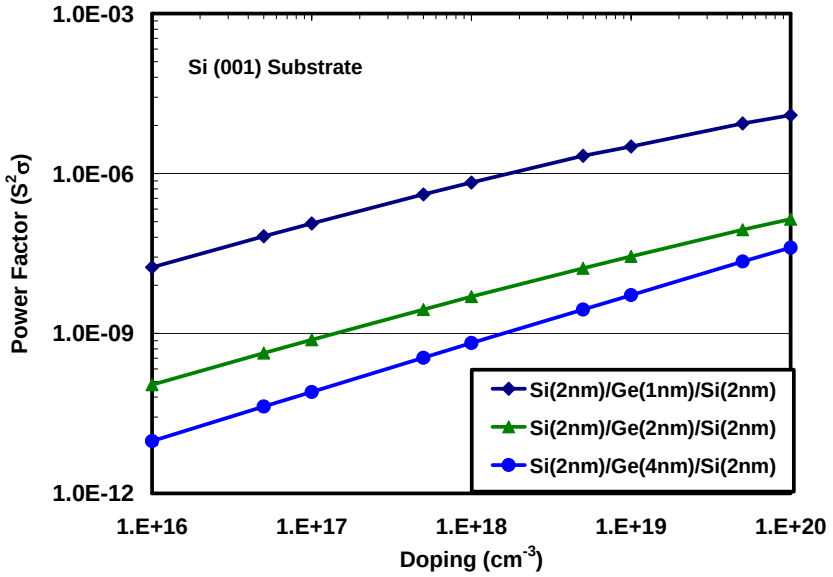

Figure 29. Power factor of Si/Ge/Si superlattices with Si (001) substrate for varying thickness of germanium layer

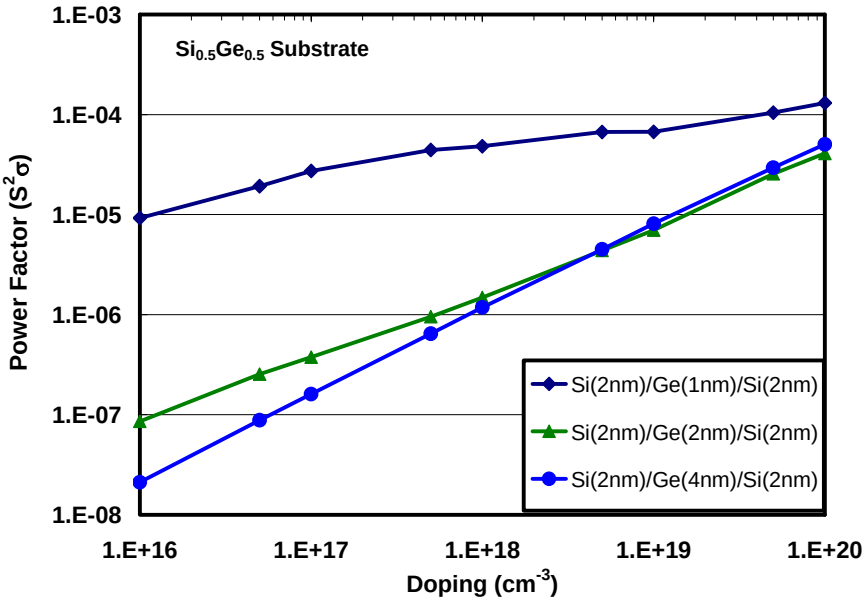

Figure 30. Power factor of Si/Ge/Si superlattices with $Si_{0.5}Ge_{0.5}$ substrate for varying thickness of the germanium layer

As expected the electrical conductivity dominates the power factor for all cases. The best power factor for both substrates is obtained for the Ge 1nm layer that allows electron tunneling through the superlattice resulting in high electrical conductivity. For higher doping, the Si(2nm)/Ge(2nm)/Si(2nm) superlattice has

almost the same power factor as the Si(2nm)/Ge(4nm)/Si(2nm) superlattice for $Si_{0.5}Ge_{0.5}$ substrate as seen in figure 30. The reason for this behavior can be understood from figure 31 where the subband energies for superlattices with Ge2nm and Ge4nm have been plotted for $Si_{0.5}Ge_{0.5}$ and Si(001) substrates for a doping of $10^{19}cm^{-3}$. For energy below the germanium barrier height, the subband energies in the superlattice occur in pairs. These levels originate from each of the silicon wells in the three layer Si/Ge/Si superlattice. Since the subband energies correspond to the eigen values of the superlattice Hamiltonian these subband energy levels are not the same as silicon films having the same thickness as the well region. The actual current contributed by each of these subbands is determined by the Green's function of the channel that takes into account the presence of the germanium barrier layer when calculating the channel density of states. As seen from figure 31, the conduction band edge for the germanium layer with $Si_{0.5}Ge_{0.5}$ substrate lies below the Fermi level compared to the Si (001) substrate. As a result, the first few subband energies for a superlattice on $Si_{0.5}Ge_{0.5}$ substrate lie closer to the Fermi level compared to the Si(001) substrate providing more states for electron transport. In addition, the 4nm germanium layer also has more subband energies available for transport within a given energy range. This is evident from figure 31 where between the energy range of -0.1eV to 0.5eV, the superlattice with Ge4nm layer on $Si_{0.5}Ge_{0.5}$ substrate has one additional subband compared to the a superlattice with Ge2nm layer on $Si_{0.5}Ge_{0.5}$ substrate.

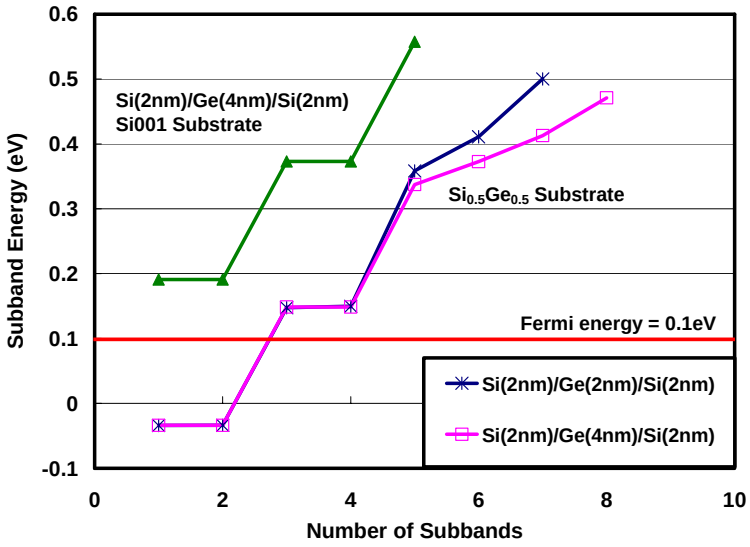

Figure 31. Comparison of subband energies of Si(2nm)/Ge2nm/Si(2nm) and Si(2nm)/Ge(4nm)/Si(2nm) superlattices on Si(001) and $Si_{0.5}Ge_{0.5}$ substrates.

The similar thermoelectric performance of the higher doped Ge2nm and Ge4nm superlattices on Si_xGe_{1-x} substrates can be taken advantage of during the fabrication of superlattices where interlayer diffusion between very thin layers can be avoided by using a thicker germanium layer to obtain the desired thermoelectric performance.

Effect of Electron-Phonon Scattering on the Power Factor of Si/Ge/Si Superlattices

Electron-optical phonon scattering was included in the NEGF to study the impact of scattering on the thermoelectric performance of strained superlattices shown in figure 32. The study was done for the two cases of Si(2nm)/Ge(1nm)/Si(2nm) superlattice on Si(001) and $Si_{0.5}Ge_{0.5}$ substrates since the superlattice with this thickness had produced the highest power factor distribution with doping of all the structures considered. Electron-phonon scattering caused the power factor of both superlattices to decrease due to decrease in the electrical conductivity. Since the subband energies of the superlattice on $Si_{0.5}Ge_{0.5}$ substrate lie closer to the Fermi level compared to the Si(001) substrate, the superlattice on $Si_{0.5}Ge_{0.5}$ substrate show greater decrease in the current with scattering. As a result, the average decrease in the power factor for the superlattice on $Si_{0.5}Ge_{0.5}$ substrate was 64% compared to the 43% decrease in the case of a Si(001) substrate. However, the overall power factor of the superlattices on $Si_{0.5}Ge_{0.5}$ substrate with scattering was still an order of magnitude greater than superlattices on the Si(001) substrate. The oscillations in the Seebeck coefficient in the case of the $Si_{0.5}Ge_{0.5}$ substrate were also present in the power factor distribution with doping. While increased doping is commonly associated with better conductivity and performance, the Seebeck oscillations point to an interesting result where the power factor for $5x10^{18}cm^{-3}$ doped superlattices is lower than the power factor of the lesser doped $1x10^{18}cm^{-3}$ superlattices.

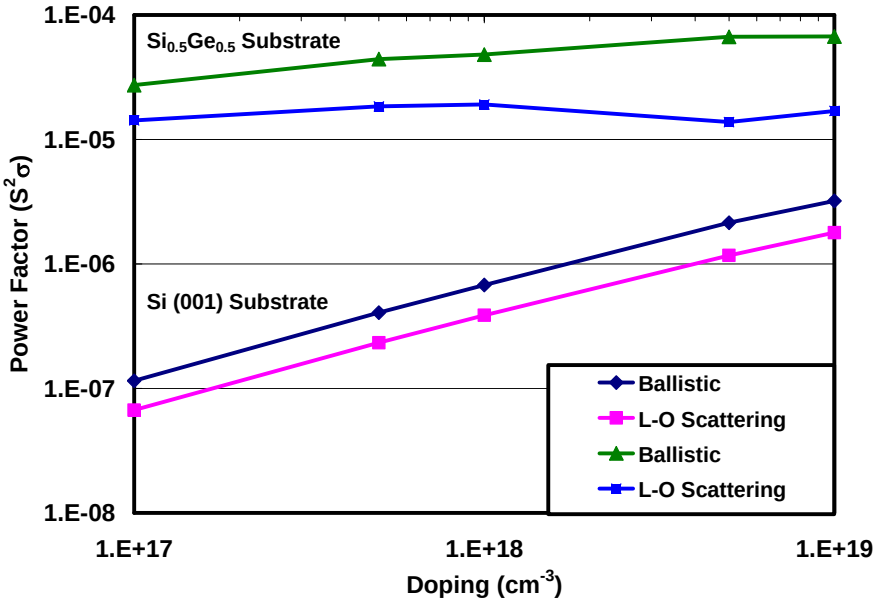

Figure 32. Comparison of thermoelectric performance with scattering for strained Si(2nm)/Ge(1nm)/Si(2nm) superlattices with $Si_{0.5}Ge_{0.5}$ and Si(001) substrates.

CHAPTER VII

CONCLUSIONS

Reliance on Boltzmann-based models has produced a culture of "smaller is better" research, where the reduction in size is expected to produce limitless increase in performance. Experimental observations especially in the case of thermoelectric performance of nanoscale devices have not exhibited this behavior. The motivation for this research stemmed out of a need to understand the disparity in theoretical predictions and experimental observations.

Transport models based on Boltzmann and Fermi-Dirac statistics coupled in semi-classical transport have been very effective in identifying the pertinent physical parameters responsible for thermoelectric performance in bulk materials. The inclusion of various scattering mechanisms through the relaxation time approach allow us to isolate and understand carrier scattering mechanisms that dominate thermoelectric performance for a particular temperature range. While the semi-classical models work well in predicting the performance of materials in the bulk regime, wave effects that cannot be captured naturally in particle-based models begin to dominate in nanostructured materials. Reduced dimensionality results in phonon confinement and formation of phonon bandgaps as well as tunneling and diffraction of electrons that are characteristic of wave behavior. Furthermore, alteration of the dispersion relations of electrons and phonons at nanoscales affects the way these carriers interact with each other. Figure 10 demonstrates that at length scales near the room temperature de Broglie wavelength of electrons, phonons do not affect electron transport significantly. This means that in devices at these length scales, carrier distribution is no longer in equilibrium. Another important effect seen from figure 10 is the effect of electron confinement. Decreased length scales lead to energy discretization limiting the number of energy states available to transport electrons at the nanoscale leading to a decrease in current with shrinking device size for a constant field.

For materials at reduced scales, the governing physics changes enough that new models are required. A quantum transport model that can successfully couple wave effects and scattering effects to predict thermoelectric performance is introduced through the non-equilibrium Green's function method. Using an effective mass Hamiltonian, current flow from the contacts is modeled as a modification of the channel density of states through self energy terms in the Hamiltonian. In addition, the NEGF method does not require a statistical distribution of carriers. This allows for the modeling of highly non-equilibrium transport as well as the inclusion of rigorous scattering. The ability of the NEGF method to model quantum effects purely based on first principles is evident from figure 20 where the conductivity predictions of the NEGF and the semi-classical CRTA model are compared. While the NEGF model does not rely on any external parameters other than the electron effective mass, the reliance of the CRTA model on external electron mobility data for conductivity predictions demonstrates the empirical nature of the semi-classical Boltzmann model. In addition to successfully coupling quantum and scattering effects, the NEGF method allows us to seamlessly include various parameters that affect thermoelectric performance such as bandgaps, doping, and effective mass.

The NEGF method is used to study the effect of electron confinement on silicon nanofilms and wires. Electron confinement results in almost a factor of 4 decrease in the electrical conductivity of the 6nm silicon film compared to the 12nm film. Increase in the amount of confinement also leads to a 33% decrease in the conductivity of a 6nm x 6nm wire compared to the 6nm film. Electron-optical phonon scattering was included in the NEGF using the concept of Buttiker probes where scattering is treated as another contact. Scattering with optical phonons was found to have a greater effect on the 12nm film where the current decreased by 45% of its ballistic value.

Thermoelectric performance of quantum well superlattices is studied using the NEGF model with the inclusion of substrate strain and optical phonon scattering. The power factor of a single period superlattice is compared for various substrates. It was found that a substrate rich in germanium would lower the energy of the conduction band valley in silicon to providing more states around the Fermi energy for electron transport. Such substrates also produce oscillations in the Seebeck coefficient that are attributed to the shift

in subband energies around the conduction band due to doping. These effects cannot be captured in semi-classical models without introducing some form of quantum corrections.

The power factor of the superlattices was found to be dominated by the electrical conductivity despite the very high Seebeck coefficients of the Si(001) substrates that were poor electrical conductors. The thermoelectric performance of superlattices was also studied as a function of the germanium barrier thickness. Overall, despite a 64% decrease in conductivity due to electron-phonon scattering, the best thermoelectric performance was obtained for superlattices with germanium rich substrates having barriers that allowed tunneling as in the case of a Si(2nm)/Ge(1nm)/Si(2nm) structure on $Si_{0.5}Ge_{0.5}$ substrate. The Seebeck oscillations produced by germanium rich substrates could be exploited to design structures with high power factors for low doping. The coupled thermoelectric solution combined with quantum and scattering effects in superlattices demonstrates the capability of the NEGF method as a platform to design structures with enhanced figure of merit.

The NEGF model suggests that optimization of devices is possible. Although this places theoretical upper limits on performance, there is no indication that these theoretical limits have been reached and continued research is warranted. While quantum effects are inherent in the NEGF model, the effect of various scattering mechanisms such as electron-impurity scattering and intersubband electron-phonon scattering must be further explored to fully gauge the performance of nanoscale structures. This research started as an attempt to explain the discrepancy between theoretical predictions and experimental data of nanoscale devices. Not only have we identified the pertinent physics that explain the discrepancy, but we have also developed a framework for further studies on performance of highly scaled thermoelectric devices. Now device designers have a tool with appropriate predictive power to guide the continued search for high efficiency materials.

APPENDIX A

MATLAB PROGRAM FOR I-V CHARACTERISTICS OF SILICON FILMS

```
%% Program to calculate the current density vs. voltage characteristics for a silicon film. Ballistic transport
is assumed. Current is summed over the conduction band and 10 subbands %%
clear all, close all
%%%% Constants (all MKS, except energy which is in eV) %%%%
hbar = 1.06e-34;                % Reduced Planck's constant, Units of Joule-sec
q = 1.6e-19;                    % Charge of an electron in Coulombs
Io = 2*(q^2)/(2*pi*hbar);   % Quantized conductance term, units of Amp/eV
%%%% Specifying Material Inputs %%%%
epsil0 = 8.85e-12;    % Permittivity of free space, Units of Farad/m = Coulomb/Volt-m
epsilr = 11.7;          %  Relative permittivity for Silicon
me = 9.31e-31;        % Electron mass in Kg
m = 0.91*me;          % Electron effective mass in silicon along 001 direction, units of Kg
mu = 0.1;               % Fermi energy
Ec = 0.1863;          % Conduction band edge in silicon for doping level of 10^18/cm^3
%%%% Specifying temperature of source and drain %%%%
kT = 0.0259;          % General room temperature in eV (Boltzmann constant k * Temperature T)
kT1 = 0.0259;         % Source temperature at 300K
kT2 = 0.0259;         % Drain temperature at 300K
%%%% Grid Inputs %%%%
a = 2e-10;                      % Distance between successive nodes
Np = 31;                        % Number of nodes in Silicon
XX = a*(Np-1);                % Length of silicon layer
Len = linspace(0,XX,Np)';    % Stores length in a column vector
```

```
t = (hbar^2)/(2*m*(a^2)*q);  % Inter-unit cell coupling energy for silicon, units of eV
%%% Calculating channel potential constants %%%%%
Uo = q./(2*pi*epsilr*epsil0*a);   % Units of eV
Uo = Uo.*log(2);
U = 0;              % Setting initial potential in channel to be zero
%%%%%%%%% Hamiltonian Matrix, Units of eV %%%%%%%%%%%
H=(((2*t)+Ec)*diag(ones(1,Np)))-(t*diag(ones(1,Np-1),1))-(t*diag(ones(1,Np-1),-1));
[VH DH] = eig(H);    % Calculates eigen vectors and energy eigen values of Hamiltonian
DH = diag(DH);       % Stores subband energies (eigen values) of superlattice in a column vector
%%%%%%%%%%% Defining energy range of incoming electrons %%%%%%%%%%%
NE = 1201;               % Number of energy steps
E=linspace(0,1,NE);    % Specifying incoming electron range
dE=E(2)-E(1)             % Difference between each energy step
zplus=i*1e-12;           % Incremental term for energy for broadening during coupling
Eng = E';                % Stores energy steps in a column vector
No1 = (m*kT1*q)/(2*pi*(hbar^2));   % Constant used in Fermi function (source) (1/m^2)
No2 = (m*kT2*q)/(2*pi*(hbar^2));   % Constant used in Fermi function (drain) (1/m^2)
%%%% Specifying applied drain bias %%%%%
NV = 201;                    % Number of voltage steps
VV = linspace(0,0.1,NV);    % Setting voltage range from 0V to 0.1V
Vol = VV';                   % Stores voltage steps in a column vector
%%%%%% START OF MAIN CURRENT-VOLTAGE CALCULATIONS %%%%%%
for nsb = 1:11   % Number of bands considered = Conduction band + 10 subbands
    if nsb == 1
      Ds = Ec;   % For first iteration, energy corresponds to conduction band edge
   else
      Ds = DH(nsb-1);   % Additional iterations over subbands whose value is obtained from line 52
   end
```

```
No = 0;    % For each subband, setting initial electron density in channel to be zero
Sig1 = zeros(Np,Np); Sig2 = zeros(Np,Np);  % Initial values for self energy matrices
%%%%%%%%%%%%%%%%%%%%%%%%%%%%%%%%%%%%%%%%%%%%%%%%%%%%%%%%%%%%%%%%%%%%%%%%%%%%%%%%
for b = 1:NV  % Start of voltage loop
    V = VV(b);     % Voltage input for each step
    chg = 1;       % Initial guess for potential change
    while chg > 1e-6  % Checks potential change
        Rh = 0;     % Initial electron density along length of channel
        for k = 1:NE   % Starting energy loop for incoming electron energy
        %%% Calculating Fermi functions of electrons entering through Silicon Source and Drain
%%%
        f1 = No1*log(1+exp((-(E(k)-mu))/kT1));      % 2D source Fermi function. Units of 1/m^2
        f2 = No2*log(1+exp((-(E(k)-mu + V))/kT2));  % 2D drain Fermi function. Units of 1/m^2
        %%%%%%%%%%%%%%%%%%%%%%%%%%%%%%%%%%%%%%%%%%%%%%%%%%%%%%%%%%%%%%%%%%%%%%%%%%%%%%%%
        ka1 = acos(1 - ((E(k) + zplus - Ds)/(2*t )));      % Wave vector of broadened waves at source
        Sig1(1,1) = -t*exp(i*ka1);                         % Self energy of source  (eV)
        Gam1 = i*(Sig1 - Sig1');                           % Source broadening matrix (eV)
        SigIn1 = Gam1*f1;                                  % Inscattering term for source (eV)

        ka2 = acos(1 - ((E(k) + zplus - Ds + V)/(2*t)));   % Wave vector of broadened waves at drain
        Sig2(Np,Np) = -t*exp(i*ka2);                       % Self energy of drain (eV)
        Gam2 = i*(Sig2 - Sig2');                           % Drain broadening matrix (eV)
        SigIn2 = Gam2*f2;                                  % Inscattering term for drain (eV)

        G = inv(((E(k) + zplus)*eye(Np)) -H -diag(U) -Sig1 -Sig2);   % Green's function  (1/eV)
        A = i*(G - G');                                    % Channel density of states matrix (1/eV)
        Gn = G*(SigIn1+SigIn2)*G';       % Electron density matrix in channel (1/eV-m^2)
```

```
Rh = Rh + (dE/(2*pi))*Gn;          % Calculating electron density in the channel  (1/m^2)
T = Gam1*G*Gam2*G';                % Transmission function (no units, number)
IT(k) = real(trace(T*(f1-f2)));    % Transmission current for each energy step  (number/m^2)
I1(k) = real(trace(SigIn1*A) - trace(Gam1*Gn));  % Source current for each energy step
                                                 (Number/m^2)
I2(k) = -real(trace(SigIn2*A) - trace(Gam2*Gn));  % Drain current for each energy step
                                                  (Number/m^2)
end     % End of energy loop
%%%%%%%%%% Self consistent potential calculation %%%%%%%%%%
N = real(diag(Rh));       % Stores diagonal elements (along length of channel) of density matrix,
Units                                of 1/m^2
Unew = Uo.*(N-No)*(a^2);  % Calculates new channel potential from change in electron density
(eV)
dU = Unew-U;              % Change in channel potential due to new electron density
chg = max(abs(dU))
U = U + 0.2*dU;           % Updating channel potential with respect to old potential
if V == 0
   No = N;, chg = 0;
end
Rho = N/a;   % Normalized electron density per unit cell (1/m3)
end   % End of potential while loop each voltage step
Den(:,b) = Rho;    % Stores electron density in channel for each voltage for the present subband
Pot(:,b) = U;      % Stores potential in channel for each voltage for the present subband
IE1(:,b) = I1';    % Current density per unit energy at source for each voltage
IE2(:,b) = I2';    % Current density per unit energy at drain for each voltage
Is(b) = dE*Io*sum(I1);   % Net source current density summed over all energies for each voltage step
Isc = Is';
```

```
        Id(b) = dE*Io*sum(I2);   % Net drain current density summed over all energies for each voltage step
        Idr = Id';
         I(b) = dE*Io*sum(IT);    % Net transmission current summed over all energies for each voltage step
         Itr = I'
    end   % End of each voltage step loop
    Isb(:,nsb) = Itr;   % Transmission current for each subband
    Isbs(:,nsb) = Isc;  % Source current for each subband
    Isbd(:,nsb) = Idr;  % Drain current for each subband
end  % End of subband loop
II = sum(Isb,2)   % Sum of current from all subbands for each voltage step
hold on
dlmwrite('Len.dat',Len,',');     % Stores length of the channel
dlmwrite('Vol.dat',Vol,',');      % Stores applied voltage range with incremental steps
dlmwrite('Eng.dat',Eng,',');    % Stores electron energy range with incremental steps
dlmwrite('Isb.dat',Isb,'\t');      % Stores transmission current for each subband for each voltage step
dlmwrite('Isbs.dat',Isbs,'\t');   % Stores source current for each subband for each voltage step
dlmwrite('Isbd.dat',Isbd,'\t');   % Stores drain current for each subband for each voltage step
dlmwrite('II.dat',II,',');            % Stores sum of currents from all subbands for each voltage step
```

APPENDIX B

MATLAB PROGRAM FOR I-V CHARACTERISTICS OF SILICON WIRES

%% Program to calculate current density vs. voltage characteristics for a silicon wire. Confined dimensions are along the Lx and Ly directions. The Lz direction has infinite length. Ballistic transport along Lx is assumed. The calculated current is summed over the conduction band and 10 subbands.

```
clear all, close all
%%%%% Constants (all MKS, except energy which is in eV) %%%%%
hbar=1.06e-34;                % Reduced Planck's constant, Units of Joule-sec
q = 1.6e-19;                  % Charge of an electron in Coulombs
Io = 2*(q^2)/(2*pi*hbar);     % Quantized conductance term, units of Amp/eV
%%%%%%%%% Specifying Material Inputs %%%%%%%%%%%
epsil0 = 8.85e-12;       % Permittivity of free space, Units of Farad/m = Coulomb/Volt-m
epsilr = 11.7;           % Relative permittivity for Silicon
me = 9.31e-31;           % Electron mass in Kg
m = 0.91*me;             % Electron effective mass in silicon along 001 direction, units of Kg
mu = 0.1;                % Fermi energy
Ec = 0.1863;             % Conduction band edge in silicon for doping level of 10^18/cm^3
%%%%%%% Specifying temperature of source and drain %%%%%%%%
kT = 0.0259;             % General room temperature in eV (Boltzmann constant k * Temperature T)
kT1 = 0.0259;            % Source temperature at 300K
kT2 = 0.0259;            % Drain temperature at 300K
%%%%%%%%%% Grid Inputs %%%%%%%%%%%
a = 3e-10;                    % Distance between successive nodes
Nx = 21;                      % Number of nodes in Silicon along the Lx direction
Ny = 21;                      % Number of nodes in Silicon along the Ly direction
```

```
Np = Nx*Ny;                 % Total number of nodes for the square grid
XX = a*(Nx-1);              % Length of Lx direction
YY = a*(Ny-1);              % Length of Ly direction
Lx = linspace(0,XX,Nx)';    % Stores length in a column vector
Ly = linspace(0,YY,Ny)';    % Stores length in a column vector
%%%%%%%%%%%%%%%%%%%%%%%%%%%%%%%%%%%%%%%%%%%%%%%%%%%%%%%%%%%%%%%%%%%%%%%%%%%%%%%
t = (hbar^2)/(2*m*(a^2)*q);  % Inter-unit cell coupling energy for silicon, units of eV
%%%%%%%%% Calculating channel potential constants %%%%%%%%%%%%
Uo = q./(2*pi*epsilr*epsil0*a);   % Units of eV
Uo = Uo.*log(2);
U = 0;                          % Setting initial potential in channel to be zero
%%%%%%%%%%%% Hamiltonian Matrix, Units of eV %%%%%% %%%%
   H = zeros(Np,Np);
   for n = 1:Np
      H(n,n) = Ec + 4*t;     %% Specifies main diagonal terms
   end
   j = 1;
   for r = 1:Ny;              %% For each row of nodes along Ly
      for n = 1:(Nx-1)        %% Specifies x-axis off-diagonal terms for each node along Lx
         H(j,j+1) = -t;
         H(j+1,j) = -t;
         j = j+1;
      end
      j = j+1;                %% Jumps to the next row of nodes along Ly
   end
   j = Nx+1;                  %% For each node point counting from 1 along Lx
   for r = 1:(Np-Nx)          %% Specifies Y-axis off-diagonal terms
      H(r,j) = -t;
```

```
    H(j,r) = -t;

    j = j+1;

  end

%%%%%%%%%%%%%%%%%%%%%%%%%%%%%%%%%%%%%%%%%%

[VH DH] = eig(H);          % Calculates eigen vectors and energy eigen values of Hamiltonian

DH = diag(DH);             % Stores subband energies (eigen values) of superlattice in a column vector

%%%%%%%%%%%% Defining energy range of incoming electrons %%%%%%%%%%%%

NE = 601;                  % Number of energy steps

E=linspace(0,1,NE);        % Specifying incoming electron range

dE=E(2)-E(1)               % Difference between each energy step

zplus=i*1e-12;             % Incremental term for energy for broadening during coupling

Eng = E';                  % Stores energy steps in a column vector


N1 = ((hbar^2)/(2*m*kT1*q));     % Constant used in Fermi function (source) Units of (m^2)

C1 = (1/(4*pi))*sqrt(1/N1);      % Constant used in Fermi function (source) Units of 1/m

N2 = ((hbar^2)/(2*m*kT2*q));     % Constant used in Fermi function (drain)  Units of (m^2)

C2 = (1/(4*pi))*sqrt(1/N2);      % Constant used in Fermi function (drain)  Units of 1/m

%%%%%%%%%%%% Specifying applied drain bias %%%%%%%%%%%%

NV = 31;                         % Number of voltage steps

VV = linspace(0,0.03,NV);        % Setting voltage range from 0V to 0.03V

Vol = VV';                       % Stores voltage steps in a column vector

%%%%%%%%%%%% START OF MAIN CURRENT-VOLTAGE CALCULATIONS %%%% %%%%%

for nsb = 1:11   % Number of bands considered = Conduction band + 10 subbands

   if nsb == 1

     Ds = Ec;             % For first iteration, energy corresponds to conduction band edge

  else

     Ds = DH(nsb-1);   % Additional iterations over subbands whose value is obtained from line 52

  end
```

```
No = 0;                    % For each subband, setting initial electron density in channel to be zero
Sig1 = zeros(Np,Np); Sig2 = zeros(Np,Np);  % Initial values for self energy matrices
for b = 1:NV  % Start of voltage loop
    V = VV(b);     % Voltage input for each step
    chg = 1;       % Initial guess for potential change
    while chg > 1e-6  % Checks potential change
          Rh = 0;     % Initial electron density along length of channel
          for k = 1:NE   % Starting energy loop for incoming electron energy
           % Calculating Fermi functions of electrons entering through Silicon Source and Drain %
          x = -(E(k) - mu)/kT1;
          X1(k) = x;
           if x < 2
              f1 = C1*Fermi1(x);      % 1D Source Fermi function. Units of 1/m
          else
              f1 = C1*Fermi2(x);      % 1D Source Fermi function. Units of 1/m
           end
           ferm1(k,b) = f1;           % Stores fermi function values for each energy
           x = -(E(k) - mu + V)/kT2;
            X2(k) = x;
            if x < 2
               f2 = C2*Fermi1(x);         % 1D Drain fermi function. Units of 1/m
            else
               f2 = C2*Fermi2(x);         % 1D Drain fermi function. Units of 1/m
            end
            ferm2(k,b) = f2;          % Stores fermi function values for each energy
    %%%%%%%%%%%%%%%%%%%%%%%%%%%%%%%%%%%%%%%%%%%%%%%%%%%%%%%%%
     ka1 = acos(1 - ((E(k) + zplus - Ec - Ds)/(2*t)));      % Wave vector of broadened waves at source
     j = 1;
```

```
for n = 1:Ny
    Sig1(j,j) = -t*exp(i*ka1);                  % Self energy of source  (eV)
    j = j + Nx;
end
Gam1 = i*(Sig1 - Sig1');                        % Source broadening matrix (eV)

ka2 = acos(1 - ((E(k) + zplus - Ec - Ds + V)/(2*t)));  % Wave vector of broadened waves at source
j = Nx;
for n = 1:Ny
    Sig2(j,j) = -t*exp(i*ka2);                  % Self energy of drain  (eV)
    j = j + Nx;
end
Gam2 = i*(Sig2 - Sig2');                        % Drain broadening matrix (eV)
G = inv(((E(k) + zplus)*eye(Np)) -H -diag(U) -Sig1 -Sig2);   % Green's function  (1/eV)
A = i*(G - G');                                 % Channel density of states matrix  (1/eV)

SigIn1 = Gam1*f1;              % Inscattering term for source Units of eV/m
SigIn2 = Gam2*f2;              % Inscattering term for drain Units of eV/m
SigIn = SigIn1 + SigIn2;

Gn = G*SigIn*G';               % Electron density matrix in channel (1/eV-m)
Rh = Rh + (dE/(2*pi))*(Gn);    % Calculating electron density in the channel (1/m)

T = Gam1*G*Gam2*G';            % Transmission function (no units, number)
IT(k) = real(trace(T*(f1-f2)));   % Transmission current for each energy step (number/m2)

I1(k) = real(trace(SigIn1*A) - trace(Gam1*Gn));    % Source current for each energy step
(Number/m)
```

```
        I2(k) = -real(trace(SigIn2*A) - trace(Gam2*Gn));   % Drain current for each energy step
(Number/m)
      end     % End of energy loop
      %%%%% Self consistent potential calculation %%%%%
      N = real(diag(Rh));          % Stores diagonal elements (along length of channel) of density matrix
(1/m)
      Unew = Uo.*(N-No)*a;   % Channel potential (eV)
      dU = Unew-U;                % Change in channel potential due to new electron density
      chg = max(abs(dU))
      U = U + 0.2*dU;             % Updating channel potential with respect to old potential
      if V ==0
         No = N; chg = 0;
      end
      Rho = N/(a*a);                % Normalized electron density per unit cell (1/m3)
    end      % End of potential while loop

  Den(:,b) = Rho;    % Stores electron density in channel for each voltage for the present subband
  Pot(:,b) = U;      % Stores potential in channel for each voltage for the present subband
  IE1(:,b) = I1';    % Current density per unit energy at source for each voltage
  IE2(:,b) = I2';    % Current density per unit energy at drain for each voltage
  Is(b) = dE*Io*sum(I1);   % Net source current density summed over all energies for each voltage step
  Isc = Is';
  Id(b) = dE*Io*sum(I2);   % Net drain current density summed over all energies for each voltage step
  Idr = Id';
  I(b) = dE*Io*sum(IT);    % Net transmission current summed over all energies for each voltage step
  Itr = I'
end     % End of each voltage step loop
Isb(:,nsb) = Itr;   % Transmission current for each subband
```

```
Isbs(:,nsb) = Isc;  % Source current for each subband

Isbd(:,nsb) = Idr;  % Drain current for each subband

end   %%% End of subband loop

II = sum(Isb,2)   % Sum of current from all subbands for each voltage step

hold on

dlmwrite('Len.dat',Len,',');   % Stores length of the channel

dlmwrite('Vol.dat',Vol,',');   % Stores applied voltage range with incremental steps

dlmwrite('Eng.dat',Eng,',');   % Stores electron energy range with incremental steps

dlmwrite('Isb.dat',Isb,'\t');      % Stores transmission current for each subband for each voltage step

dlmwrite('Isbs.dat',Isbs,'\t');   % Stores source current for each subband for each voltage step

dlmwrite('Isbd.dat',Isbd,'\t');   % Stores drain current for each subband for each voltage step

dlmwrite('II.dat',II,',');            % Stores sum of currents from all subbands for each voltage step
```

APPENDIX C

MATLAB PROGRAM FOR I-V CHARACTERISTICS OF STRAINED SI/GE/SI SUPERLATTICES

```
%%% Program to calculate current density vs. voltage characteristics for a strained Si/Ge/Si superlattice.
Ballistic transport is assumed. Current is summed over conduction band and 10 subbands. %%%
clear all, close all
%%%%% Constants (all MKS, except energy which is in eV) %%%%%
hbar=1.06e-34;                  % Reduced Plancks constant, Units of Joule-sec
q = 1.6e-19;                    % Charge of an electron in Coulombs
Io = 2*(q^2)/(2*pi*hbar);       % Quantized conductance term, units of Amp/eV
%% Specifying Material Inputs %%
epsil0 = 8.85e-12;              % Permittivity of free space, Units of Farad/m = Coulomb/Volt-m
epsilrS = 11.7;                 % Relative permittivity for Silicon
epsilrG = 16;                   % Relative permittivity for Germanium
epsilrJ = 0.5*(epsilrS + epsilrG);  % Relative permittivity of the Si/Ge junction
me = 9.31e-31;          % Electron mass in Kg
ms = 0.91*me;           % Silicon effective mass along 001 direction
mg = 0.95*me;           % Germanium effective mass along 001 direction
mu = 0.1;               % Fermi energy
Ecs = 0.1863;           % Conduction band edge in silicon for doping level of 10^18/cm^3
Ecg = 0.1606;           % Conduction band edge in germanium for doping level of 10^18/cm^3
%%%%%%% Input Parameters to Calculate Strain %%%%%%%
a0Si = 5.4307;      % Silicon Lattice constant parallel to substrate
a0Ge = 5.6579;      % Germanium Lattice constant parallel to substrate
D001Si = 0.7713;    % Silicon deformation potential
D001Ge = 0.7509;    % Germanium deformation potential
```

```
EdUSi = 9.16;

EdUGe = 9.42;

%%%%%%%% Calculation of substrate lattice constant %%%%%%%%%

% Concentration of silicon in Si(x)Ge(1-x) substrate

x = 1;     % Si 001 substrate

% x = 0.5;   % Si(0.5)Ge(0.5) substrate

a11 = x*(a0Si) + (1-x)*(a0Ge);   % Lattice constant parallel to the superlattice layers

%%%%%%%%% Silicon Strain Parameters %%%%%%%%%%

a_1Si = a0Si*(1-D001Si*((a11/a0Si)-1));   % Lattice constant perpendicular to the layers

eps_parSi = (a11 - a0Si)/a0Si;                  % Strain parallel to the silicon layers

eps_perSi = (a_1Si - a0Si)/a0Si;                % Strain perpendicular to the layers

dEcs = (2/3)*(EdUSi)*(eps_perSi - eps_parSi);  % Shift in the conduction band edge due to strain

%% Germanium strain parameters %%

a_1Ge = a0Ge*(1-D001Ge*((a11/a0Ge)-1));   % Lattice constant perpendicular to the layers

eps_parGe = (a11 - a0Ge)/a0Ge;                  % Strain parallel to the silicon layers

eps_perGe = (a_1Ge - a0Ge)/a0Ge;                % Strain perpendicular to the layers

dEcg = (2/3)*(EdUGe)*(eps_perGe - eps_parGe);   % Shift in the conduction band edge due to strain

%%%%%%% New conduction band edges due to shift in band edges with strain %%%%%%%%

Ecs = Ecs + dEcs;            % New conduction band edge in silicon

Ecg = Ecg + dEcg;            % New conduction band edge in germanium

Ecb = 0.5*(Ecs + Ecg);      % Conduction band at interface of Si and Ge

%%%%%%%% Specifying temperature of source and drain %%%%%%%%

kT = 0.0259;               % General room temperature in eV (Boltzmann constant k * Temperature T)

kT1 = 0.0259;              % Source temperature at 300K

kT2 = 0.0259;              % Drain temperature at 300K

%%%%%%%%% Grid Inputs  %%%%%%%%%%

a = 2e-10;                    % Distance between successive nodes

Ns = 11;                      % Number of nodes in Silicon
```

```
Ng = 11;                    % Number of nodes in germanium
Ni = 2;                     % Number of Si-Ge interfaces
NC = Ns+Ng+Ns;              % Total number of nodes for Si/Ge/Si
Np = (NC-Ni);               % Actual number of nodes describing the superlattice
XS = a*(Ns-1);              % Length of silicon layer
XG = a*(Ng-1);              % Length of germanium layer
XX=a*(Np-1);                % Total length of superlattice
Len = linspace(0,XX,Np)';  % Stores length in a column vector
%%%%%%%%%%%%%%%%%%%%%%%%%%%%%%%%%%%%%%%%%%%%%%%%%%%%%%%%%%%%%%%%%%%%%%%%%%%%%%%
ts = (hbar^2)/(2*ms*(a^2)*q);       % Inter-unit cell coupling energy for silicon
tg = (hbar^2)/(2*mg*(a^2)*q);       % Inter-unit cell coupling energy for germanium
%%%%%%%%% Calculating the Superlattice Permittivity %%%%%%%%%%%
epsilr = zeros(Np,1);       % Specifying size of permittivity matrix
n = 1;
for n = n:(n+Ns-2)
   epsilr(n,1) = epsilrS;    % Inputs silicon permittivity
end
n = n+1;
epsilr(n,1) = epsilrJ;       % Inputs interface permittivity
n = n+1;
for n = n:(n+Ng-3)
   epsilr(n,1) = epsilrG;    % Inputs germanium permittivity
end
n = n+1;
epsilr(n,1) = epsilrJ;       % Inputs interface permittivity
n = n+1;
for n = n:(n+Ns-2)
   epsilr(n,1) = epsilrS;    % Inputs silicon permittivity
```

```
end
%%%%%%% Calculating Channel Potential Constants %%%%%%%%
Uo = q./(2*pi*epsilr*epsil0*a);   % Units of eV
Uo = Uo.*log(2);
U = 0;                                  % Setting initial potential in channel to be zero
%%%%%%%%%% Hamiltonian Matrix, Units of eV %%%%%%%%%
H = zeros(Np,Np);
n = 1;
for r = 1:1
     for n = n:(n + Ns-2)
      H(n,n) = Ecs + (2*ts);
     end
   n = n+1;
   H(n,n) = Ecb + ts+tg;
   n = n+1;
   for n = n:(n + Ng-3)
     H(n,n) = Ecg + (2*tg);
   end
   n = n+1;
   H(n,n) = Ecb + ts+tg;
   n = n+1;
   for n = n:(n + Ns-2)
      H(n,n) = Ecs + (2*ts);
   end
end
%%%%%%%%%% Specifying off-diagonal terms %%%%%%%%%
n = 1;
for r = 1:1
```

```
    for n = n:(n + Ns-2)
        H(n,n+1) = -ts;
        H(n+1,n) = -ts;
    end
    n = n+1;
    for n = n:(n + Ng-2)
        H(n,n+1) = -tg;
        H(n+1,n) = -tg;
    end
    n = n+1;
    for n = n:(n + Ns-2)
        H(n,n+1) = -ts;
        H(n+1,n) = -ts;
    end
end
[VH DH] = eig(H);      % Calculates eigen vectors and energy eigen values of Hamiltonian
DH = diag(DH);         % Stores subband energies (eigen values) of superlattice in a column vector
%%%%%%%% Defining energy range of incoming electrons %%%%%%%%%%
NE = 1201;             % Number of energy steps
E=linspace(0,1,NE);    % Specifying incoming electron range
dE=E(2)-E(1)           % Difference between each energy step
zplus=i*1e-12;         % Incremental term for energy for broadening during coupling
Eng = E';              % Stores energy steps in a column vector
No1 = (ms*kT1*q)/(2*pi*(hbar^2));    % Constant used in Fermi function (source) (1/m^2)
No2 = (ms*kT2*q)/(2*pi*(hbar^2));    % Constant used in Fermi function (drain) (1/m^2)
%% Specifying applied drain bias %%
NV = 201;              % Number of voltage steps
VV = linspace(0,0.1,NV);      % Setting voltage range from 0V to 0.1V
```

```
Vol = VV';                          % Stores voltage steps in a column vector
%%%%%%%%% START OF MAIN CURRENT-VOLTAGE CALCULATIONS %%%%%%%%%%
for nsb = 1:11              % Number of bands considered = Conduction band + 10 subbands
  if nsb == 1
    Ds = Ecs;               % For first iteration, energy corresponds to conduction band edge
  else
    Ds = DH(nsb-1);    % Additional iterations over subbands whose value is obtained from line 143
  end
  No = 0;    % For each subband, setting initial electron density in channel to be zero
  Sig1 = zeros(Np,Np); Sig2 = zeros(Np,Np);  % Initial values for self energy matrices
  for b = 1:NV  % Start of voltage loop
    V = VV(b);     % Voltage input for each step
    chg = 1;          % Initial guess for potential change
    while chg > 1e-6  % Checks potential change
        Rh = 0;             % Initial electron density along length of channel
        for k = 1:NE     % Starting energy loop for incoming electron energy
        %% Calculating Fermi functions of electrons entering through Silicon Source and Drain %%
        f1 = No1*log(1+exp((-(E(k)-mu))/kT1));        % 2D Source fermi function. Units of 1/m^2
        f2 = No2*log(1+exp((-(E(k)-mu + V))/kT2));  % 2D drain fermi function. Units of 1/m^2

        ka1 = acos(1 - ((E(k) + zplus - Ds)/(2*ts)));       % Wave vector of broadened waves at source
        Sig1(1,1) = -ts*exp(i*ka1);                         % Self energy of source  (eV)
        Gam1 = i*(Sig1 - Sig1');                            % Source broadening matrix (eV)
        SigIn1 = Gam1*f1;                                   % Inscattering term for source (eV)

        ka2 = acos(1 - ((E(k) + zplus - Ds + V)/(2*ts)));  % Wave vector of broadened waves at drain
        Sig2(Np,Np) = -ts*exp(i*ka2);                       % Self energy of drain (eV)
        Gam2 = i*(Sig2 - Sig2');                            % Drain broadening matrix (eV)
```

```
        SigIn2 = Gam2*f2;                              % Inscattering term for drain (eV)

        G = inv(((E(k) + zplus)*eye(Np)) -H -diag(U) -Sig1 -Sig2);   % Green's function  (1/eV)
        A = i*(G - G');                        % Channel density of states matrix (1/eV)
        Gn = G*(SigIn1+SigIn2)*G';       % Electron density matrix in channel (1/eV-m^2)

        Rh = Rh + (dE/(2*pi))*Gn;          % Calculating electron density in the channel  (1/m^2)
        T = Gam1*G*Gam2*G';              % Transmission function (no units, number)
        IT(k) = real(trace(T*(f1-f2)));      % Transmission current for each energy step (number/m^2)
        I1(k) = real(trace(SigIn1*A) - trace(Gam1*Gn)); % Source current for each energy step 1/m^2
        I2(k) = -real(trace(SigIn2*A) - trace(Gam2*Gn)); % Current for each energy step at drain 1/m^2
    end     % End of energy loop
    %%%%% Self consistent potential calculation %%%%%%
    N = real(diag(Rh));  % Stores diagonal elements (along length of channel) of density matrix (1/m^2)
    Unew = Uo.*(N-No)*(a^2);   % Channel potential (eV)
    dU = Unew-U;                    % Change in channel potential due to new electron density
    chg = max(abs(dU))
    U = U + 0.2*dU;                 % Updating channel potential with respect to old potential
    if V == 0
       No = N; chg = 0;
    end
    Rho = N/a;   % Normalized electron density per unit cell (1/m^3)
end   % End of potential while loop each voltage step
Den(:,b) = Rho;  % Stores electron density in channel for each voltage for the present subband
Pot(:,b) = U;       % Stores potential in channel for each voltage for the present subband
IE1(:,b) = I1';     % Current density per unit energy at source for each voltage
IE2(:,b) = I2';     % Current density per unit energy at drain for each voltage
Is(b) = dE*Io*sum(I1);   % Net source current density summed over all energies for each voltage step
```

```
    Isc = Is';
    Id(b) = dE*Io*sum(I2);   % Net drain current density summed over all energies for each voltage step
    Idr = Id';
    I(b) = dE*Io*sum(IT);    % Net transmission current summed over all energies for each voltage step
      Itr = I'
  end     % End of each voltage step loop
  Isb(:,nsb) = Itr;      % Transmission current for each subband
  Isbs(:,nsb) = Isc;    % Source current for each subband
  Isbd(:,nsb) = Idr;    % Drain current for each subband
end  % End of subband loop
II = sum(Isb,2)   % Sum of current from all subbands for each voltage step
hold on
dlmwrite('Len.dat',Len,',');     % Stores length of the channel
dlmwrite('Vol.dat',Vol,',');      % Stores applied voltage range with incremental steps
dlmwrite('Eng.dat',Eng,',');     % Stores electron energy range with incremental steps
dlmwrite('Isb.dat',Isb,'\t');       % Stores transmission current for each subband for each voltage step
dlmwrite('Isbs.dat',Isbs,'\t');    % Stores source current for each subband for each voltage step
dlmwrite('Isbd.dat',Isbd,'\t');   % Stores drain current for each subband for each voltage step
dlmwrite('II.dat',II,',');            % Stores sum of currents from all subbands for each voltage step
```

REFERENCES

[1] Ioffe, A. F. (1957) Semiconductor Thermoelements and Thermoelectric Cooling, London: Infosearch.

[2] Dresselhaus, M. S., Lin, Y. M., Koga, T., Cronin, S. B. Rabin, O., Black, M. R. and Dresselhaus, G. (2001) Quantum wells and quantum wires for potential thermoelectric applications, in Recent Trends in Thermoelectric Materials Research III, Ed. Tritt, T. M., Semiconductors and Semimetals, **71**, Academic Press, New York.

[3] Balandin, A. and Wang, K. L. (1998) Significant decrease of the lattice thermal conductivity due to phonon confinement in a free-standing semiconductor quantum well, Physical Review B, **58**, **3**, 1544-1549.

[4] Balandin, A. and K. L. Wang, (1998), Effect of phonon confinement on the thermoelectric figure of merit of quantum wells, Journal of Applied Physics, 84, 11, 6149-6153.

[5] Hicks, L. D., Harman, T. C. and Dresselhaus, M. S. (1993) Use of quantum-well superlattices to obtain a high figure of merit from non-conventional thermoelectric materials, Applied Physics Letters, **63**, **23**, 3230-3232.

[6] Whitlow, L. W and Hirano, T. (1995) Superlattice applications to thermoelectricity, Journal of Applied Physics, **78**, **9**, 5460-5466.

[7] Dresselhaus, M. S. (2003) Nanostructures and energy conversion, Proceedings of Rosenhow Symposium on Future Trends of Heat Transfer, Cambridge, MA.

[8] Bottner, H., Chen, G. and Venkatasubramanian, R. (2006) Aspects of thin-film superlattice thermoelectric materials, devices and applications, Materials Research Society Bulletin, **31**, 211-217.

[9] Koga, T., Cronin, S. B., Dresselhaus, M. S., Liu, J. L. and Wang, K. L. (2000) Experimental proof-of-principle Investigation of enhanced $Z_{3D}T$ in 001 oriented Si/Ge superlattices, Applied Physics Letters, **77**, **10**, 1-3.

[10] Vashaee, D. and Shakouri, A. (2004) Electronic and thermoelectric transport in semiconductor and metallic superlattices, Journal of Applied Physics, **95**, **3**, 1233-1245.

[11] Asenov, A, Watling, J. R., Brown, A. R. and Ferry, D. K. (2002) The Use of Quantum Potentials for Confinement and Tunneling in Semiconductor Devices, Journal of Computational Electronics, **1**, 503–513.

[12] Tang, T. W. and Wu, B. (2004) Quantum Correction for the Monte Carlo Simulation via the Effective Conduction-band Edge Equation, Semiconductor Science and Technology, **19**, 54-60.

[13] Lent, C. S. and Kirkner, D. J. (1990) The Quantum Transmitting Boundary Method, Journal of Applied Physics, **67**, **10**, 6353-6359.

[14] Laux, S. E., Kumar A. and Fischetti, M. V. (2002) Ballistic FET Modeling Using QDAME: Quantum Device Analysis by Modal Evaluation, IEEE Transactions on Nanotechnology, **1**, **4**, 255-259.

[15] Lundstrom, M., (2000) Fundamentals of Carrier Transport, Cambridge University Press.

[16] Datta, S. (2005) Quantum Transport: Atom to Transistor, New York: Cambridge University Press.

[17] Eisberg, R. and Resnick, R. (1974) Quantum Physics of Atoms, Molecules, Solids, Nuclei and Particles, John Wiley & Sons.

[18] Seebeck, T. J. (1822) The magnetic polarization of metals and ores produced by temperature difference, Proceedings. of Prussian Academy of Sciences, 265-373.

[19] Peltier, J. C. (1834) Nouvelles experiences sur la caloriecete des courans electriques, Annals of Chemistry, LVI, 371-387.

[20] Thomson, W. (1851) On a mechanical theory of thermoelectric currents, Proceedings of Royal Society of Edinburgh, 91-98.

[21] Joffe, A. F. (1952) Dokl. Akad. Naitk., USSR, **87**, 369.

[22] Goldsmid, H. J. (1954) On the thermal and electrical conductivity of semiconductors, Proceedings of the Physical Society of London, **67**, **4**, 360 - 363.

[23] Bardeen, J. and Shockley, W. (1950) Deformation potentials and mobilities in non-polar crystals, Physical Review, **8**0, **1**, 72-80.

[24] Goldsmid H. J. and Douglas, R. W. (1954) The use of semiconductors in thermoelectric refrigeration, British Journal of Applied Physics, **5**, **11**, 386-390.

[25] Ioffe, A. F., Airapetyants, S. V., Ioffe, A. V., Kolomoets, N. V. and Stil'bans, L. S. (1956) On increasing the efficiency of semiconductor thermocouples, Dokl. Akad. Nauk., USSR, **106**, 981.

[26] Birkholz, U. (1958) Z. Naturforsch. **13a**, 780.

[27] Rosi, F. D., Abeles, B. and Jensen, R. V. (1959) Journal of Physics C **10** 191.

[28] Yim, W. M. and Rossi, F. D. (1972) Compound tellurides and their alloys for Peltier cooling - A review, Solid State Electronics, **15**, 1121-1140.

[29] Goldsmid, H. J. (2001) Introduction, in Recent Trends in Thermoelectric Materials Research I, Ed. Tritt, T. M. Semiconductors and Semimetals, **69**, Academic Press, New York.

[30] Skrabek, E. A. and Trimmer, D. S. (1994) Properties of the general TAGS systems in CRC Handbook of Thermoelectrics, Ed. Rowe, D. M., Boca Raton: CRC Press.
[31] Abeles B., Beers, D. S., Cody G. D. and Dismukes, J. P. (1962) Thermal conductivity of Ge-Si alloys at high temperatures, Physical Review, **125**, **1**, 44-46.

[32] Rowe, D. M. and Bhandari, C. M. (1983) Modern Thermoelectrics, London: Holt, Rhinehart and Winston.

[33] Slack, G. A. (1979) The thermal conductivity of nonmetallic crystals, in Solid State Physics, Eds. Ehrenreich, H., Seitz F. and Turnbull, D. Academic Press, New York.

[34] Cahill, D. G., Fischer, H. E., Watson, S. K., Pohl, R. O. and Slack, G. A. (1989) Thermal properties of boron and borides, Physical Review B, **40**, **5**, 3254- 3260.

[35] Yamanaka, S., Kurosaki, K., Kosuga, A., Goto, K. and Muta, H. (2005) Extremely Low Thermal Conductivity Substances as Novel Thermoelectric Materials, Proceedings of the Fall Meeting of the Materials Research Society.

[36] Nolas, G. S., Cohn, J. L., and Slack, G. A. (1998) Effect of partial void filling on the lattice thermal conductivity of skutterudites, Physical Review B, **58**, **164**.

[37] Hoang, K., Mahanti, S. D., Androulakis, J. and Kanatzidis, M. G. (2005) Electronic Structure of AgPbmSbTem+2 Compounds - Implications on Thermoelectric Properties, Proceedings of the Fall Meeting of the Materials Research Society.
[38] Service, R. F. (2006) Semiconductor advance may help reclaim energy from 'lost' heat, Science, 1860.

[39] Sommerfeld, A. (1928) Zeits. F. Physik, **47**, 1.

[40] Sommerfeld, A. and Frank, N. H. (1931) The statistical theory of thermoelectric, galvano and thermomagnetic phenomena in metals, Review of Modern Physics, **3**, **1**, 1-8.

[41] Bloch, F. (1928) Zeits. F. Physik, **52**, 555.

[42] Wilson, A. H. (1931) The Theory of Electronic Semi-Conductors, Proceedings of Royal Society of London A, **133**, 822, 458-491.

[43] Bronstein, M. (1932) Phys. Z. Sowjetunion, **2**, 28.

[44] Fowler, R. H. (1933) An elementary theory of electronic semiconductors and some of their possible properties, Proceedings of Royal Society of London A, **140**, **842**, 505-522.

[45] Wilson, A. H. (1953) Theory of Metals, Cambridge University Press.

[46] Johnson, V. A. and Lark-Horovitz, K. (1953) Theory of thermoelectric power in semiconductors with applications to germanium, Physical Review, **92**, **2**, 226-232.

[47] Lark-Horovitz, K., Middleton, A. E., Miller, Scanlon, W. W. and Walerstein, Physical Review, 69, 259, 1946.

[48] Lord Kelvin (Sir. W. Thomson) (1882) Collected Papers I, Cambridge University Press.

[49] Onsager, L., (1931) Physical Review, **37**, 405.

[50] Callen, H. B. (1948) The Application of Onsager's reciprocal relations to Thermoelectric, Thermomagnetic and Galvanomagentic Effects, Physical Review, **73**, **11**, 1349-1358.

[51] Frederikse, H. P. R. (1953) Thermoelectric Power of Germanium below Room Temperature, Physical Review, **92**, **2**, 248-252.

[52] Price, P. J. (1956) Theory of Transport effects in Semiconductors: Thermoelectricity, Physical Review, **104**, **5**, 1223-1239.

[53] Tauc, J. (1954) Theory of Thermoelectric Power in Semiconductors, Physical Review, **95**, **6**, 1394.

[54] Altenkirch, E. (1909) Physikalische Zeitschrift, **10**, 560-580.

[55] Altenkirch, E. (1911) Physikalische Zeitschrift, **12**, 920-924.

[56] Ioffe, A. F. (1957) Semiconductor Thermoelements and Thermoelectric Cooling, London: Infosearch.

[57] Chasmar, R. P. and Stratton, R. (1959) The thermoelectric figure of merit and its relation to thermoelectric generators, Journal of Electronics and Control, **7**, 52-72.

[58] Littman, H. and Davidson, B. (1961) Theoretical bound on the thermoelectric figure of merit from irreversible thermodynamics, Journal of Applied Physics, **32**, **2**, 217-219.

[59] Rittner, E. S. and Neumark, G. F. (1963) Theoretical bound on the thermoelectric figure of merit of two-band semiconductors, Journal of Applied Physics, **34**, **7**, 2071-2077.

[60] Simon, R. (1962) Thermoelectric figure of merit of two-band semiconductors, Journal of Applied Physics **33**, **5**, 1830-1841.

[61] Callen, H. B. (1949) Electric breakdown in ionic crystals, Physical Review, **76**, 1394.

[62] Frohlich, H. (1954) Electrons in lattice fields, Advances in Physics, **3**, 325.

[63] Kohler, (1948) Z. Physik, **125**, 679.

[64] Rode, D. L. (1970) Electron mobility in direct-gap polar semiconductors, Physical Review B, **2**, **4**, 1012-1024.

[65] Nag, B. R. (1980) Electron Transport in Compound Semiconductors, Springer–Verlag, Berlin.

[66] Kane, E. O. (1957) Journal of Physical Chemistry of Solids, **1**, 249.

[67] Rode, D. L. (1971) Electron transport in InSb, InAs and InP, Physical Review B, **3**, **10**, 3287-3299.

[68] Sofo, J. O. and Mahan, G. D. (1994) Optimum band gap of a thermoelectric material, Physical Review B, **49**, **7**, 4565-4570.

[69] Esaki, L. and Tsu, R. (1970) Superlattice and negative differential conductivity in semiconductors, IBM Journal of Research and Development, 61-65.

[70] Slater, J. C. (1952) A soluble problem in energy bands, Physical Review, **87**, **5**, 807-835.

[71] Friedman, L. (1984) Thermopower of superlattices as a probe of the density of states distribution, Journal of Physics C, Solid State Physics, **17**, 3999- 4008.

[72] Sibille, A., Palmier, J. F., Wang, H. and Mollot, F. (1990) Observation of Esaki-Tsu negative differential velocity in GaAs/AlAs superlattices, Physical Review Letters, **64**, **1**, 52-55.

[73] Grahn, H. T., von Klitzing K. and Ploog, K. (1991) Electrical transport in narrow-miniband semiconductor superlattices, Physical Review B, **43**, **14**, 12094-12097.

[74] Lyo, S. K. (1988) Low-temperature phonon-drag thermoelectric power in heterojunctions, Physical Review B, **38**, **9**, 6345-6347.

[75] Kubakaddi, S. S., Milimani, B. G. and Butcher, P. N. (1992) Parallel and perpendicular phonon-drag thermopower in semiconductor superlattices, Semiconductor Science and Technology, **7**, 1344-1349.

[76] Mensah, S. Y. and Kangah, G. K. (1992) The thermoelectric effect in a semiconductor superlattice in a non-quantized electric field, Journal of Physics, Condensed Matter, **4**, 919-922.

[77] Hicks, L. D. and Dresselhaus, M. S. (1993) Effect of quantum-well structures on the thermoelectric figure of merit, Physical Review B, **47**, **19**, 12727-12731.

[78] Sofo, J. O. and Mahan, G. D. (1994) Thermoelectric figure of merit of superlattices, Applied Physics Letters, **65**, **21**, 2690-2692.

[79] Broido, D. A. and Reinecke, T. L. (1995) Effect of superlattice structure on the thermoelectric figure of merit, Physical Review B, **51**, **19**, 13797-13800.

[80] Broido, D. A. and Reinecke, T. L. (2001) Theory of thermoelectric power factor in quantum well and quantum wire superlattices, Physical Review B, **64**, 045324.

[81] Nag, B. R. (1980) Electron Transport in Compound Semiconductors, Springer-Verlag, Berlin.

[82] Scheidemantel, T. J., Ambrosch-Draxl, C., Thonhauser, T., Badding, J. V. and Sofo, J. O. (2003) Transport coefficients from first-principles calculations, Physical Review B, **68**, 125210.

[83] Lee, S. and von Allmen, P. (2006) Tight-binding modeling of thermoelectric properties of bismuth telluride, Applied Physics Letters **88**, 022107.

[84] Datta, S. (2000) Nanoscale Device Simulation: The Green's function formalism, Superlattices and Microstructures, **28**, 253-278.

[85] Szafer, A. and Stone, A. D. (1989) Theory of quantum conduction through a constriction, Physical Review Letters, **62**, 300-303.

[86] Muller, R., Kamins, T. and Chan, M. (1986) Device Electronics for Integrated Circuits, Wiley, New York.
[87] Patankar, S. V. (1980) Numerical Heat Transfer, Taylor and Francis.

[88] Geballe, T. H. and Hull, G. W. (1955) Seebeck effect in silicon, Physical Review, **98**, **4**, 940-947.

[89] Yang, B., Liu, J. L., Wang, K. L. and Chen, G. (2002) Simultaneous measurements of Seebeck coefficient and thermal conductivity across superlattice, Applied Physics Letters, **80**, **10**, 1758-1760.

[90] Sze, S. M. (1969) Physics of Semiconductor Devices, Wiley-Interscience.

[91] Choi, J. H., Park, Y. J. and Min, H. S. (1995) Electron mobility behavior in extremely thin SOI MOSFETs, IEEE Electron Device Letters, 16, **11**, 527-529.

[92] Takagi, S., Koga, J. and Toriumi, A. (1997) Subband structure engineering for performance enhancement of Si MOSFETs, IEEE Transactions of International Electron Devices Meeting, 219-222.

[93] Wang, T., Hsieh, T. H. and Chen, T. W. (1993) Quantum confinement effects on low-dimensional electron mobility, Journal of Applied Physics, **74**, **1**, 426-430.

[94] Fonoberov, V. A. and Balandin, A. A. (2006) Giant enhancement of the carrier mobility in silicon nanowires with diamond coating, Nano Letters, **6**, **11**, 2442-2446.

[95] Robert, K. (2002) Explaining strain: The positive and negative effects of elastic strain in n-silicon, IEEE Circuits and Devices Magazine, 36-39.

[96] Richardson, S. L., Cohen, M. L., Louie, S. G. and Chelikowsky, J. R. (1986) Electron charge densities at conduction-band edges of semiconductors, Physical Review B, Condensed Matter, **33**, **2**, 1177–1182.

[97] Van de Walle, C. G. (1989) Band lineups and deformation potentials in the model-solid theory, Physical Review B, **39**, 3, 1871-1883.

[98] Yang, B. , Liu, W. L., Liu, J. L., Wang, K. L. and Chen, G. (2002) Measurements of anisotropic thermoelectric properties in superlattices, Applied Physics Letters, **81**, **19**, 3588-3590.

[99] Yang, B., Liu, J., Wang, K. and Chen, G. (2002) Cross-plane thermoelectric properties in Si/Ge superlattices, Proceedings of the Materials Research Society, **691**, G. 3. 2. 1- G. 3. 2. 6.

[100] Yang, B., Liu, J. L., Wang, K. L. and Chen, G. (2002) Simultaneous measurements of Seebeck coefficient and thermal conductivity across superlattice, Applied Physics Letters, **80**, **10**, 1758-1760.

[101] Liu, W. L., Tasciuc, T. B., Liu, J. L., Taka, K., Wang, K. L., Dresselhaus, M. S. and G. Chen, (2001) In-Plane thermoelectric properties of Si/Ge superlattice, International Conference on Thermoelectrics, 340-343.

[102] Vashaee, D., Zhang, Y., Zeng, G., Chiu, Y. J. and Shakouri, A. (2004) Cross-plane Seebeck coefficient anomaly in a high barrier superlattice with Miniband formation, International Conference on Thermoelectrics, Adelaide, Australia.

[103] Venkatasubramanian, R., Colpitts, T., Watko, E. and Malta, D. (1997) Experimental evidence of improved thermoelectric properties at 300K in Si/Ge superlattice structures, Proceedings of Spring Meeting of the Materials Research Society, San Francisco, March 31-April 4.